Techniques for Spectroscopy with Frequency Combs

by

Bradley Smith

A dissertation submitted in partial fulfillment
of the requirements for the degree of
Doctor of Philosophy
(Applied Physics)
in The University of Michigan
2019

Doctoral Committee:

Professor Steven Cundiff, Chair
Professor Almantas Galvanauskas
Professor Ted Norris
Professor Duncan Steel
Professor Herbert Winful

Bradley Smith

bradcs@umich.edu

ORCiD: 0000-0002-7145-9498

For all the people who made me who I am today.

ACKNOWLEDGEMENTS

First and foremost I thank my wife, Amira, for bringing out the best of me in so many ways. Graduate school can be grueling at times, but you provided all the inspiration I could ever need. I thank my mom and dad for instilling in me a strong work ethic, encouraging good morals, and of course raising me – as a new parent I am only beginning to truly appreciate what these things mean. I also extend my gratitude to Steven Cundiff, Herb Winful, Duncan Steel, Ted Norris, and Almantas Galvanauskas for serving on my dissertation committee and mentoring me throughout my time at the University of Michigan. My trajectory through graduate school has been tumultuous but having great role models helped me preserver. I also thank Stephen Rand for serving as my first graduate advisor and providing my initial graduate research experience. Although I switched groups, I drew many lessons from the experience that had an undeniable, positive impact on my professional and personal development. During this time, John Whitaker, Alex Fisher, and Liz Dreyer taught me the fundamentals of working in an ultrafast laser lab and jump-started my career as an optical physicist. In addition, Liz inspired me to become the outreach chair for the Optics Society at the University of Michigan and to join the Michigan Light Project. The outreach events that I participated in as a result made me appreciate all of the opportunities and experiences I had as a child that shaped who I am today. On a related note, I thank my fellow Dow sustainability fellows (particularly Anna Harrison, Mike Lipowicz, and Christina Reynolds) for opening my eyes to the broad scope of opportunities that seek to increase Earth's sustainability – I realized my

passions for physics and sustainability can overlap no matter where I go professionally. Once I joined the Cundiff group, I received enormous social and professional support from all of the students and postdocs. I extend my gratitude to Bachana Lomsadze in particular for being a patient mentor and hard-working lab partner. I also thank the machine shop technicians (Jim especially) for teaching me how to machine. The parts I built were vital to my laboratory work. Lastly, I wish to thank the Applied Physics program (particularly Cyndi McNabb, Cagliyan Kurdak, Charles Sutton, and Lauren Segall) for accepting me into the program and providing such a nurturing environment.

I gratefully acknowledge support from two fellowships – a Graduate Research Fellowship (GRF) provided by the National Science Foundation (NSF) (1256260) and a Dow Doctoral Sustainability Fellowship provided by the Dow Chemical Company and the Graham Institute at the University of Michigan. In addition, I gratefully acknowledge research funding provided by the Intelligence Advanced Research Projects Activity (IARPA) program grant 2016-16041300005, which primarily covered the work in Chaps. III, V, and VI, the Defense Advanced Research Projects Agency (DARPA) Spectral Combs from UV to THz (SCOUT) program via the Army Research Office (ARO) grant W911NF-15-1-0625, which funded the work in Chap. IV, and the Air Force Office of Scientific Research (AFOSR) grant FA9550-12-1-0119 which sponsored other graduate work unrelated to this dissertation (cited in the Preface) but fundamental to my development as a student.

PREFACE

First of all, I recommend viewing this dissertation in its PDF format using an Adobe-brand PDF viewer. This will enable the animations in Chaps. III and V to be viewed properly.

My path through graduate school has been somewhat unconventional leading to a broader, but less deep, overall research experience. For this reason, several projects I have worked on are not included in this dissertation but are mentioned here to provide a more complete picture of my graduate experience. With Prof. Stephen Rand and Dr. John Whitaker I discovered, demonstrated, and theoretically analyzed a novel, all-optical means to steer few-cycle THz-frequency pulses [1–3]. Also during this time I began extending the Lorentz oscillator model independently – I intend to publish this work in Physical Review A soon. Because it provides a broad overview of light-matter interactions from a classical perspective, which may be helpful for a dissertation centered on spectroscopy, I have included this work in Appx. A.

TABLE OF CONTENTS

LIST OF FIGURES

Figure

LIST OF APPENDICES

Appendix

LIST OF ABBREVIATIONS

AOM acousto-optic modulator

CARS coherent anti-Stokes Raman scattering

CCD charge-coupled device

CW continuous wave

DAQ data acquisition board

DC direct current (meaning zero frequency)

DCS dual-comb spectroscopy

DDFG digital difference frequency generation

DDS direct digital synthesizer

DFG difference frequency generation

DTCS degenerate tri-comb spectroscopy

EOM electro-optic modulator

ESA electrical spectrum analyzer

EUV extreme ultraviolet

FFT fast Fourier transform

FIR far-infrared/finite impulse response

FPGA field-programmable gate array

FTIR Fourier transform infrared spectroscopy

FTS Fourier transform spectroscopy

FSR free spectral range

FWHM full width at half maximum

FWM four-wave mixing

HHG high-harmonic generation

HWHM half width at half maximum

HWP half-wave plate

IFE inverse Faraday effect

IIR infinite impulse response

LO local oscillator

LOM Lorentz oscillator model

MDCS multi-dimensional coherent spectroscopy

MIR mid-infrared

MOKE magneto-optic Kerr effect

NA numerical aperture

NEP noise equivalent power

NIR near-infrared

NLO nonlinear optics

NUFFT non-uniform fast Fourier transform

OR optical rectification

OSA optical spectrum analyzer

PBS polarizing beam splitter

PDE photon drag effect

PLL phase-locked loop

QCSE quantum confined Stark effect

QW quantum well

QWP quarter-wave plate

rf radio frequency

RIN relative intensity noise

SFG sum frequency generation

SHB spatial hole burning

SHG second harmonic generation

SMOKE surface magneto-optic Kerr effect

SNR signal-to-noise ratio

STP standard temperature and pressure

TCS tri-comb spectroscopy

TEC thermo-electric cooler

VCCS voltage controlled current source

ABSTRACT

This dissertation contains several novel works pertaining to the use of frequency combs for spectroscopy.

First, the optimum comb repetition rates (f_{Sig} and f_{LO}) for dual-comb spectroscopy were determined using a Monte Carlo approach to quantify their impact on the standard deviation of the error, σ, of the fitted parameters of a single Lorentzian resonance (assuming all else is equal, i.e. lasers powers, acquisition time, etc.). A maximum allowable spectral point spacing, $\delta\nu \approx \gamma$, where γ is the half width at half maximum of the resonance was identified. For the traditional implementation of dual-comb spectroscopy, the ideal repetition rates are $f_{\mathrm{Sig}} \approx f_{\mathrm{LO}} \approx \gamma$ but even more accurate measurements can be made by allowing for arbitrary near-harmonic repetition rate ratios. In this case the ideal repetition rates are $f_{\mathrm{Sig}} \lessapprox \gamma$ and $f_{\mathrm{LO}} \to \infty$. In general, $\sigma \propto 1/\sqrt{f_{\mathrm{LO}}}$ (i.e. no f_{Sig} dependence) for $f_{\mathrm{Sig}} \lessapprox \gamma$. The simulations were then generalized to quantify how the signal-to-noise ratio (SNR) and spectral point spacing, $\delta\nu$, affect the error, σ, in the fitted parameters of a Lorentzian function. The general result, $\sigma \propto \sqrt{\delta\nu}\,/\,\mathrm{SNR}$, was identified which applies beyond spectroscopy to any peak fitting situation.

Second, a novel type of frequency comb source based on a single-section semiconductor diode laser was characterized and its potential to enable battery-powered dual-comb spectroscopy was examined. For characterization, the tunability of the comb parameters (i.e. the repetition rate and offset frequency) was measured as a function of the diode temperature and injection current. Tuning the injection current (temperature) was found to change the repetition rate by -91 ± 9 MHz/A (-2 ± 3

MHz/°C) and the offset frequency by -4.2 ± 0.1 kHz/A (-4.4 ± 0.2 kHz/°C). Next, the ability to perform dual-comb spectroscopy using these combs powered by standard laboratory-grade equipment was demonstrated. Later, a battery-powered current driver was built that successfully powered a comb.

Third, a novel form of nonlinear hyperspectral imaging that leveraged frequency combs was developed and demonstrated. 400-pixel images that spectrally resolved a four-wave mixing signal from a GaAs-quantum-well-based sample with comb resolution were constructed using only 45 seconds worth of collected data. The images reveal spatially varying spectral features that can be attributed to a combination of an inhomogeneous, thermally-induced strain field and the quantum confined Stark effect it produces via a piezoelectric field. Advantages of this technique compared to prior arts were also evaluated.

Fourth, a novel technique coined tri-comb spectroscopy that replaces the mechanical delay lines used in many multi-dimensional coherent spectroscopy experiments with three frequency combs having different repetition rates was developed and demonstrated. A rephasing spectrum and multiple linear spectra, all with comb resolution, of a gaseous mixture of Rb isotopes were simultaneously constructed from only 365 ms of acquired data. Future improvements to this technique where the repetition rates of all combs are identical were posited and explored.

CHAPTER I

Introduction

Spectroscopy is the study of the interaction between light and matter and has three primary goals. First, information about a specific source of light can be obtained using a known material and a known light-matter interaction (e.g. characterizing the optical output of a laser diode as in Ref. [4]). Second, the properties of a material can be explored using a known light source and light-matter interaction (e.g. remotely sensing greenhouse gas concentrations as in Ref. [5]). Lastly, the interactions themselves can be studied using known materials and light sources (e.g. exploring the many-body physics affecting the photoluminescence of highly charged quantum dots as in Ref. [6]). Within each of these three branches there are many different techniques available and new ones waiting to be discovered – this dissertation presents several novel works that utilize a class of lasers called frequency combs for spectroscopy.

From a theoretical perspective, light-matter interactions manifest themselves in the form of constitutive relations for Maxwell's equations. These include expressions for the polarization density $\mathbf{P}$, magnetization density $\mathbf{M}$, and electric quadrupolarization $\mathbf{Q}$ (and higher-order terms if necessary) and this is where all of the "physics" that comprise light-matter interactions literally and figuratively enters the equation [7]. Every material has unique constitutive relations. In most matter (except for example those exhibiting bi-stability), each one of $\mathbf{P}$, $\mathbf{M}$, and $\mathbf{Q}$, can be expanded in joint

power series of $\mathbf{E}$ and $\mathbf{B}$ such as

$$\mathbf{P} = \mathbf{P}^{(0)} + \mathbf{P}^{(E)} + \mathbf{P}^{(B)} + \mathbf{P}^{(EE)} + \mathbf{P}^{(EB)} + \cdots , \tag{1.1}$$

where for example the term $\mathbf{P}^{(EB)}$ scales linearly with both $\mathbf{E}$ and $\mathbf{B}$ (if you double $\mathbf{E}$ or $\mathbf{B}$ then $\mathbf{P}^{(EB)}$ also doubles). In most optics textbooks (e.g. Refs. [8,9]) dependence on $\mathbf{B}$ within the constitutive relations is neglected despite many real phenomena showing explicit dependence on $\mathbf{B}$. For example, the Faraday isolators used Chaps. VI and V rely on a linear magneto-optic effect which is described by the term $\mathbf{P}^{(EB)}$. For a classical overview of light-matter interactions and their representation in constitutive relations see Appx. A. Fortunately, most physical phenomena can be described by retaining only a small number of these terms and ignoring the rest.

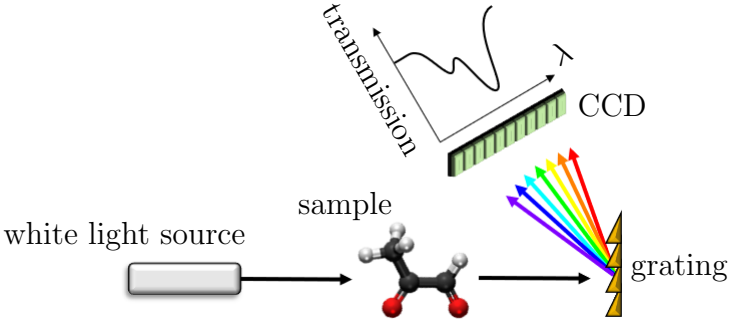

Figure 1.1: Cartoon of a simple transmission spectroscopy experiment. Collimated white light passes through a sample, diffracts off a grating, and is detected by a CCD revealing absorption information.

The simplest constitutive relation retains only $\mathbf{P} = \mathbf{P}^{(E)}$ and ignores all other terms and constitutive relations. This linear response approximation accurately describes a surprising number of real phenomena [10]. A simple example of linear spectroscopy is shown in Fig. 1.1. Another technique that is fundamental to this work is Fourier transform spectroscopy (FTS) – see Appx. B for a brief overview or Ref. [11]. The fundamental idea behind FTS is that when light impinges upon a medium, the medium responds by developing a polarization density having a tempo-

ral coherence determined by its optical properties. This polarization density usually radiates light that is phase-matched to the incident light and so superimposes with it in the forward direction. The temporal coherence in the polarization is then imprinted on the outgoing light. It can be useful to have the picture in mind that when a pulse of light enters a material it leaves with a "tail" (see Fig. 1.2). The goal of FTS is to measure this tail – which serves as a proxy for the polarization density – and extract the material's optical properties from it. Linear spectroscopy techniques are relatively simple but provide limited information.

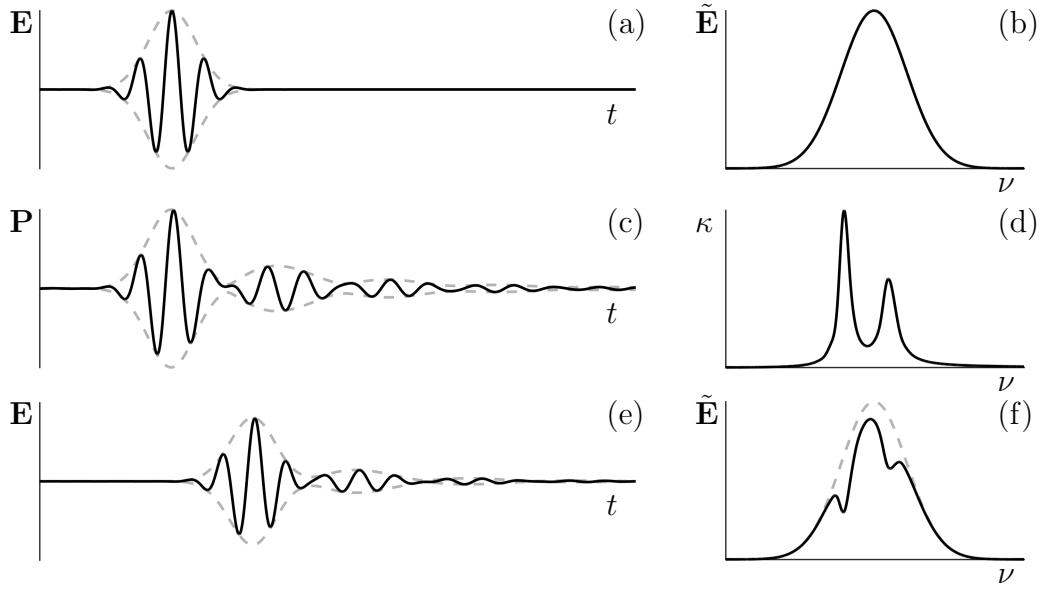

Figure 1.2: A pulse of light is transmitted through a slab of material illustrating the primary concept of FTS. (a,b) Incident electric field of a Gaussian pulse (dotted line is envelope). (c) Linear response of the material evaluated near the entrance face (dotted line is envelope). (d) Extinction coefficient of the material. (e) Transmitted electric field showing a "tail" resulting from material absorption (dotted line is envelope). (f) Fourier transform of (e) showing spectrum of transmitted field (dotted line is spectrum of incident field).

For a long time Fourier transform infrared spectroscopy (FTIR) was the unchallenged gold standard of high-resolution broadband spectroscopy. However, it's position is being challenged by a technique called dual-comb spectroscopy (DCS) that replaces the scanning delay stage in FTIR with two frequency combs having slightly different repetition rates [12]. See Chap. II for a brief overview of frequency combs

and Chap. III for more information on DCS. Compared to FTIR, typical implementations of DCS have resolutions that are several orders of magnitude smaller and can acquire single spectra on a microsecond timescale. Because DCS has no moving parts it is intrinsically more robust and field-deployable than FTIR. However, the available optical bandwidth from a frequency comb is smaller than the thermal sources used in FTIR. Using large optical bandwidths in DCS also places stringent requirements on the repetition and offset frequencies of the combs which adversely affects the acquisition time of a single spectrum and therefore the SNR for a fixed acquisition period. This can be circumvented by choosing combs with higher repetition rates (assuming all else is fixed), but there is a trade-off: the free spectral range increases meaning the material response function is more coarsely sampled leading to less accurate fitting of the data for determining the response function parameters. Chap. III explores this trade-off with the goal of identifying the optimum comb repetition rates for a given sample of interest.

As mentioned, DCS systems can be quite robust and even deployed on a vehicle [13]. However, there is still much more room for improvement - the dream is to perform high-quality DCS using a single, integrated, hand-held device. Chap. IV provides a demonstration of AA battery powered laser diode frequency combs – an important step to take in this regard. Unlike microring resonator combs (another compact comb technology used for DCS [14,15]) these laser diodes require no external pumping and could easily be mass produced using standard fabrication techniques.

While linear spectroscopy is undoubtedly very useful, it does have certain limitations. For example, it cannot distinguish between homogeneous and inhomogeneous broadening nor coupled and uncoupled energy levels, it breaks down at high field strengths, and it completely ignores population dynamics. These limitations can sometimes be addressed by retaining more terms (i.e. nonlinear terms) in the constitutive relations mentioned earlier. Appx. A outlines the physical phenomena

associated with these other terms.

The most relevant nonlinear term to this dissertation is $\mathbf{P}^{(EEE)}$ (which is usually just called $\mathbf{P}^{(3)}$). One method to access the information contained in its corresponding third-order response function is multi-dimensional coherent spectroscopy (MDCS). Appx. E introduces MDCS as a nonlinear extension of FTS and contains references to several textbooks that have more detailed information. MDCS has the ability to spectrally resolve $\boldsymbol{\chi}^{(3)}$ (the response function for $\mathbf{P}^{(3)}$) by measuring the temporal coherences embedded in $\mathbf{P}^{(3)}$ using a series of three pulses (see Fig. 1.3). This comes at the cost of increased experimental complexity. Another technique that is simpler but obtains less information on $\boldsymbol{\chi}^{(3)}$ is spectrally resolved four-wave mixing. Chap. V presents an application of this technique to hyperspectral microscopy.

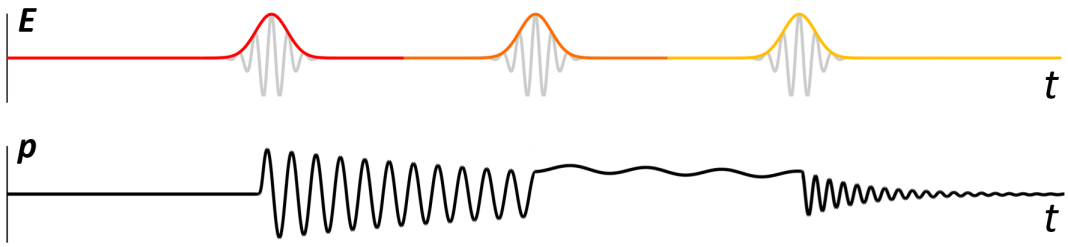

Figure 1.3: Cartoon describing the measurement of a third-order nonlinear response function. (top) Electric fields and envelopes of three pump pulses (red, orange, and yellow) impinging on a sample. (bottom) Expectation value of the third-order electric dipole response of a system to the three pump pulses corresponding to one possible perturbative quantum pathway. By scanning the pump pulse delays, MDCS measures the "tails" in $\mathbf{p}$ which contain information about its corresponding nonlinear response function. More information is available in Appx. E.

As noted earlier, the introduction of frequency combs to FTS produced a powerful new technique (DCS) that has garnered much recent attention. In a similar vein, Chap. VI presents the introduction of frequency combs to MDCS which has resulted in a new technique called tri-comb spectroscopy (TCS). The same advantages that DCS has over FTIR (increased acquisition speed, resolution, etc.) have been realized for TCS compared to delay-stage-based MDCS. However, the trade-off between maximum acceptable optical bandwidth and SNR/acquisition speed that exists for

DCS is different for TCS because the latter is a nonlinear technique. Increasing the repetition rates in a nonlinear experiment (and holding all other parameters fixed) actually *decreases* the SNR because it lowers the energy per pulse [16]. So for TCS the trade-off is between SNR/maximum optical bandwidth and acquisition speed. This points towards lower repetition rates being ideal for TCS but this becomes technologically challenging since it requires ever tighter locking of the comb parameters. Furthermore, the results of Chap. III suggest that achieving full comb resolution may be unnecessary depending on the spectral lines under consideration. Lastly, using lower repetition rates may also involve measuring points long after the temporal coherence tail has decayed. This has two problems: one, these points usually have the lowest SNR which can lower the overall measurement SNR and, two, they take time to measure that could be better spent on more important parts of the tail. This all seems to promote the use of frequency combs that have the *same*, low repetition rate and to scan the delay between pulses an amount less-than the pulse repetition period by some other means. But wait, doesn't stage-based MDCS satisfy these criteria? Yes. However, there are still benefits to using frequency combs instead of delay stages. For example, the lack of moving parts makes a comb-based technique more robust/deployable. Chap. VII explores the potential for such a technique which, for now, is referred to as degenerate tri-comb spectroscopy (DTCS) and also concludes this dissertation.

CHAPTER II

Background on combs

Frequency combs originate from waveforms that have intrinsic periodicity. Anything periodic can be described by a Fourier series which is discrete by definition. If instead a Fourier transform is used, this discreteness remains in the form of a "comb structure" (because it looks like a hair comb) in the frequency domain. Fig. 2.1 depicts a frequency comb in both the time and frequency domains. The paradigm shift that lead to the development of frequency combs was the extension of Ramsey interferometry – in which the interference of two pulses interacting with a sample is used to increase spectral resolution [17] – to a long train of pulses rather than just two [18]. Essentially, this corresponded to a shift in thinking from the time domain to the frequency domain. For broad overviews of frequency combs including their history see Refs. [19, 20]. This chapter provides background on frequency comb generators (sources), applications, and the definition of a comb both mathematically and physically.

2.1 Sources and applications

Frequency combs can be generated from a growing number of sources. The first ever realization of a frequency comb was a synchronously pumped mode-locked continuous wave (CW) dye laser [18] in 1978 but the ps pulse train had a small

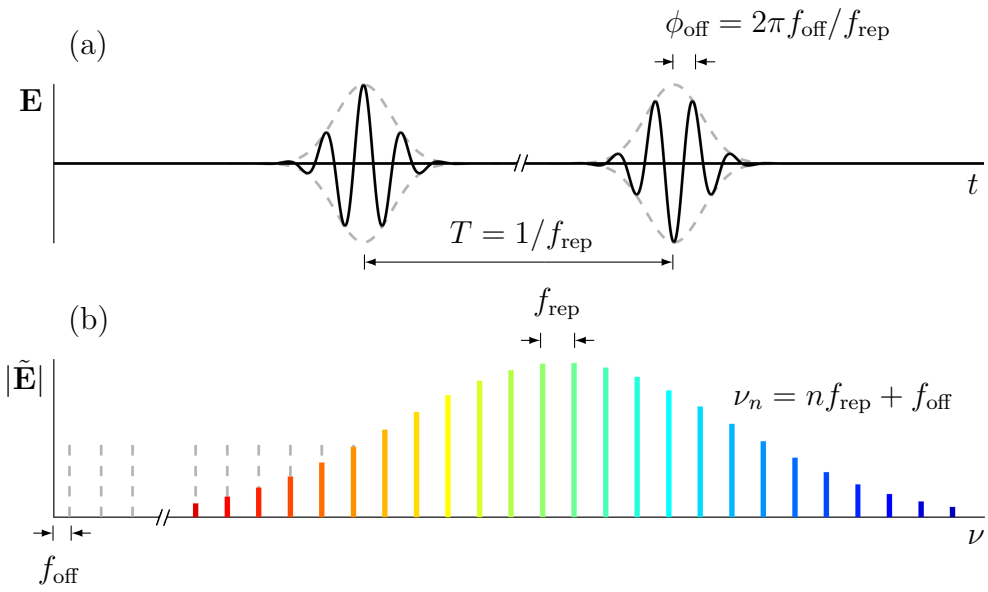

Figure 2.1: (a) In the time-domain, a frequency comb is defined by an infinitely long train of identical but arbitrarily-shaped envelopes with period $T = 1/f_{\rm rep}$. Each successive carrier wave slips by a phase of $\phi_{\rm off} = 2\pi f_{\rm off}/f_{\rm rep}$ with respect to its envelope. (b) The Fourier transform of (a) reveals comb structure with a FSR of $f_{\rm rep}$ offset from the origin by frequency $f_{\rm off}$. The optical frequency of each comb tooth is given by $\nu_n = nf_{\rm rep} + f_{\rm off}$ where n is an integer.

bandwidth limiting its usefulness. The development of the mode-locked Ti:sapphire oscillator enabled fs combs [19] and eventually the ability to self-reference a comb [21] – a now-common technique for measuring and subsequently controlling the offset frequency (see next section) which is critical for the generation of attosecond pulses [22] and extreme ultraviolet (EUV) combs via high-harmonic generation (HHG) [23]. This type of comb (the Ti:sapphire oscillator) was used for the experiments described in Chaps. V and VI. In fact, I had the honor of resurrecting the very comb used in Ref. [21] for this purpose (albeit with few of the original parts). These lasers use Kerr-lens mode-locking to generate a train of ultrafast pulses. Frequency combs can also be carved out of CW light via modulation. Typically this is accomplished with phase modulation using a high-speed electro-optic modulator (EOM) either inside or outside a cavity (e.g. electro-optic combs) [24,25]. This enables the advantageous, orthogonal control of the repetition rate, by tuning the modulator, and offset frequency, by tuning the CW laser center frequency (see next section). Alternatively, an acousto-

optic modulator (AOM) can be placed inside a laser cavity as in frequency-shifting loops (also known as Talbot lasers) [26]. Every time light makes a round-trip through the cavity it is frequency shifted by the same amount thus generating comb lines one at a time. This approach allows broadband comb output to be generated using relatively low bandwidth modulation. Other cascaded mixing schemes will also produce combs as is the case with microresonators (called microcombs) [14] and Brillouin frequency combs [27]. In the former, tight field confinement, a high quality factor, and a large nonlinear susceptibility lead to strong, cascading four-wave mixing (FWM) processes every round trip. Phase matching is achieved by balancing dispersion with the nonlinear refractive index leading to soliton formation. In the latter, tight field confinement allows efficient stimulation of Brillouin modes and subsequent FWM between them. Another technique is to use nonlinear frequency conversion of an existing comb. For example, the optical rectification of a near-infrared (NIR) comb produces a THz or far-infrared (FIR) comb with precisely zero offset frequency [28]. Similarly, difference frequency generation (DFG) can be used to generate mid-infrared (MIR) combs [29]. Upconversion is also possible – as mentioned earlier EUV combs can be created through HHG of a NIR comb [23]. Even laser diodes can produce combs by combining spatial hole burning and FWM (see Chap. IV) [30,31]. The characteristics of these combs are explored in Chap. IV. Quantum cascade lasers can also be phase-locked using similar physics to produce MIR combs [32]. Lastly, one might suspect that simply filtering thermal light with a Fabry-Perot will produce a comb as well. However, even though the output spectrum may look like a comb, it lacks temporal periodicity which is the true hallmark of a comb – this will be examined in detail in the next section.

Frequency combs have several important features that have revolutionized many different fields. First of all, the spectral span of the comb is much greater (up to a factor of 1,000,000 or more) than the sum of the linewidths of all the individual teeth.

When utilized correctly, this allows for the interrogation of a broad range of optical frequencies, albeit with a large spectral point spacing, using a radio frequency (rf) bandwidth commonly a million times smaller – DCS (see Chap. III especially Fig. 3.1), for example, does exactly this [12]. The compactness and high acquisition speed of DCS (sometimes called frequency comb multi-heterodyne spectroscopy) make it ideal for remote chemical sensing applications [33]. The dual-comb bandwidth compression approach can also be leveraged in the time-domain to allow for ultrafast ranging [34]. Furthermore, the low "duty-cycle" (discreteness) of the comb structure also allows for the precise, optical control of the amplitude and phase of each comb tooth resulting in the ability to optically synthesize an arbitrary, periodic waveform [35]. Another important feature of combs is that the optical frequencies of all the comb teeth are given by a linear combination of two radio frequencies (see following section). Absolute positioning of the comb teeth is enabled when those radio frequencies are referenced to an accurate time standard such as an atomic clock. Therefore, the comb can be used as an optical ruler, for example, to calibrate exoplanet hunting spectroscopic tools [36]. One can also think of a comb as a collection of evenly spaced CW lasers. Thus, CW spectroscopic techniques can be used. For instance, a single comb tooth can be scanned through a resonance by controlling f_{rep} and f_{off} in a known way and the resulting fluorescence detected. This is called direct frequency comb spectroscopy [37]. These techniques can also be applied in the reverse direction – rather than using known radio frequencies to generate controlled optical frequencies, one can use known optical frequencies (e.g. optical atomic or molecular transitions) to derive precise radio frequencies. This approach forms the basis of optical atomic clocks [38]. These highly precise time-keeping devices can be used for everything from relativistic geodesy [39], to constraining the time variation of the fundamental constants [40], to perhaps one day even gravitational wave astronomy [41], and much more (see Ref. [38] for overview). Control of the offset frequency (typically using

self-referencing [21]) enables the production of EUV combs with attosecond pulses via HHG which is highly sensitive to the carrier-envelope phase [22, 23]. Besides studying HHG and other attosecond process, these sources can be used for advanced spectroscopy techniques [42] and can potentially probe nuclear transitions. The latter would enable so-called "nuclear" clocks [43] which due to the high frequency of the transitions involved may outperform state-of-the-art optical atomic clocks. If made bright enough, EUV combs could also upgrade current lithography techniques [44].

2.2 Math

Mathematically, one can describe the analytic representation of the electric field of an infinitely long, periodic train of pulses as

$$\mathbf{E}(t) = \sum_{m=-\infty}^{\infty} \boldsymbol{\mathcal{E}}(t - mT)\; e^{i[\omega_{\mathrm{c}}(t-mT)+m\phi_{\mathrm{off}}]}\;, \tag{2.1}$$

where the sum runs to infinity, $\boldsymbol{\mathcal{E}}$ is the envelope, and ω_{c} is the carrier angular frequency. The meaning of the other variables can be inferred from Fig. 2.1. The comb structure can be revealed by Fourier transforming Eq. (2.1) into the frequency-domain using

$$\tilde{\mathbf{g}}(\omega) \equiv \int_{-\infty}^{\infty} \mathrm{d}t\; \mathbf{g}(t)\, e^{-i\omega t}\;. \tag{2.2}$$

Since Eq. (2.1) is the product of two functions, one can apply the convolution theorem: $\mathcal{F}[f \cdot g] = \mathcal{F}[f] * \mathcal{F}[g]$ where $\mathcal{F}$ denotes a Fourier transform and $*$ indicates convolution. Thus,

$$\tilde{\mathbf{E}} = \sum_{m} \mathcal{F}\left[\boldsymbol{\mathcal{E}}(t - mT)\right] * \mathcal{F}\left[e^{i[\omega_{\mathrm{c}}(t-mT)+m\phi_{\mathrm{off}}]}\right]\;. \tag{2.3}$$

Now we apply the Fourier shift theorem, $\mathcal{F}[g(t-\tau)] = \exp(-i\omega\tau)\mathcal{F}[g(t)]$, to the first Fourier transform and evaluate the Fourier transforms yielding

$$\begin{aligned}\tilde{\mathbf{E}}(\omega) &= \sum_m \left[e^{-im\omega T} \tilde{\boldsymbol{\mathcal{E}}}(\omega) \right] * \left[e^{-im(\omega_c T - \phi_{\text{off}})} \delta(\omega - \omega_c) \right] \\ &= \tilde{\boldsymbol{\mathcal{E}}}(\omega - \omega_c) \sum_m e^{im(\omega T - \phi_{\text{off}})} \ . \end{aligned} \tag{2.4}$$

The sum is purely over complex exponential functions and should remind the reader of a Fourier series. So what function has all of its Fourier coefficients equal to one? The Dirac comb! It's definition with spacing $\omega_{\text{rep}} = 2\pi f_{\text{rep}} = 2\pi/T$ is

$$\text{III}_{\omega_{\text{rep}}}(\omega) \equiv \sum_{k=-\infty}^{\infty} \delta(\omega - k\omega_{\text{rep}}) \tag{2.5}$$

$$= \frac{1}{\omega_{\text{rep}}} \sum_{m=-\infty}^{\infty} e^{im\omega T} \quad . \tag{2.6}$$

Accounting for the carrier slip one has

$$\omega_{\text{rep}} \, \text{III}_{\omega_{\text{rep}}}(\omega - \omega_{\text{off}}) = \sum_{m=-\infty}^{\infty} e^{im(\omega - \omega_{\text{off}})T} \ . \tag{2.7}$$

where $\omega_{\text{off}} \equiv \phi_{\text{off}}/T$. Thus, the Fourier transform of the electric field can be succinctly written as

$$\tilde{\mathbf{E}}(\omega) = \omega_{\text{rep}} \, \tilde{\boldsymbol{\mathcal{E}}}(\omega - \omega_c) \, \text{III}_{\omega_{\text{rep}}}(\omega - \omega_{\text{off}}) \ . \tag{2.8}$$

Alternatively this may be expressed with non-angular frequencies (refer to the appropriate Fourier transforms) as

$$\tilde{\mathbf{E}}(f) = f_{\text{rep}} \, \tilde{\boldsymbol{\mathcal{E}}}(f - f_c) \, \text{III}_{f_{\text{rep}}}(f - f_{\text{off}}) \ . \tag{2.9}$$

If we move Eq. (2.9) back into the time-domain and use Eq. (2.5) we find

$$\mathbf{E}(t) = f_{\text{rep}} \sum_{k=0}^{\infty} \tilde{\boldsymbol{\mathcal{E}}}(kf_{\text{rep}} + f_{\text{off}} - f_{\text{c}})\, e^{2\pi i(kf_{\text{rep}}+f_{\text{off}})t} \,. \tag{2.10}$$

Clearly, a frequency comb is equivalent to a *discrete* number of CW lasers with frequencies $kf_{\text{rep}} + f_{\text{off}}$. This is the result of the periodicity of the waveform and is not very obvious from Eq. (2.1). It should have been clear once the frequency-domain comb structure was revealed in Eq. (2.9). The periodicity of the comb *requires* that this collection of CW lasers are *phase coherent* to each other. This is guaranteed mathematically because the frequency of each CW laser is given by $kf_{\text{rep}} + f_{\text{off}}$. In other words, their frequencies (and thus phases) are all determined by the same two parameters. This is the reason why using a Fabry-Perot to filter thermal light will not produce a comb despite producing evenly spaced spectral lines – there is no phase relationship between the output "teeth" and thus no temporal periodicity. The temporal envelope and carrier phase will be effectively random each repetition period. Without the periodicity and the ability to relate the phases of the spectral lines, the filtered thermal light is useless for most of the applications mentioned in the previous section.

CHAPTER III

Optimum repetition rates for DCS

3.1 Overview

As mentioned in Chap. II, there are a multitude of frequency comb sources all having widely varying parameters such as technological maturity, average output power, repetition rate, optical bandwidth, etc. Because of this, when designing a practical implementation of DCS, selecting the ideal comb sources is not a straightforward task. This chapter provides a quantitative means to make this choice for a given application.

DCS has proven to be highly proficient at identifying and measuring the concentrations of molecules, which is desirable for a variety of applications such as greenhouse gas sensing, toxin detection, and biomedical tissue analysis [45]. To succeed in these endeavors, it is imperative to be able to accurately and precisely measure the properties (i.e. line center, width, and amplitude) of some spectral feature. Of course the speed and accuracy of this task benefit from a higher SNR; the understanding and improvement of which have been the focus of many previous works [46–50]. However, the SNR is not the only significant parameter – as shown in this chapter, the repetition rates of the two combs have a tremendous impact on the error and uncertainty of the ascertained line properties assuming all else is equal. This impact is greatest when allowing for the selection of arbitrary-harmonic related repetition rates.

In the conventional implementation of DCS (see Fig. 3.1(a)), one comb (referred to as the signal comb with a repetition rate of f_{Sig}) is transmitted through a medium of interest while the second comb (referred to as the local oscillator (LO) or "read-out" comb with a repetition rate of f_{LO}) bypasses the medium and interferes with the signal comb on a detector. The repetition rates of the two combs are slightly different so that their ratio ($\rho_{\mathrm{r}} \equiv f_{\mathrm{LO}} : f_{\mathrm{Sig}}$) is very close to unity. In the frequency-domain (see Fig. 3.1(b-c)), this means that the beat notes between any two signal and LO comb lines seen on the detector occur at unique, evenly spaced frequencies thereby forming a rf comb. This one-to-one mapping links the measured rf comb lines and the optical comb lines that generated them. Because the amplitude and phase of each individual signal comb line can be measured, the spectral line is sampled with a spectral point spacing, $\delta\nu$, equal to f_{Sig}. In the time-domain, the use of nearly identical repetition rates implies that the time delay between sequential pairs of signal and LO pulses increases by a small, very precise amount (approximately $\Delta f/f^2$) . This configuration is analogous to dispersive FTIR (see Appx. B) in the sense that the relative time-delay between two pulses is scanned so that they sample one another at discrete points and indeed the recorded interferograms appear very similar. However, by taking advantage of the high precision of combs and avoiding the use of a mechanical delay stage, DCS has significantly better spectral resolution, compactness, robustness, and acquisition times.

Although the repetition rates of the two combs used in the vast majority of conventional DCS setups possess a near-unity ratio, in principle any near-harmonic (i.e. near-multiple) relationship between the repetition rates is acceptable. The concept of heterodyning two periodic optical waveforms with arbitrary near-harmonic repetition rates has been used to characterize the envelope [51] and more recently the envelope and spectral phase [4, 52] of an unknown waveform. The latter two techniques are quite similar to DCS in the way that they retrieve optical information from the rf sig-

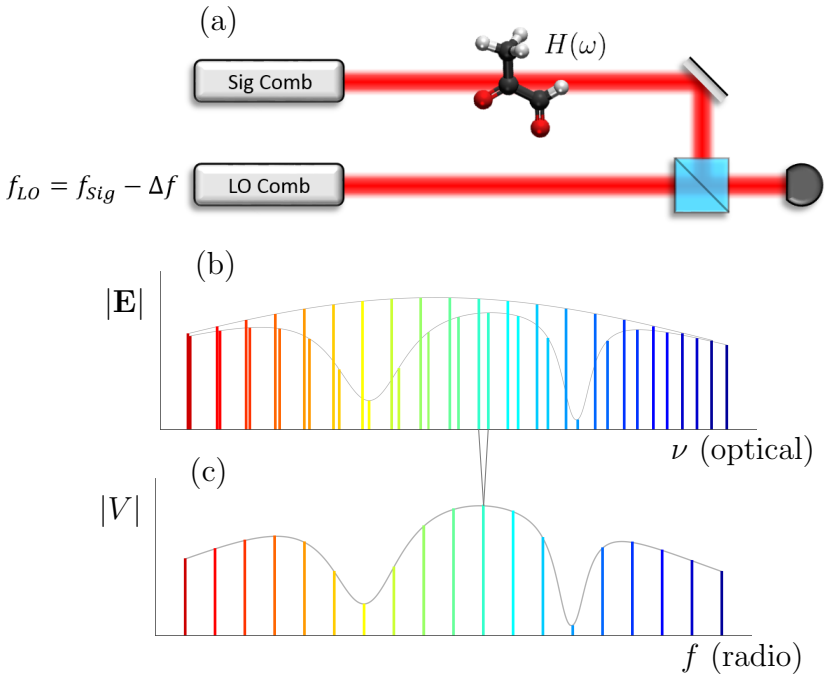

Figure 3.1: Conventional implementation of DCS. Compare to FTS in Appx. B especially Figs. B.1 and B.2. (a) Experimental schematic: a signal comb is transmitted through a sample with transfer function $H(\omega)$ and interfered with a local oscillator comb having a slightly different repetition rate on a photodetector. (b) Optical spectra of the two combs. The signal comb teeth are attenuated and phase shifted by propagating through the sample as prescribed by $H(\omega)$. (c) The rf comb seen on the detector in a bandwidth of $f_{\mathrm{LO}}/2$ illustrating the optical-to-rf mapping – every rf tooth corresponds to beating between one signal comb tooth and one LO comb tooth. Two gray lines provide an example of the mapping.

nal by leveraging the one-to-one mapping between a pair of signal and LO comb lines and their beat note on a detector. The use of near-harmonic repetition rate combs has also been applied to DCS – but rather than directly using the rf-to-optical mapping, the authors viewed the measured rf signal as a temporal-multiplexing of independent traditional DCS interferograms then demultiplexed and combined them [53]. Another method that utilizes two pulse trains actually allows for *any* ρ_{r} although its sub-picosecond time accuracy is insufficient for DCS [54].

An example of how the optical information is mixed into the rf domain on a detector for ρ_{r} near $2:1$ is shown in Fig. 3.2. From Fig. 3.2 it is clear that the

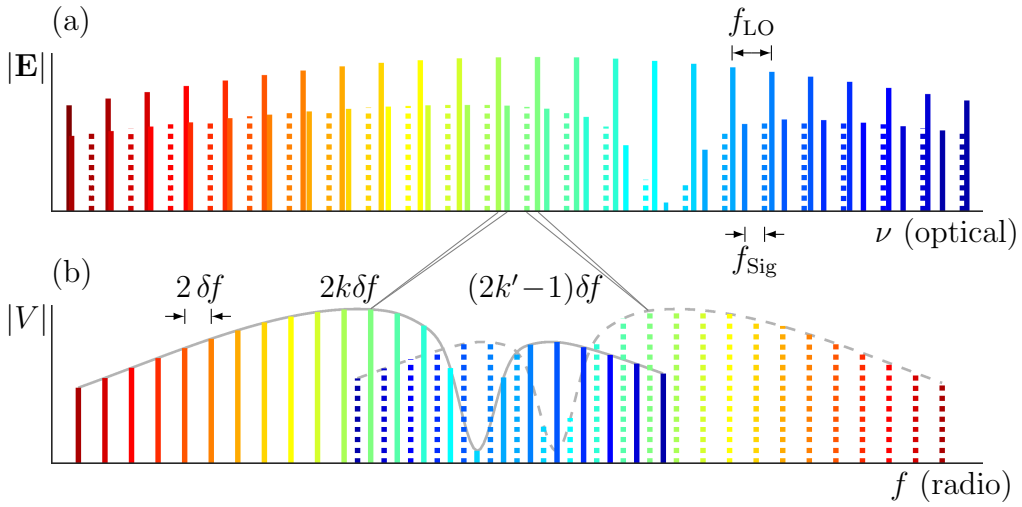

Figure 3.2: (a) Optical spectra of a signal comb (showing an absorption dip) and LO comb with equal average powers and a repetition rate ratio $\rho_r \approx 2:1$. Every other signal comb line is dotted to illustrate where the rf comb lines in (b) originate. (b) The rf comb seen on a detector in an electrical bandwidth of $f_{LO}/2$. A pair of gray lines illustrates the optical-to-rf mapping for a solid (dotted) rf comb line which in this specific example occur at even (odd) multiples of δf (k and k' are integers). Note that each "interferogram" in the time-domain will contain two unique bursts (corresponding to the solid and dotted rf combs) because the LO pulse train sweeps through a given signal pulse twice during each $\tau_{min} \equiv \delta f^{-1}$.

maximum optical bandwidth, $\Delta\nu_{max}$, that can be used without ambiguity is

$$\Delta\nu_{max} = \frac{f_{Sig} f_{LO}}{2\,\delta f} \quad , \tag{3.1}$$

where the required rf point spacing is

$$\delta f = \begin{cases} \left| \frac{f_{LO}}{\mathrm{nint}\left(\rho_r\right)} - f_{Sig} \right| , & \rho_r > 1 \\ \left| f_{LO} - \frac{f_{Sig}}{\mathrm{nint}\left(\rho_r^{-1}\right)} \right| , & \rho_r < 1 \end{cases} \tag{3.2}$$

where $\mathrm{nint}(x)$ is the nearest integer function. Note that the necessary rf point spacing is equal to the difference between the repetition rates for only conventional DCS (where $\rho_r \approx 1$). The maximum optical bandwidth can be doubled by using in-phase/quadrature detection [55,56]. The minimum amount of time required to resolve

these rf comb teeth is $\tau_{\min} \equiv \delta f^{-1}$ as set by the Nyquist criterion. Once resolved, the desired optical information can be extracted from the rf comb [4, 52, 53].

3.2 Simulation

The impact of various experimental parameters on the determination of the properties (i.e. line center, width, and amplitude) of some spectral feature can be quantified using a Monte Carlo method. Many randomly generated data sets with appropriate SNRs are each fit using a regression approach to extract the properties of the spectral feature. The errors between these measured values and the ones used to generate the data are then analyzed as a function of the experimental parameter to reveal its influence.

A number of approximations and assumptions have been made to simplify our analyses. First, we only consider a sample medium that possesses a single Lorentzian resonance and only analyze the absorption due to this resonance i.e. phase information is neglected. Second, we approximate the spectral envelopes of the signal and LO pulse trains as "top hats" whose width, $\Delta\nu$, is less than $\Delta\nu_{\max}$. In Sec. 3.2.1 the amplitude of the top hat is such that the average power of each beam is fixed while in Sec. 3.2.2 it is irrelevant. Third, the response function of the detector is assumed to be flat and the rf comb (which we assume lines up perfectly with the measurement frequency grid) is sampled at a rate of f_{LO}. Fourth, we assume that the offset frequency and repetition rate noise of the combs is negligible and that the dominant noise in the measurement may be modeled as additive complex white Gaussian noise, $N(\nu)$. Fifth, we assume that all systematic errors (e.g. baseline issues from etalon effects) are negligible.

These assumptions allow us to write the normalized, dimensionless, noise-free, optical-domain signal as

$$S(\nu) = \exp\left[2\pi i\, n'(\nu)\, L\nu/c\right] \exp\left[-\alpha(\nu)\, L/2\right] \quad , \tag{3.3}$$

which is only sampled at the signal comb frequencies within $\Delta\nu$ given by $\nu = kf_{\mathrm{Sig}} + f_{\mathrm{o}}$ where k is an integer, f_{o} is the signal comb offset frequency, $n'(\nu)$ is the real part of the sample medium's refractive index and L its length, and the absorption coefficient is

$$\alpha(\nu) = \frac{s}{L} \frac{\gamma^2}{\gamma^2 + (\nu - \nu_{\mathrm{c}})^2} \quad . \tag{3.4}$$

The parameters to be obtained from the noisy data are the center frequency, ν_{c}, half width at half maximum (HWHM), γ, and the strength, s. Since the phase information is neglected in this work, the noisy signal is

$$S_N(\nu) \equiv \left| \, S(\nu) + N(\nu) \, \right| \quad , \tag{3.5}$$

in which we expect the average SNR for a weakly absorbing sample to be

$$\mathrm{SNR}_{\rho_{\mathrm{r}}} = \sqrt{\rho_{\mathrm{r}}} \, \mathrm{SNR}_1 \tag{3.6}$$

where the corresponding SNR for conventional (i.e. $\rho_{\mathrm{r}} \approx 1$) DCS is [46]

$$\mathrm{SNR}_1 \equiv \frac{\sqrt{\tau}}{M} \frac{2P_{\mathrm{Sig}}}{\left[\mu^{-1} \left(\mathrm{NEP}\right)^2 + 4c_1 \eta^{-1} h\nu_0 P_{\mathrm{Sig}} + 2bc_2 \left(\mathrm{RIN}\right) P_{\mathrm{Sig}}^2\right]^{1/2}} \quad , \tag{3.7}$$

where τ is the acquisition time, $M \equiv \Delta\nu / f_{\mathrm{Sig}}$ is the number of resolved spectral elements (where $\Delta\nu$ is the acquisition optical bandwidth), P is the average laser power incident on the detector, NEP and η are the noise equivalent power (NEP) and efficiency of the detector respectively, $\mu \equiv P_{\mathrm{LO}} / P_{\mathrm{Sig}}$ is the laser power ratio, $h\nu_0$ is the average energy per photon, $c_1 \equiv (1 + \mu)/(2\mu)$, $c_2 \equiv (1 + \mu^2)/(2\mu)$, b is 1 (2) for balanced (unbalanced) detection, and RIN is the laser relative intensity noise (RIN) which is assumed to be the same for both pulse trains. Eq. 3.7 does not contain the

factor of 0.8 found in Ref. [46] because the laser spectra are assumed to be "top-hats" rather than Gaussians. From a frequency-domain perspective, the SNR expression in Eq. (3.6) arises from the facts that ρ_r more interferograms can be measured for any given τ and $\Delta\nu$ per Eqs. 3.1 and 3.2 (increasing the SNR by $\sqrt{\rho_\mathrm{r}}$ due to averaging), the amplitudes of the LO comb lines are $\sqrt{\rho_\mathrm{r}}$ times larger, and the frequency domain noise amplitude increases by $\sqrt{\rho_\mathrm{r}}$ because the sampling rate increases by ρ_r. In the time-domain, the same $\sqrt{\rho_\mathrm{r}}$ benefit from averaging and the same $\sqrt{\rho_\mathrm{r}}$ times greater noise amplitude from faster sampling exist in addition to a LO electric field amplitude that is $\sqrt{\rho_\mathrm{r}}$ greater on average.

3.2.1 Varying the repetition rates

For a fair comparison of repetition rates to be used in DCS, all other experimental parameters are fixed. In this case, Eq. (3.6) implies that the SNR scales with the repetition rates as

$$\mathrm{SNR} \propto \sqrt{f_\mathrm{Sig} f_\mathrm{LO}} \quad , \tag{3.8}$$

as shown in the leftmost panel of Fig. 3.4. Eq. 3.8 has recently been experimentally verified in Ref. [50] (note the reported SNRs are for the rf power as opposed to amplitude – the latter being the convention used in this work). For any given signal and LO comb repetition rates, the noisy signal $S_N(\nu)$ from Eq. (3.5) (with $L = 1$ and $s = 1$) was simulated independently many times with a SNR given by Eq. (3.8) and a random signal comb offset frequency, f_o, each time. Then, for each simulation, $-2\ln[S_N(\nu)]/L$ was fit to Eq. (3.4) using a nonlinear least-squares method following the Levenberg-Marquardt algorithm. Animations depicting this approach are shown in Fig. 3.3.

The idea behind any Monte Carlo technique is to quantify something (in this

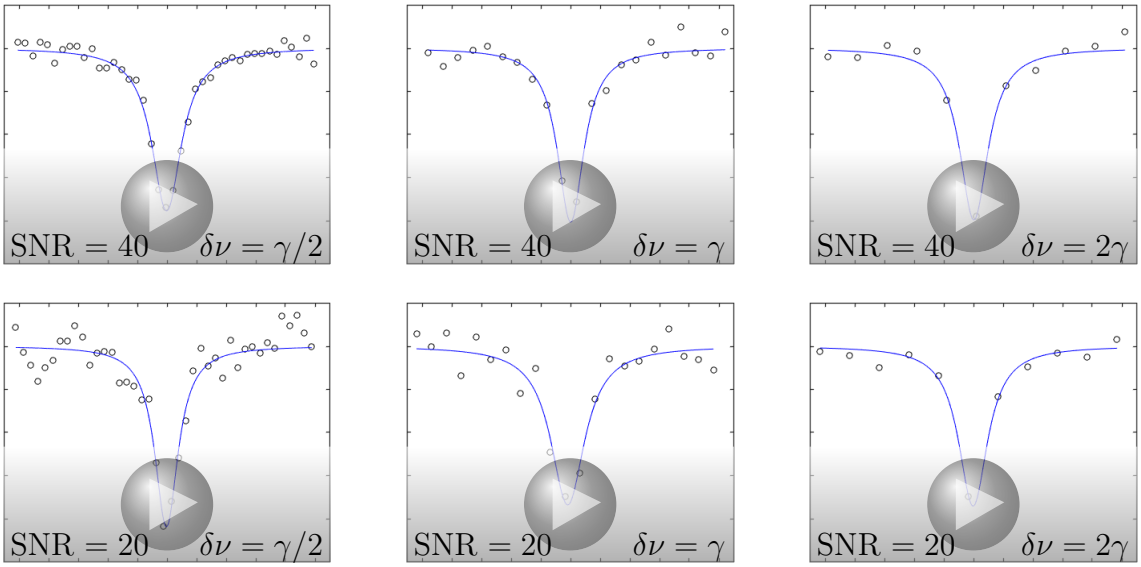

Figure 3.3: Monte Carlo animations. Black circles are noisy data and blue line is nonlinear least squares fit (see text for details). SNR is 40 (20) for top (bottom) row. The spectral point spacings are $\gamma/2$, γ, and 2γ for the left, middle, and right columns respectively.

case accuracy) that depends on a random process (i.e. Gaussian white noise) that is difficult or impossible to determine analytically. In this work, we wish to quantify the "jigglyness" of the fits in the animations shown in Fig. 3.3 as a function of the repetition rates. Thus, the standard deviation of the errors in the fitted center frequency (σ_c), half width at half maximum (HWHM) (σ_γ), and strength (σ_s) were then recorded for each simulation and are displayed in the rightmost three panels of Fig. 3.4.

In DCS the spectral point spacing, $\delta\nu$, is usually equal to the signal comb repetition rate, f_{Sig}. However, it is possible to achieve the same spectral point spacing with a signal comb repetition rate that is m times greater (where m is an integer) by using the spectral interleaving technique in which a series of m separate spectra are collected with each one having shifted signal comb lines [57, 58]. According to Eqs. (3.6) and (3.7) the SNR in the final interleaved spectrum is identical to one acquired without interleaving because the increase in the signal comb repetition rate by a factor of m (increasing the SNR by a factor $\sqrt{m}$) is counteracted by the reduction in

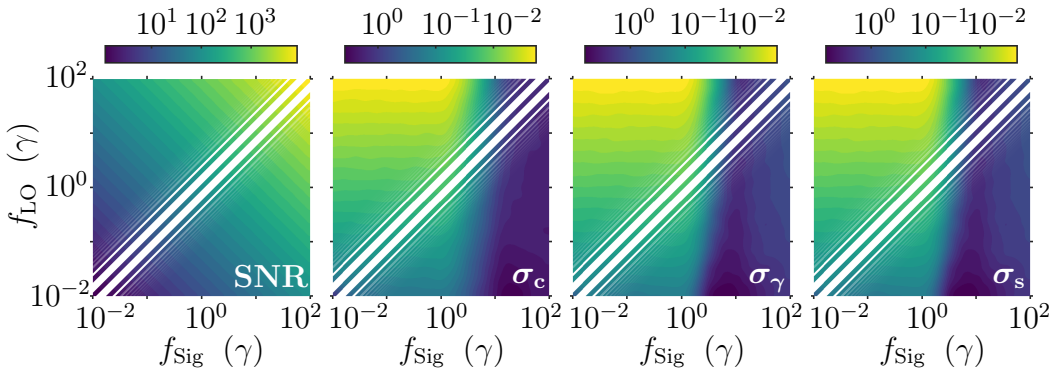

Figure 3.4: SNR and corresponding standard deviations of the errors in the fitted center frequency (σ_{c}), HWHM (σ_{γ}), and strength (σ_{s}) as functions of the repetition rates of the signal and LO combs (which have units of γ, the HWHM of the resonance). Conventional ($\rho_{\mathrm{r}} \approx 1$) DCS is the middle diagonal line on each plot while the first line above (below) the diagonal corresponds to $\rho_{\mathrm{r}} \approx 2$ ($\rho_{\mathrm{r}}^{-1} \approx 2$) and so forth. The space between neighboring lines shrinks exponentially due to the logarithmic axes.

acquisition time allowed for each measurement by a factor of m (decreasing the SNR by a factor $1/\sqrt{m}$) assuming all other parameters are the same. Thus, the results in Fig. 3.4 also apply to systems using the spectral interleaving technique but with the understanding that the horizontal axis should be interpreted as the final spectral point spacing, $\delta\nu$, which is f_{Sig}/m.

The core result of this work is that the repetition rates of the signal and LO combs greatly impact the error and uncertainty in the measured parameters of a Lorentzian resonance which is clearly shown in Fig. 3.4. When all other experimental parameters are fixed, it is ideal to have $f_{\mathrm{Sig}} \approx f_{\mathrm{LO}} \approx \gamma$ when using the traditional implementation of DCS in which $\rho_{\mathrm{r}} \approx 1$. However, by allowing the repetition rates to have a near-harmonic relationship, the uncertainty in the fit parameters can be orders of magnitude lower (assuming $f_{\mathrm{Sig}} \lessapprox \gamma$) resulting from an SNR that scales with $\sqrt{\rho_{\mathrm{r}}}$ (see Eq. 3.6 and the following paragraph). In this case, it is ideal to have any $f_{\mathrm{Sig}} \lessapprox \gamma$ in addition to the highest near-harmonic LO repetition rate that is feasible. Of course there is a lower limit set on the signal comb repetition rate that corresponds to the SNR approaching 1. Note that it is never beneficial to use a near-subharmonic LO comb as can be seen in Fig. 3.4 – this would imply that many signal pulses are never

sampled, wasting potential data. Although any signal comb repetition rate below the HWHM of the resonance should produce nearly the same fitting error for a given f_{LO} (see Fig. 3.4), there may be practical reasons to choose one f_{Sig} over another. For example, the higher the signal comb repetition rate, the less congested the rf comb will be because there are fewer comb teeth in a given electrical bandwidth. On the other hand, the higher the signal comb repetition rate, the less versatile that system will be in the sense that fewer samples will meet the $f_{\mathrm{Sig}} \lessapprox \gamma$ requirement.

It is important to note that these results apply strictly to linear measurements because Eq. (3.3) does not accurately describe nonlinear signals in general. For example, nonlinear interactions typically generate new comb lines rather than attenuate existing ones [59–63]. Indeed one nonlinear experiment demonstrated that the SNR actually decreases with increasing f_{Sig} (fixed laser output powers), which would imply that lower signal comb repetition rates are always better for nonlinear measurements due to the higher energy per pulse [16]. Of course there are other techniques that can affect the SNR even for linear measurements. For instance, a gated optical noise reduction technique can be used, which would favor a slower LO comb [64].

3.2.2 Varying the SNR and spectral point spacing

The results of Sec. 3.2.1 isolate the advantage stemming from the use of near-harmonically related repetition rates. However, most practical DCS systems have sufficiently different laser powers, detector efficiencies, types of dominant noise, etc., such that a more general simulation approach is necessary. For example, DCS has recently been performed with microresonator combs [15], but because these combs typically output only milliwatts of power [14], it is inappropriate to use the results from Fig. 3.4 to compare their ability to ascertain the properties of a spectral line to slower oscillators that have orders of magnitude more output power. To generalize our results, the simulations were performed again but instead of varying the repetition

rates, the independent parameters selected were the SNR and the spectral point spacing, $\delta\nu$. In all other respects the simulation process was identical to that described in Sec. 3.2.1. The results are displayed in Fig. 3.5.

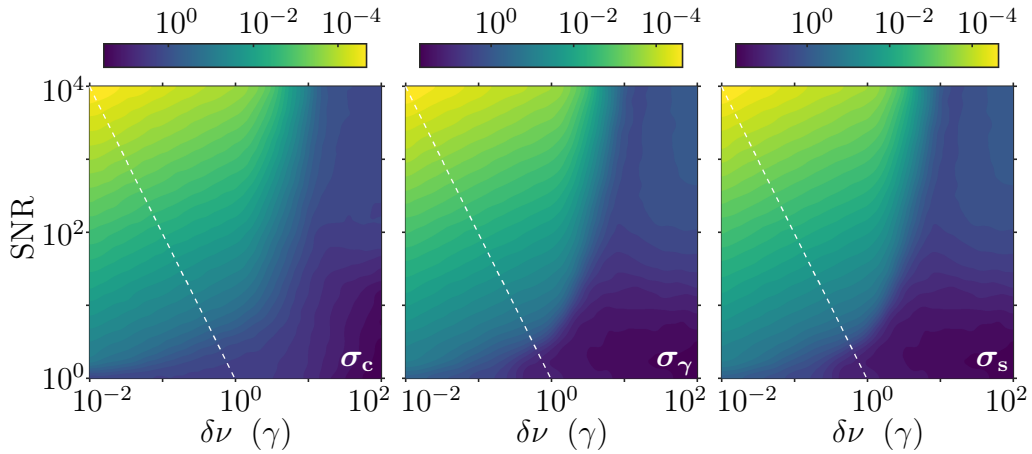

Figure 3.5: Standard deviation of the errors in the fitted center frequency (σ_c), HWHM (σ_γ), and strength (σ_s) as functions of the SNR and spectral point spacing, $\delta\nu$. The dashed white lines are gradients to help illustrate the relationship in Eq. (3.9).

Examining the left-hand side of each plot in Fig. 3.5 reveals that as long as $\delta\nu \lessapprox \gamma$ and the SNR is sufficiently high, then

$$\sigma \propto \frac{\sqrt{\delta\nu}}{\mathrm{SNR}} \tag{3.9}$$

where σ is the standard deviation of a given fit parameter. This is a known result in signal processing that also applies to Gaussian and Voigt profile line shapes as well [65]. This result is completely general and not specific to DCS because the simulation merely fits a Lorentzian to arbitrarily collected data. Any two spectroscopic systems can be compared regardless of the laser power used, acquisition time, etc., as long as the sample is weakly absorbing and the noise is white, Gaussian distributed, and dominates the systematic error. Therefore, Eq. 3.9 provides a useful tool to compare any two spectroscopic systems. It also explains in Fig. 3.4 why σ_c, σ_γ, and σ_s, are all proportional to $1/\sqrt{f_{\mathrm{LO}}}$ (with zero f_{Sig} dependence) for $f_{\mathrm{Sig}} \lessapprox \gamma$ when one considers

the SNR expression in Eq. 3.8 and the fact that $\delta\nu = f_{\text{Sig}}$.

All of the plots in Figs. 3.4 and 3.5 show that the error rapidly climbs for $\delta\nu \gtrapprox 3\gamma$. This observation corroborates one's intuition because zero (or only one) signal comb lines are "hitting the resonance." This condition means that the vast majority of the fitting involves the wings of the Lorentzian which are inherently insensitive to changes in ν_{c}, γ, and d (i.e. a large change in one of the parameters results in a minuscule change in data points far from line center) due to the exponential behavior of the wings. This lack of sensitive data points quickly leads to huge uncertainty in the fitted parameters *despite the fact that the* SNR *monotonically increases with* f_{Sig} (and therefore $\delta\nu$).

To verify the comprehensiveness of the results in Figs. 3.4 and 3.5 several series of simulations were performed. First, the overall patterns in the error plots remained the same as the SNR was scaled up and down over several orders of magnitude. Second, the number of data points over which the fitting was performed was varied between a fixed number of data points, a fixed frequency range of data points, and a hybrid approach. There was no significant effect on our results. Third, the strength of the resonance was varied. For sufficiently small strengths ($s \lessapprox 5$) the general patterns in our results were unaffected. However, for larger strengths the absorption becomes saturated and the comb lines containing the most critical information (those near line center) have drastically reduced signal-to-noise ratios. This situation leads to significantly less accurate fits overall.

3.3 Summary

We have isolated the impact of the DCS comb repetition rates on the standard deviation of the error, σ, of the measured parameters of a single Lorentzian resonance (assuming all else is equal, i.e. lasers powers, acquisition time, etc.) and found that there is a maximum suitable spectral point spacing, $\delta\nu \approx \gamma$, where γ is the HWHM

of the resonance. Because of this, the repetition rates that yield the smallest errors in the fit parameters do *not* possess the highest SNR. For the traditional implementation of DCS the ideal repetition rates are $f_{\mathrm{Sig}} \approx f_{\mathrm{LO}} \approx \gamma$ but even more accurate measurements can be made by allowing for arbitrary near-harmonic repetition rate ratios. In this case the ideal repetition rates are $f_{\mathrm{Sig}} \lessapprox \gamma$ and $f_{\mathrm{LO}} \to \infty$. In general, $\sigma \propto 1/\sqrt{f_{\mathrm{LO}}}$ (with zero f_{Sig} dependence) for $f_{\mathrm{Sig}} \lessapprox \gamma$. These are timely results given the recent advances in high-repetition-rate microresonator combs [15] and external repetition rate multiplying techniques [50, 66–68]. Since utilizing near-harmonic repetition rates requires only a slight modification to the rf-to-optical mapping process, any application of DCS where measuring the parameters of a spectral line is a top priority should readily receive higher accuracy and lower uncertainty by switching from similar to near-harmonic repetition rates assuming other experimental parameters remain more or less unchanged.

In practice, spectroscopic systems may differ wildly in everything from the type of dominant noise to the maximum allowable acquisition time. By running our simulations as a function of the SNR and spectral point spacing, $\delta\nu$, we identified a general fitting result, $\sigma \propto \sqrt{\delta\nu}\,/\,\mathrm{SNR}$, which can be used to compare any two spectroscopic systems despite their differences. In fact, this relationship can be used to compare even non-comb-based systems as long as the noise is predominately white and Gaussian distributed. Such a metric shows that while the SNR is important, efforts to reduce the spectral point spacing should also be made.

CHAPTER IV

Toward battery-powered DCS

One of the guiding visions for spectroscopy is to one day have a robust, battery powered, smartphone-sized device capable of high precision, high speed spectroscopic measurements. As mentioned in Chap. II, there are many frequency comb sources [14,18,21,23,25–30,32] some aligning with this vision more than others. For example, microresonator quality factors are now so high that when photonically integrated on a chip with a CW pump laser the entire device can be powered by a single AAA-battery [69]. Demonstrations of battery-powered, high precision, high speed spectroscopy (e.g. DCS) are on only a matter of time. In this chapter, efforts toward this end using a novel frequency comb source [31] are described.

4.1 Laser diode combs

In a normal laser cavity, the gain spectrum covers many cavity modes and during startup many of these modes may be above threshold. Whichever mode is the farthest above threshold (greatest gain minus loss) will power up exponentially faster than the other modes. Eventually, it will saturate the gain medium thereby balancing its loss and gain. Since the other modes don't have as much power, the saturation of the gain medium forces them below threshold (their losses dominate) and they will lose power until only the one mode is lasing. This phenomenon is called gain competition and

leads to CW lasing when the gain saturation affects all of the cavity modes equally. But in standing wave cavities, a phenomenon called spatial hole burning (SHB) can occur which reduces the gain experienced by the dominant lasing mode significantly more than others. SHB is caused when a standing wave within the cavity starts saturating the gain medium which occurs more at antinodes compared to nodes as shown in Fig. 4.1. Thus, the gain experienced by that cavity mode is significantly reduced. However, the other cavity modes, which have different wavelengths and hence different antinode locations, experience some reduction in gain but not as much as the dominant lasing mode – they benefit from the unused gain at the nodes of the dominant mode. Depending on the losses, it is therefore possible for these other modes to be above threshold and thus build up power rather than being extinguished as in the non-SHB case. Eventually, more SHB will saturate the gain of these other modes allowing more modes to lase until finally all of the gain is saturated. Thus, equilibrium can only be reached when multiple modes are lasing at the same time. If the device is intended to be single-mode then this is clearly a problem.

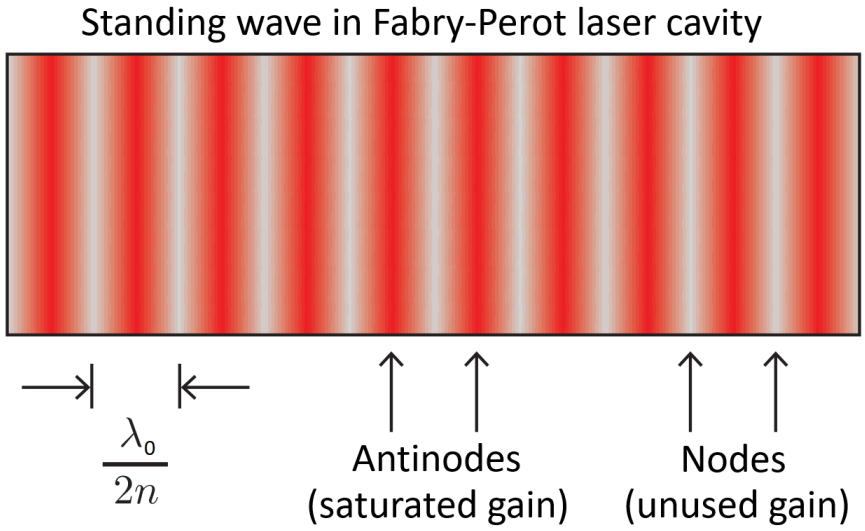

Figure 4.1: SHB in a Fabry-Perot laser cavity where the gain medium occupies the whole cavity. A standing wave saturates gain in its antinodes (red) leaving unused gain in the nodes (gray) which is used to drive the lasing of other cavity modes. Adapted from Mark Dong's PhD dissertation.

On the other hand, SHB can help facilitate the self mode-locking of a laser diode [30] although the physics were unclear until very recently [31]. Sometimes, this is referred to as phase-locking to distinguish it from traditional mode-locking – in the former the output is quasi-CW while in the latter pulses are generated. However, when the output of a phase-locked laser diode is sent through an appropriate dispersion compensating fiber, a train of pulses emerges [70]. Ultimately, the fundamental characteristic of both mode-locking and phase-locking is that a stable phase relationship between the multiple lasing modes exists. Per the discussion in Chap. II, this ensures that the output waveform is periodic and thus truly constitutes a comb (this assumes the frequency separation between modes is constant). SHB itself is not sufficient for mode-locking because it is an intensity-dependent effect rather than a carrier phase dependent effect and so it cannot couple the phases of individual modes to each other. For the laser diodes used in this chapter, FWM fixes the phases of the lasing modes relative to each other as described in Ref. [31]. These two effects constitute the necessary physics that enable passive frequency comb output from a single section laser diode – an attractive platform for future compact, low-power combs.

Mark Dong recently performed a detailed study of the physics of these laser diode combs and identified several important design considerations [31]. First, the carrier diffusion length should be small compared to the intra-cavity mode wavelengths in order to limit the ability of carriers injected into a node from diffusing and providing their gain within an antinode thereby increasing the magnitude of SHB. This can be accomplished by decreasing the carrier diffusion length, by decreasing the carrier mobility and/or lifetime (by choosing appropriate material parameters), and also by increasing the intra-cavity mode wavelengths, by operating with as red a spectrum as possible. Second, the cavity facets and injection current should encourage a high intra-cavity power so as to enhance both the SHB and FWM as much as possible. Lastly, a highly nonlinear active region should be chosen, again, to promote FWM.

Mark also fabricated many of these laser diode combs using these design principles – they typically produce several mW of power (although only about 1 mW can be coupled into a tapered SMF-28 optical fiber) with output spectra such as the one in Fig. 4.2. The repetition rate (about 20 GHz) is so high that the comb structure can be directly resolved on an optical spectrum analyzer (OSA) (approximately 6 GHz resolution). Of course performing spectroscopy like this would fail to capitalize on the comb structure. Throughout this chapter, all optical fibers are SMF-28 FC/APC (single mode, non-polarization maintaining).

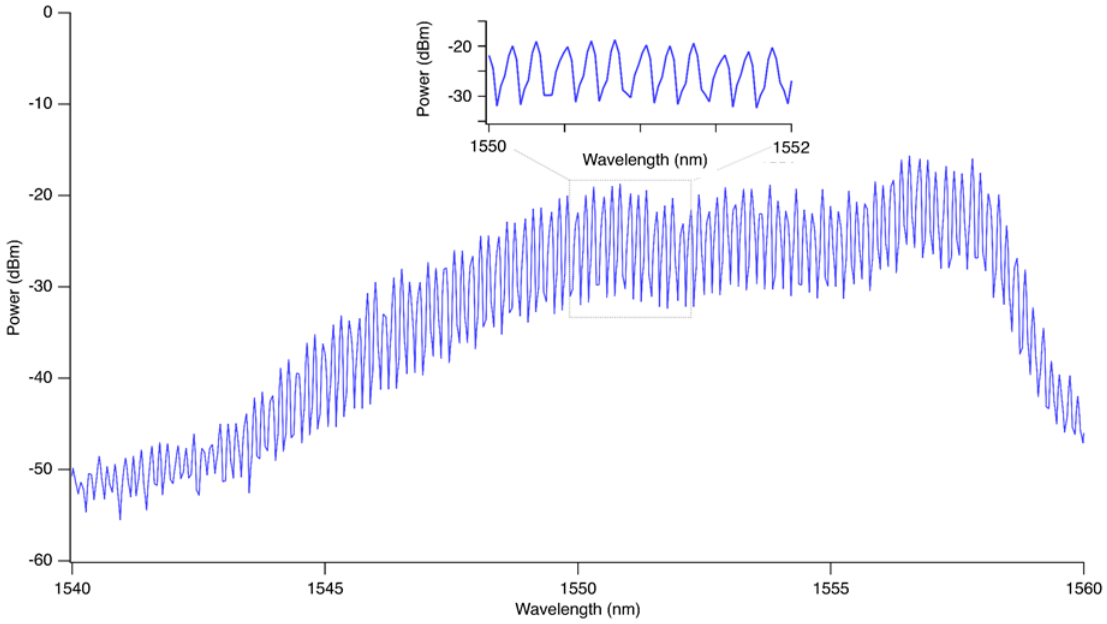

Figure 4.2: OSA trace of a typical laser diode comb having a repetition rate of 20 GHz. The comb teeth are directly resolvable since the OSA resolution is 6 GHz. Inset shows a zoom-in on a 2 nm range. Figure created by Matthew Day.

4.2 Characterization

Because of the novelty of the combs used in this chapter, it is worthwhile to characterize their performance, especially, their tunability, in order to qualify their prospects for real-world applications. For example, if used for an atomic clock, control of the repetition rate and offset frequency must enable the tunability of the comb

teeth by at least half a free spectral range (FSR) so that matching an atomic transition is always possible. To address this, we explored how the repetition rate and offset frequency depend on injection current and temperature. A Thorlabs ITC4000 series controller controlled both the injection current and temperature. Electrical contact for the injection current was made with a fine-tip electrical probe (see Fig. 4.3). The temperature was monitored with a thermistor in contact with the gold-coated plate underneath the chip and controlled via a thermo-electric cooler (TEC) underneath the laser diode (see Fig. 4.3). A typical laser diode (from batch vγ4) was selected for testing. Its output (coupled into a tapered optical fiber) was split using a 50:50 fiberized beam splitter with one exit port directed into an OSA and the other to a fast photodetector whose signal was monitored with an electrical spectrum analyzer (ESA) to detect the repetition rate. The injection current was varied (keeping the temperature fixed at 20°C) from 100 to 210 mA and OSA and ESA traces were saved after allowing several minutes for equilibration. The results are displayed in Fig. 4.4. In general, the comb smoothly red shifts (roughly 70 pm/mA) and the repetition rate increases with increasing injection current. While the spectrum changes relatively smoothly, the repetition rate, particularly its shape, is quite variable. Narrow repetition rates are always beneficial for applications so it is important to know which "knobs to turn" to improve the shape. Several "good" modes of operation (narrow repetition rate) can be identified in the ESA traces in Fig. 4.4. More comb teeth are visible at higher current as well, likely the result of the extra gain. Later, the temperature was varied (keeping the current fixed at 195 mA) from 18 to 23°C and OSA and ESA traces were saved after allowing several minutes for equilibration. The results are displayed in Fig. 4.5. In general, the comb smoothly red shifts with increasing temperature (roughly 60 pm/°C). But the repetition rate on average does not change much with temperature. However, the shape of the repetition rate does change – some traces even show nearly bi-modal behavior. This can also be argued

for some of the ESA traces for the current tuning data in Fig. 4.4.

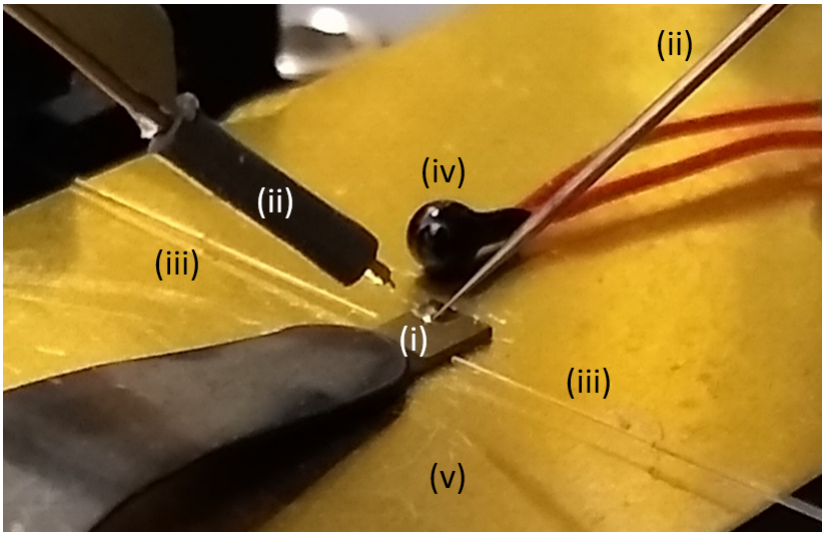

Figure 4.3: Laser diode combs. (i) Chip containing about 15 laser diodes. (ii) Electrical contact probes (the gold-coated plate underneath the chip is the return). (iii) Tapered fibers used to couple light from the combs. (iv) Thermistor. (v) Gold-coated plate with TEC underneath. An optical microscope allows alignment of the appropriate parts. The tapered fibers and electrical probes are mounted on 3-axis translation stages.

Changes in the repetition rate and offset frequency are difficult to determine visually from the OSA traces in Figs. 4.4 and 4.5. The ESA traces certainly do not reveal anything about the offset frequency and quantifying changes in the repetition rate could be difficult given the asymmetric shapes of some of the peaks. Therefore, the repetition rate and offset tunability was calculated in the following way. First, the individual comb teeth in the OSA traces were fit with Gaussian functions to identify their center frequencies at a resolution much better than the OSA resolution. A global fit was performed over all of these center frequencies to the model $\nu_n(x) = n f_{\mathrm{rep}}(x) + f_{\mathrm{off}}(x)$ where $f_{\mathrm{rep}}(x) = f_{\mathrm{rep}}^{(0)} + \beta_{\mathrm{rep}}\, x$, $f_{\mathrm{off}}(x) = f_{\mathrm{off}}^{(0)} + \beta_{\mathrm{off}}\, x$, n is the comb tooth mode number, and x is either the injection current or temperature. The offset frequency is constrained to be greater than 0 and less than f_{rep}. The results of this procedure are shown in Fig. 4.6. Tuning the current changes the repetition rate by -91 ± 9 MHz/A and the offset frequency by -4.2 ± 0.1 kHz/A. Tuning the

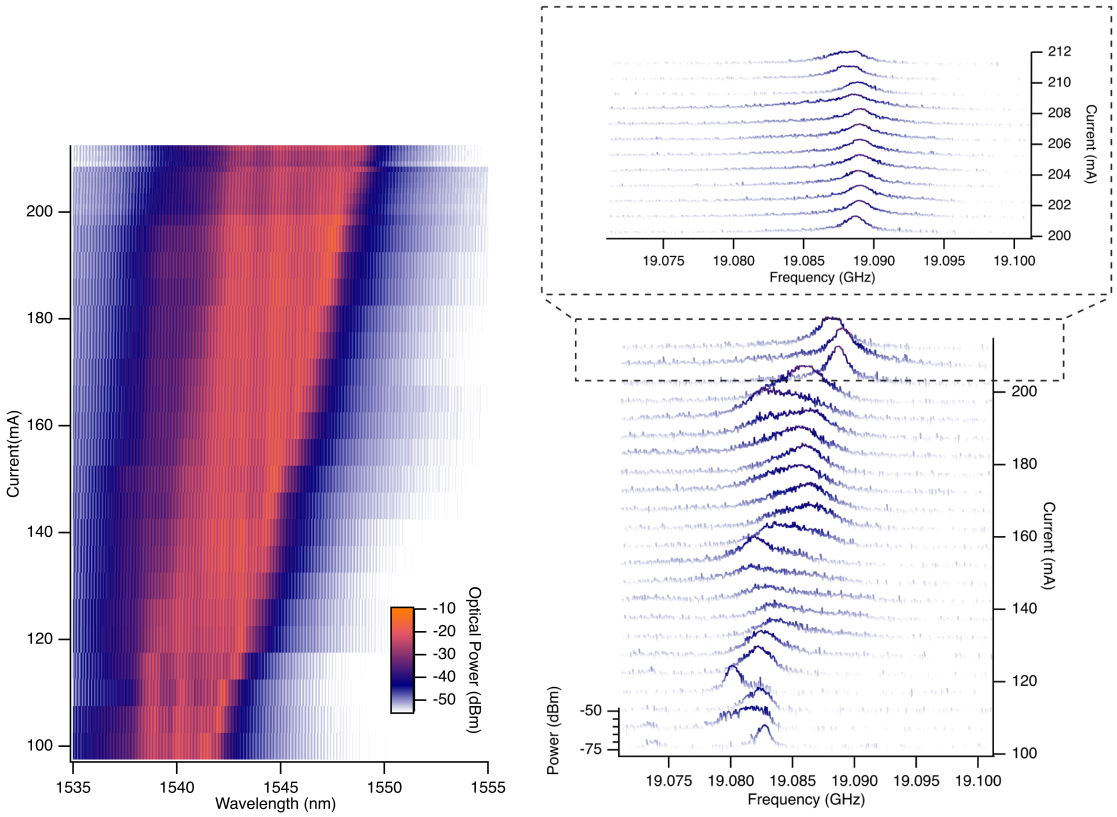

Figure 4.4: Comb dependence on injection current (temperature fixed at 20°C). (left) OSA traces. (right) ESA traces showing the first harmonic of the repetition rate. Figure created by Matthew Day.

temperature changes the repetition rate by -2 ± 3 MHz/°C and the offset frequency by -4.4 ± 0.2 kHz/°C.

4.3 DCS with laser diode combs

The simplicity, compactness, low power requirements, and "turn-key" nature of laser diode combs make them intriguing candidates for portable spectroscopic measurements. To demonstrate this, we aim to ultimately perform the first-ever battery-powered DCS experiment. As an initial step we performed DCS using standard laboratory-grade equipment (diagrammed in Fig. 4.7). The outputs from two laser diode combs on the same chip were coupled into tapered fibers and combined using a 50:50 splitter. One output is sent towards an OSA to monitor the comb spectra, their

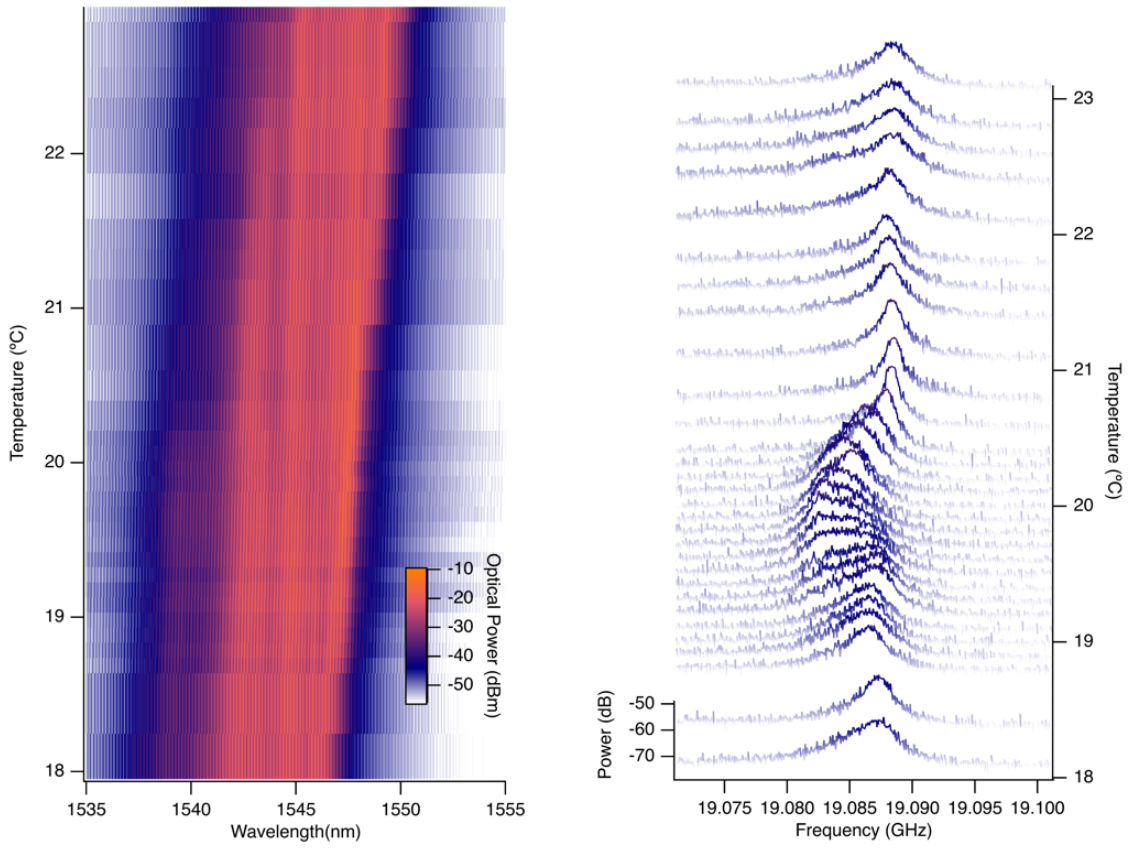

Figure 4.5: Comb dependence on temperature (injection current fixed at 195 mA). (left) OSA traces. (right) ESA traces showing the first harmonic of the repetition rate. Figure created by Matthew Day.

overlap, and relative spectral positioning of the CW laser to the combs. The other output is polarized using an in-line polarizer then transmitted through a $H^{13}C^{14}N$ gas cell (Wavelength References). A 90:10 splitter sends 90% of this light to a 45 GHz photodetector (Newport 1014). The other 10% is sent to the OSA. A CW reference laser (Q-photonics QDFBLD-1550-10, 2 MHz linewidth) is combined with the combs using the 90:10 splitter (10% is sent to the photodetector). Using a single photodetector guarantees that the relative timing of all signals is identical (excluding any electrical dispersion) which is critical for post-processing (see Appx. D). Polarization control paddles ensure that all lasers are co-polarized at the photodetector. Again, all fiber is SMF-28 FC/APC. The output from the photodetector is split sending half of the signal to the ESA for repetition rate monitoring and the other half to the data

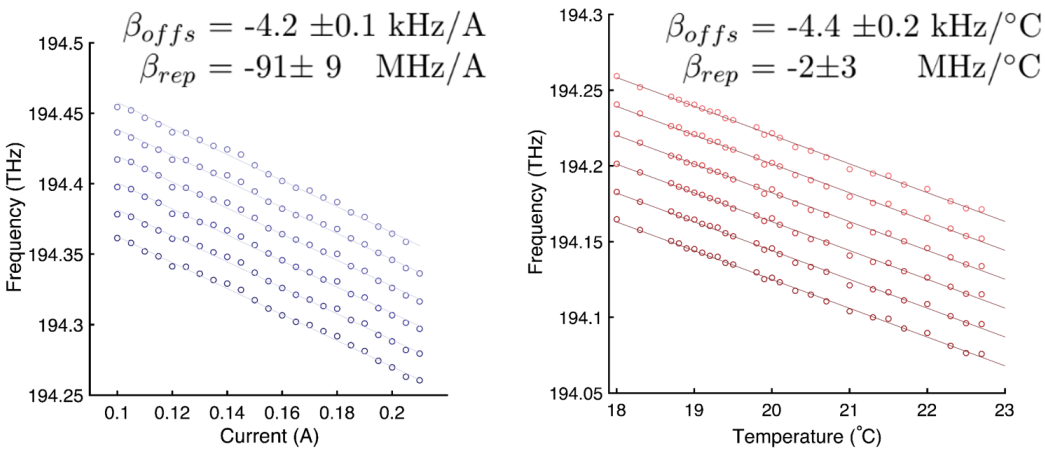

Figure 4.6: Tracking 6 teeth as functions of the injection current (left) and temperature (right) by fitting the individual teeth in the OSA traces in Figs. 4.4 and 4.5 to Gaussian functions to extract their center frequencies. The lines are the result of a global fit of all comb teeth (not just the 6 displayed here) to a model where the repetition rate and offset frequency were allowed to linearly depend on the temperature or injection current. The calculated linear dependencies are the β coefficients on each plot. Figure created by Matthew Day.

acquisition board (DAQ) board where it is digitized at 4 GS/s. Prior to digitization, the signal is amplified with 2 GHz bandwidth amplifiers to both low-pass filter the signal as well as fill up the amplitude range of the DAQ board. The DAQ spectrum and ESA and OSA traces are all observed in real-time while tweaking the comb spectra (via their injection currents and temperatures) as well as the CW laser center wavelength (via its temperature). The goal is to first get a stable dual-comb signal with sufficient comb spectra overlap where each comb repetition rate is as narrow as possible. Then, the CW laser center frequency is tuned such that the two CW-comb beat-notes fit within the 2 GHz digitizer bandwidth. Due to drifts, this usually requires two people. In principle, slow feedback loops could be used to eliminate the drifts.

Once digitized, the data is processed following the recipe in Appx. D. For the initial experiments, a different CW laser with a much smaller linewidth was used. An example result is shown in Fig. 4.8. The dips correspond to the absorption peaks in $H^{13}C^{14}N$.

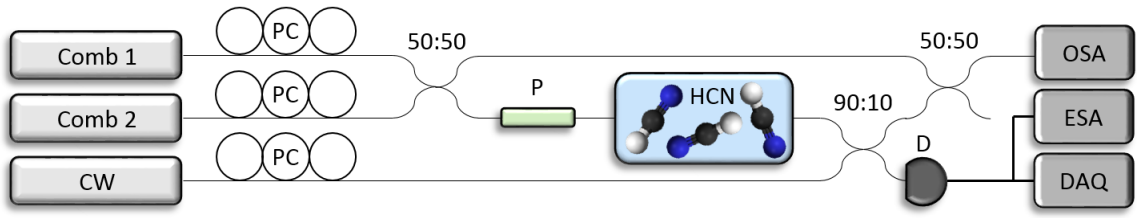

Figure 4.7: Experimental schematic for DCS using laser diode combs, a CW reference laser, and a single photodetector. All fiber is single mode SMF-28 FC/APC. The 90:10 splitter sends 90% of the comb light to the photodetector. PC = polarization controller, P = in-line polarizer, and D = 45 GHz photodetector.

4.4 Battery-powered operation

Having successfully demonstrated that these laser diode combs are capable of DCS, the next step toward battery-powered DCS is to design, build, and test, a battery-powered current controller to drive the combs. Since ordinary laser diodes are commonly battery-powered, many off-the-shelf components exist specifically suited for this task. We designed the circuit shown in Fig. 4.9 to drive current through a single laser diode – the circuit was duplicated so that two laser diodes could be driven independently. Several AA batteries are connected in parallel to supply a low-noise 3 V direct current (meaning zero frequency) (DC) signal to a voltage controlled current source (VCCS). The VCCS drives a fixed 350 mA through the laser diode and two potentiometers which are all connected in parallel (forming a current divider). The reason for using two potentiometers rather than just one is that, from a practical standpoint, more precise control over the injection current is possible (this is needed per the previous two sections). This makes generating and sustaining a quality dual-comb signal much easier. The potentiometers (10 Ω, 1-turn and 100 Ω, 10-turns) are connected in parallel giving an effective resistance of $R_{\text{eff}} = (1/R_1 + 1/R_2)^{-1}$. Precise current control is enabled when the two potentiometers have *significantly different resistances*. In this case, changes in the smaller resistance will have a much larger impact on R_{eff} than changes in the larger resistance. For example, when the

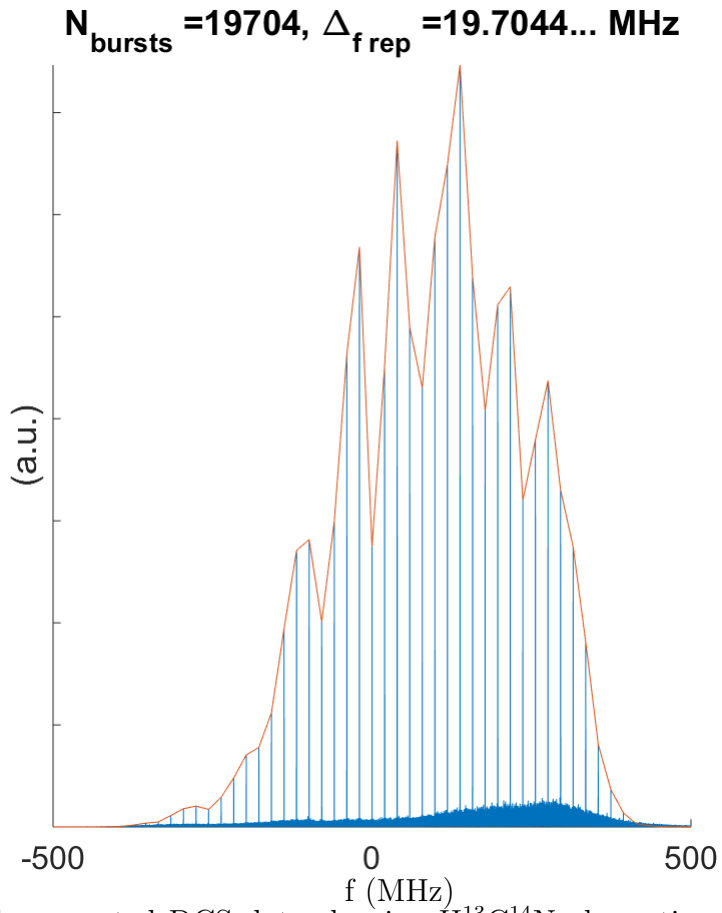

Figure 4.8: Fully corrected DCS data showing $H^{13}C^{14}N$ absorption dips. 19704 interferograms were recorded in 1 ms (corresponding to a difference in repetition rates of about 20 MHz). 39 comb teeth are visible corresponding to an optical bandwidth of about 6 nm. Each rf comb tooth is exactly 1 point wide indicating accurate noise correction.

potentiometers are set to 8.8 Ω and 88 Ω, the laser diode sees about 175 mA (its resistance near this point is 8 Ω). Changes to the 100 Ω potentiometer change the laser diode current about 10 times less than changes to the 10 Ω potentiometer. Thus, the 10 Ω potentiometer provides coarse current control and the 100 Ω potentiometer provides fine current control. Note that the potentiometers have the same number of Ohms per turn – ideally the fine-control potentiometer would have fewer Ohms per turn but we could not find such components. When either potentiometer provides zero resistance, all of the current in the circuit is diverted away from the laser diode. Switches allow an ammeter to monitor the current going through the battery and the

current through the laser diode separately and also disconnect the batteries from the VCCS. The duplicate circuits were constructed and packaged inside a small box (see Fig. 4.9). The power supply was tested and successfully powered a laser diode comb. The maximum operating time was only about 10 minutes for a single laser diode so more AA batteries were installed. In the future, the laser diode power requirements could be reduced by coating one facet with a high-reflectivity coating.

4.5 Discussion

The temperature and injection current tuning results in Fig. 4.6 should be interpreted with caution. The thermistor was placed on top of the gold-coated plate underneath the chip and no thermal paste was used so the thermal contact was small. Furthermore, the injection current likely heats the laser diode locally by a significant amount. Therefore, the measured temperature is probably quite different from the true temperature inside the diode which might also have a significant spatial dependence. The relationship between the measured and true temperature might be nonlinear but at the very least should be monotonic. Either way, the implication is that during the current tuning experiment the temperature was probably not constant. For the temperature tuning experiment, the current was indeed fixed, but the measured temperature values are probably not indicative of the true laser diode temperature. For future modeling endeavors these systematic errors should be taken into account.

For the DCS experiment, the results in Fig. 4.8 have been difficult to reproduce. It appears the diodes used had particularly low noise at the time of measurement. Specifically, the repetition rate noise relative to the difference in repetition rates is now larger than before. This limits the effectiveness of the digital difference frequency generation (DDFG) resampling approach (see Appx. D). To address this, a second CW laser with a different center frequency was combined with the first CW laser

and two additional beat notes with the combs were detected (4 total). Using these beat-notes allows access to an isolated, higher harmonic of Δf_{rep} than is possible with DDFG. Therefore, the resampling should be improved because the noise is more sensitively captured. This approach has so far been unsuccessful – I am actively trying to understand why. Another solution being explored is to correct the data using an extended Kalman filter [71]. This would be advantageous for battery-powered DCS because it completely eliminates the need for CW reference lasers thereby simplifying the experiment in exchange for more post-processing. On the other hand, the most straightforward approach to correcting the noise is to reduce it at its source. Experimentally, significant thermal coupling between the comb diodes makes it difficult to operate both in low-noise states simultaneously. One solution being considered is to cleave the chip in half to eliminate this coupling. Another solution is to apply some feedback to the combs to stabilize their repetition rates. Initial attempts at locking the repetition rate to a function generator by applying feedback to the injection current (similar to the approach used for the Ti:sapphire combs described in Appx. C) has yielded mixed results. So far, it appears that only drifts can be removed. A stable CW laser was also coupled into the laser diode cavity to lock-down one of the optical comb teeth. This appears to work, but has little to no effect on the repetition rate. Other approaches being considered are to strongly modulate the injection current with a narrow-band frequency close to the repetition rate and to apply narrow sidebands at the repetition rate to a CW laser being coupled into the laser diode cavity. Once the data in Fig. 4.8 can be re-produced, efforts to demonstrate battery-powered DCS will be made.

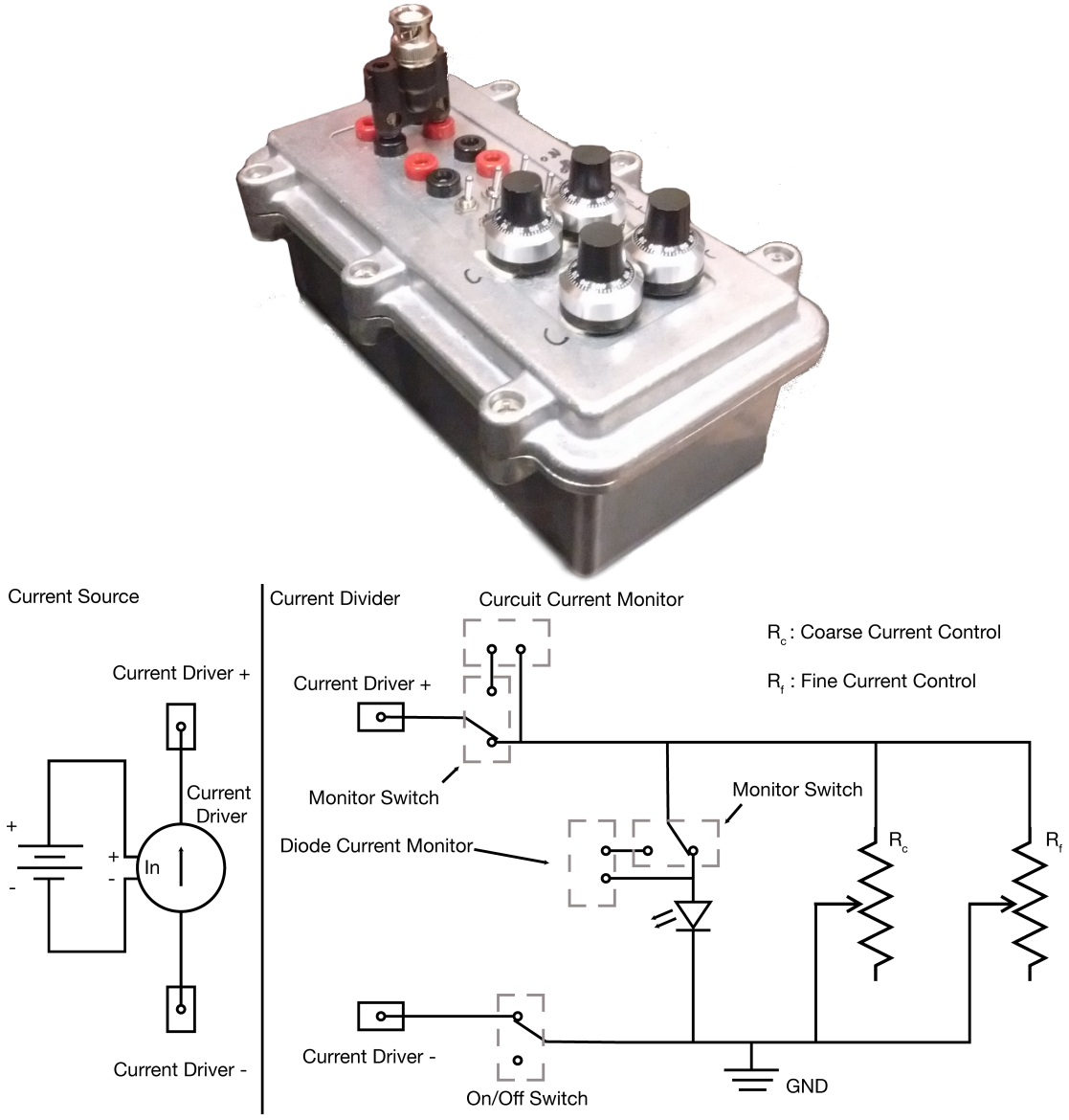

Figure 4.9: (top) Picture of the fully packaged dual laser diode current controller. An ammeter can be connected via the banana jacks. The switches disconnect the batteries from the VCCS and also enable/disable current going through the ammeter. Coarse and fine current control is enabled by potentiometers (see text). (bottom) Circuit for a single laser diode current controller.

CHAPTER V

Four-wave mixing hyperspectral imaging

The frequency-comb-based spectroscopy applications presented so far have all considered a single acquisition period using a single photodetector. Any material in the beam path imprints its spectral properties on the outgoing light but this reveals nothing about the material's spatial properties. For this, some form of imaging is required. For some applications, simple techniques like acquiring gray-scale images by integrating the white light reflected from a material may be sufficient to determine the spatial properties of interest. But sometimes it is necessary to achieve both rich spectral and spatial information simultaneously. Enter hyperspectral imaging.

Hyperspectral images are images where every pixel also contains spectral information and are thus 3-dimensional. One example of a hyperspectral imager you should be very familiar with is your eye. The cones on your retina provide measurements of the amount of red, green, and blue light. This is very limited spectral information, but it illustrates the concept of hyperspectral imaging and is indeed powerful enough to be a significant biological advantage for many species. Technically your eyes only perform "multispectral" imaging because they acquire information in only 3 spectral bands. Commonly accepted definitions state that data in more than 15 spectral bands is necessary for classification as hyperspectral imaging [72]. Hyperspectral imaging is being applied to a diverse number of fields including agriculture [73], food

inspection [74], biology [75], astronomy [76], etc. There are even commercial, hand-held hyperspectral imagers available now [77] and detailed open-access instructions to build your own imager using 3D-printed and off-the-shelf parts [78]. Lastly, for DCS-based hyperspectral imaging, one might suspect that a photodetector array [79, 80] or lock-in charge-coupled device (CCD) [81] is necessary. However, so-called "single pixel" techniques exist that require only one photodetector thereby reducing signal analysis complexity at the cost of requiring serial measurements. For example, a recent demonstration of DCS-based hyperspectral imaging used a Hadamard-transform-based technique [82]. Of course, mechanical raster-scanning is always an option, but is less robust and likely slower because moving parts are required.

All of these examples utilize linear techniques which, as mentioned in Chap. I, are simpler but have disadvantages compared to nonlinear techniques. In the context of imaging, nonlinear methods have intrinsically higher spatial resolution (since the square or cube of a Gaussian spot has a smaller spot size), higher sensitivity to the environment, and the ability to probe various types of coupling. For example, tailored gold nanorods enable plasmonically enhanced FWM [83]. Like all plasmon-based phenomena they should be highly sensitive to changes in their environment meaning if implanted in a sample they could offer a mechanism to enhance signals from small features. Nonlinear hyperspectral imaging techniques also exist such as coherent anti-Stokes Raman scattering (CARS) imaging [84] which can also be accomplished using frequency combs [85]. Lastly, there have also been hyperspectral images formed using MDCS [86], but the technique used requires delay stages. The resulting image revealed coherent coupling between distant excitons.

The frequency-comb-based CARS example mentioned above (Ref. [85]) successfully achieved the same benefits from combs as DCS did with respect to FTS. However, it also acquired the fundamental limitation of any CARS technique – it relies on Raman shifts which strictly limits the number of samples it can be applied to.

In this chapter, a new FWM technique hyperspectral imaging technique is presented that can in principle be applied universally to any material.

5.1 Experimental design

One of the fundamental challenges with nonlinear spectroscopy lies is distinguishing a nonlinear signal from a linear one (see also discussion in Chap. VI). This is why CARS uses the anti-Stokes Raman shift – it spectrally shifts the FWM signal away from the pumps. This enables the use of a simple optical filter to isolate the FWM signal for high sensitivity detection. Without this filter, the FWM signal would be a tiny signal on top of a large linear signal from the pumps and would require an enormous dynamic range of the detector. In principle a box geometry [87] could be used to eliminate light from the pumps, but since most imaging techniques are often employed for microscopy, a collinear geometry is preferred because it yields higher spatial resolution.

So, how else can FWM signals be isolated from linear ones? We combined a comb-based version of "frequency tagging" [88] with the standard dual-comb read-out technique. This technique was originally demonstrated by Bachana Lomsadze [60]. In comb terms, the concept behind frequency tagging is that the carrier-envelope offset frequency of the three pump beams that generate the FWM are all different but the repetition rates are all the same. In this way, any coherently generated FWM signal that depends on all three pump beams will have a carrier-envelope offset frequency that is the sum or difference of those of the three pumps (e.g. $f_{\mathrm{FWM,off}} = -f_{\mathrm{A,off}} + f_{\mathrm{B,off}} + f_{\mathrm{C,off}}$. This implies that when heterodyned with a local oscillator beam, the FWM and linear signals are spectrally isolated in the rf-domain. This allows the use of rf filtering to suppress unwanted signals. Because the linear signals are still present on the detector there is the disadvantage that they will contribute shot noise to the FWM signal. By using two combs, one for the pump and one for the

local oscillator, all of the advantages of combs compared to mechanical delay stages are also obtained allowing the FWM signal to be rapidly spectrally resolved.

Fig. 5.3 shows a schematic representation of the experiment we performed. The pump comb is split using a polarizing beam splitter (PBS) into two arms having nearly equal lengths (this was controlled using a mechanical delay stage to optimize the FWM signal which usually occurred by adding a slight extra delay to the arm whose pulses acted twice). The non-delay-stage arm has an AOM and only a first-order diffracted beam is collected. The two beams are recombined on a PBS. A CCD is placed both near to and far from the exit port of the PBS. The CCD spots from both beams are made to overlap to achieve spatial and wave vector overlap which is critical for heterodyne detection. Wavefront curvature matching was not monitored, but all lasers were telescoped to ensure highly collimated outputs. This technique is used extensively throughout this entire work. The orthogonally polarized beams are then projected together using a 45° rotated polarizer. This effectively yields two co-propagating, co-polarized combs with identical repetition rates (93.500129(88) MHz) but offset frequencies that are 80 MHz apart (the frequency at which the AOM is driven). Physically the AOM shifts the comb lines by adding both momentum and energy via three-wave mixing with the acoustic waves within the crystal [89]. Propagation through a Faraday isolator at this point is necessary to prevent reflections from the sample from destabilizing the laser. Usually back reflections can be avoided through slight misalignment, but this will not work when the reflection occurs in the focal plane of a high numerical aperture (NA) optic. This pump beam is then rotated to s-polarization using a half-wave plate (HWP) and reflected off of a PBS. A 24 nm optical band-pass filter centered around 800 nm filtered both beams to avoid exciting unwanted transitions. A quarter-wave plate (QWP) converts the pump beam polarization to circular (the handedness does not matter). Two mirrors bonded with highly flexible epoxy to 20 μm piezoelectric actuators provide pitch and yaw

control. I built these devices (see Fig. 5.2) inspired by a design from Eric Martin. The piezoelectric actuators are controlled using an obsolete Thorlabs controller (Thorlabs MDT693A) which is connected to a computer for remote control via Labview. The first mirror is 4f imaged onto the second mirror and the second mirror is 4f imaged onto the back of a 10x, 0.25 NA microscope objective. Each 4f-imaging system used positive lenses and incorporated a magnification (-12.5/10 and -15/10 respectively) of the beam in order to match the beam diameter to the objective aperture diameter to maximize the use of the available numerical aperture. This also resulted in an asymmetry in the dimensions of the raster scanning area. It would have been more advantageous for only the second 4f system to include magnification but both physical space and lens availability prohibited this option. To compensate the asymmetry allowing for square images, the vertical scanning piezo was driven to only 74% of its maximum range. The 74% number was calculated by taking images (described below) of the laser spot at the four corners of the rectangular raster scanning area using a test sample with gold electrodes whose dimensions were known precisely – this also provided a means to calibrate piezo-controller voltage to physical distance. The microscope objective focused the joint pump beam onto the sample. The pitch and yaw control enabled by this setup allow the laser spot to be raster scanned across the sample surface thereby enabling pixel-by-pixel sequential imaging.

The sample was a stack of 10 GaAs quantum wells (QWs) with 10 nm separation mounted on a sapphire substrate in a high-vacuum, flow cryostat and cooled to 6-8 Kelvin using Helium [90]. Relevant to this work are two absorption peaks corresponding to $n = 1$ light-hole and heavy-hole excitons (typical linear absorption is shown in Fig. 5.1 reproduced from Ref. [90] - note the data is *not* from the sample used in this work). For alignment verification and white-light imaging, removable 50:50 beam splitters allowed a gooseneck white light source to illuminate the sample through the objective and the reflected light was collected using the second beam splitter and

focused to create an image of the sample on a CCD. The laser spot on the sample could also be simultaneously observed in this way. By translating the cryostat a moderate astigmatism of both pump beams was observed by monitoring the shape of the laser spot on the CCD image. As the cryostat was translated longitudinally the spot achieved its smallest size in one direction first (so it was an ellipse) then became a medium-sized circle, then the other orthogonal direction reached its minimum size (again resulting in an ellipse). This astigmatism results in an inability to achieve a diffraction-limited spot in both directions simultaneously. The maximum FWM signal occurred with the cryostat translated such that the spot was in between in the max ellipticity and circular states. Although the FWM signal is phase-matched in the forward direction for this collinear excitation scheme, the strong absorption of the sample limits the effective excitation depth to an amount comparable to the wavelength of the pump light within the medium (approximately 200 nm). Thus, appreciable FWM can be emitted in the backward direction.

The FWM and reflected linear signals (all having the same-handedness circular polarization which is opposite to that of the incident pumps) propagate back through the objective and 4f systems. In this way, the deflection caused by each piezo-actuated mirror is undone and the pointing and position of the backward-direction beams is fixed at the QWP throughout the raster scanning process. The QWP converts the circular polarization into p-polarization since the handedness is opposite that of the incident pump beam. These beams are combined with the local oscillator comb (with repetition rate 65 Hz lower than pump) using another PBS. One of the outputs is used to detect the linear and FWM signals and the other is directed to another PBS where it combines with two reference CW lasers isolated with Faraday isolators (Toptica DL100 external cavity diode lasers) to monitor repetition rate and offset frequency fluctuations. HWPs control how much light is used for the error signals.

The topmost detector (see Fig. 5.3(a)) measures beating between all of the optical

comb lines including the FWM. Prior to this detector, a 24 nm optical band-pass filter centered around 800 nm filtered all beams. All detectors have 45° rotated polarizers in front of them to project the polarizations onto the same axis – otherwise no heterodyning would occur. The remaining two detectors measure beat notes between the CW reference lasers and the non-AOM-shifted comb 1 teeth and comb 2 (in principle the AOM arm should have been monitored as well but this proved unnecessary). The purpose is to measure all repetition rate and offset frequency noise on each laser at the exact PBS where the all beams are combined (any noise after this PBS is mutual to all beams). The optical frequencies of the CW lasers were also measured using a wavemeter (Bristol) to provide coarse spectral calibration for the acquired data (center frequencies of 370.404(76) THz and 377.115(38) THz). Prior to these detectors and after the polarizers, the combined beams are rotated to p-polarization using more HWPs (to optimize diffraction efficiency) and diffracted off of a grating in a near-Littrow configuration. The diffracted beams are allowed to propagate a long distance. This suppresses both inter-comb beat notes (i.e. dual-comb like signals) and intra-comb beat notes (i.e. harmonics of the repetition rates) on the detectors which would corrupt the error signals and increase the noise. It also allows more CW power to be sent to the each detector before electrical saturation occurs thereby increasing the SNR of the error signals. These detectors were amplified whereas the signal detector was merely biased. The reason for using only a biased detector was that intra-comb beat notes (i.e. harmonics of the repetition rate) dominate the signal and would saturate electrical amplifiers quickly. Using a biased detector allows these unwanted signals to be electrically filtered out using low pass filters. However, without a high-speed transimpedance amplifier we chose to use a 50 Ohm terminator to convert our current signal into a voltage signal for subsequent amplification. This is not ideal because it adds substantial Johnson noise. Recently, a balanced amplified photodetector [48] has been purchased to remedy this for future work in Chap. VII.

The four CW beat notes are individually electrically filtered, then combined using rf power combiners, then amplified to a peak-to-peak voltage level slightly below that of the DAQ board. The FWM signal and two linear dual-comb signals from the signal detector (see Fig. 5.3(b)) were split up and individually amplified then recombined such that the rf power in each signal was similar and their total peak-to-peak voltage was again slightly below the maximum range of the DAQ board to maximize the use of the DAQ dynamic range. These two channels were digitized at 250 MS/s. A Labview program raster scanned the laser spot, waited several hundred ms after the movement command to allow settling of the physical parts, then acquired data from the DAQ board, then repeated until 400 pixels of data were recorded. Due to the large size of the files that had to be saved after digitization for each pixel, each hyperspectral image took about 30 min of laboratory time to record even though only about 45 seconds worth of data was collected. This could be remedied using real-time techniques [91–93] which allow for significantly smaller file sizes. Further acquisition speed gains could come via faster raster scan control enabled for example by resonant galvanometer mirrors.

5.2 Results

Once collected, the data was post-processed in Matlab using the techniques in Appx. D particularly with respect to Ref. [94]. Only the heterodyne signals between the FWM and the LO are presented below. Linear signals were also processed, but produced unreliable data – at this time we are unsure why. Initial results are shown in Fig. 5.4. Two months later, after processing the initial results and re-epoxying the piezoelectric actuators to the mirrors, which increased the raster scanning area, more images were collected as shown in Fig. 5.5-5.9. These animations can only be viewed with an Adobe-brand software. Cold (6-8 K, during experiment) and hot (standard temperature and pressure (STP), 6 months later) white light images of the sample

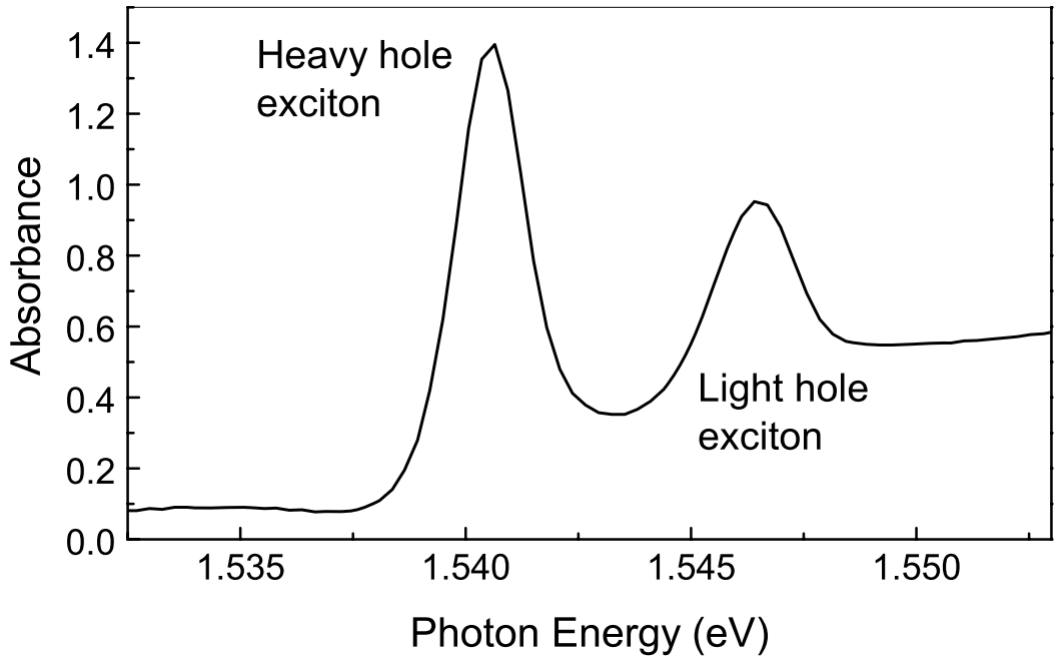

Figure 5.1: Typical linear absorption of a $Al_{0.3}Ga_{0.7}As/GaAs/Al_{0.3}Ga_{0.7}As$ QW at 10 K. The data is *not* from the sample used in this work. Reproduced from Ref. [90].

were also collected as shown in Figs. 5.4-5.9.

5.3 Discussion

The heavy-hole and light-hole exciton spectral features shown Fig. 5.1 are also present in the FWM hyperspectral images - Figs. 5.4-5.9. However, they show up at different wavelengths/energies. One parameter that affects these features is spatial confinement – more confinement leads to more red-shifting of the exciton features relative to the band edge which is itself blue-shifted by confinement [90]. Confinement also lifts the valence band gap degeneracy. Basically, forcing the electron and hole to stay closer together increases their binding energy so it requires more energy to dissociate them resulting in a red-shifting of the absorption feature relative to the band edge. This also depends on the polarization of the excitation beam and the spatial structure of the confinement. Both the band gap and exciton features are also temperature dependent. Another parameter that can shift exciton features is

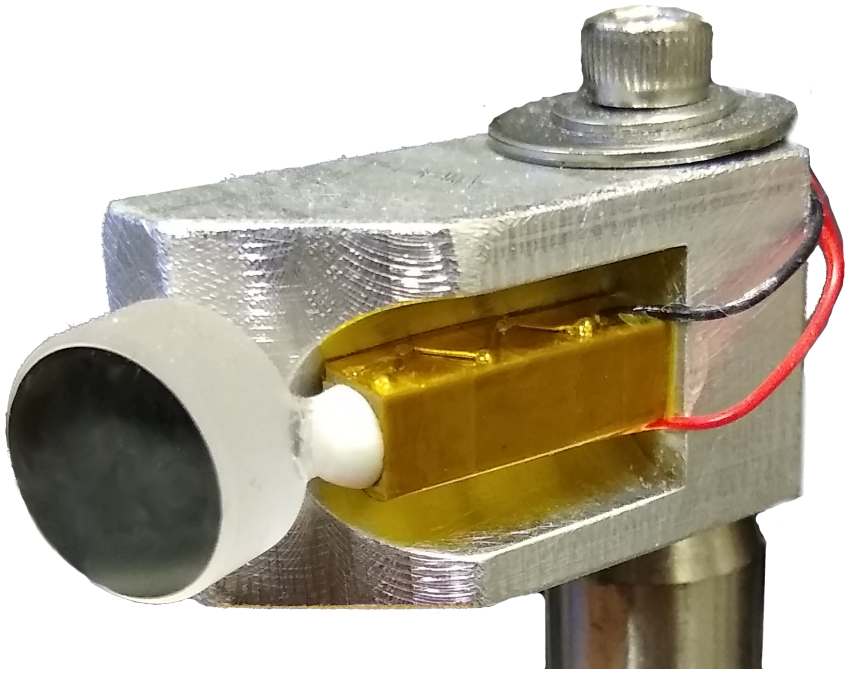

Figure 5.2: Homemade piezoelectric actuated mirror. The mirror is epoxied to the aluminum mount and the ball-cap end of the piezoelectric actuator using a highly flexible epoxy (otherwise no rotation would be possible). The bottom of the piezoelectric actuator is super glued to the aluminum mount.

the Stark effect (described in Appx. A). For excitons the Stark effect is predicted to be much larger than for atoms per Eq. (A.46) because the binding energy is typically only a few to tens of meV [90]. However, Eq. (A.46) does not pertain to the "ground state" ($n = 1$) exciton features examined in this work because they correspond to non-degenerate states (see Sec. A.7). That being said, an inverse correlation to the binding energy should still be expected for the quadratic Stark effect which affects all exciton features (see the quadratic dependence in Ref. [95] for example). For bulk excitons, the low binding energy also means that the electron and hole dissociate from each other at relatively small electric field strengths – given an exciton diameter of 30 nm and binding energy of 10 meV, the characteristic field strength required for dissociation is a modest 0.3 MV/m. Near and beyond this critical strength, the exciton lifetime is greatly reduced. Thus, the absorption related to these features becomes severely broadened thereby diminishing peak visibility. On the other hand,

when the exciton is spatially confined (e.g. in a QW, quantum wire, or quantum dot), the electric field strength required for dissociation is greatly increased allowing for strongly perturbed, but still bound, states to exist. Essentially the confinement prevents the dissociation problem plaguing the bulk exciton Stark shift. Furthermore, the confinement greatly enhances the quadratic Stark coefficient (resonance shift per square electric field) because the potential well acts a large anharmonic restoring force (assuming the potential well width is of similar scale or smaller than the exciton diameter). Thus confinement allows incredibly large Stark shifts to occur by leveraging the anharmonic restoring force of the potential well and the small binding energy of the excitons (leading to huge Stark shifts via Eq. (A.46)) while preventing their dissociation. The combination of confinement and the Stark effect is called the quantum confined Stark effect (QCSE) [95]. Shifts of tens of meV are possible in GaAs QWs [95]. The QCSE is particularly relevant when the materials used are non-centrosymmetric (which both GaAs and AlGaAs are) because these materials also exhibit the piezoelectric effect. Thus, any strain within the sample will produce a static electric field which leads to a QCSE. Continuum states are also impacted by an applied electric field via the Franz-Keldysh effect which puts a tail on the band absorption edge and some oscillations above the edge [96]. And just like excitons, confinement enhances the Franz-Keldysh effect leading to the quantum confined Franz-Keldysh effect [97]. Strain by itself has also been observed to spectrally shift the exciton features in bulk GaAs by multiple meV through direct altering of the band structure [98]. Interestingly, neither Ref. [98] nor Ref. [95] mention the others effect despite strain and electric field being directly linked through the piezoelectric and inverse piezoelectric effects. That is, it makes no sense to consider one but not the other. Perhaps an interesting experiment would be to disentangle strain-induced shifts from those resulting from the QCSE.

So what is causing the spatial dependence of the exciton FWM spectral features

seen in Figs. 5.4-5.9? It certainly cannot be spatial temperature variation because there is no reason to expect the sample to not be uniformly cooled. Likewise, spatial confinement variation could explain the results but since the sample is grown using molecular beam epitaxy this is also unlikely. On the contrary, a spatially varying QCSE resulting from spatially varying strain could both explain the results and be explained by the combination of the "battered" nature of the sample and a thermal expansion coefficient mismatch with the sapphire substrate. This is further corroborated by the hot and cold white light images in Figs. 5.4-5.9. The cold images clearly show many spatial features that match with the hyperspectral images. The hot images, however, show far fewer similarities - particularly only cracks within the sample. Therefore, the hyperspectral features can only be explained by a temperature dependent phenomenon. The "crater-like" nature of the features unique to some of the cold images suggests that cooling the sample introduces significant strain fields within the sample especially near cracks. As mentioned earlier, this strain alone can account the spectral shifting of the exciton features. The temperature dependence of these strain fields could be explained by a difference in thermal expansion coefficients between the QWs and the sapphire substrate. Lastly, the QCSE can produce shifts of tens of meV in GaAs QWs – much greater than the shifts in Figs. 5.4-5.9. However, without an independent strain imaging technique, this hypothesis is impossible to test so at this point it is plausible at best. Note that these shifts should be revealed by linear techniques as well.

The focus of the work presented in this chapter was to demonstrate a spectrally precise and potentially rapid technique capable of generating near-diffraction limited FWM hyperspectral images. Of particular interest was demonstrating its advantages over CARS imaging, namely that it is a universal technique that does not rely on the sample having a Raman shift. As a proof-of-concept, this work accomplished these goals, but leaves much room improvement. The ultimate FWM hyperspectral

imaging technique would leverage the high precision, bandwidth compression, and acquisition speed enabled by frequency combs with the universality and rich information of MDCS. What a perfect segue to the next chapter...

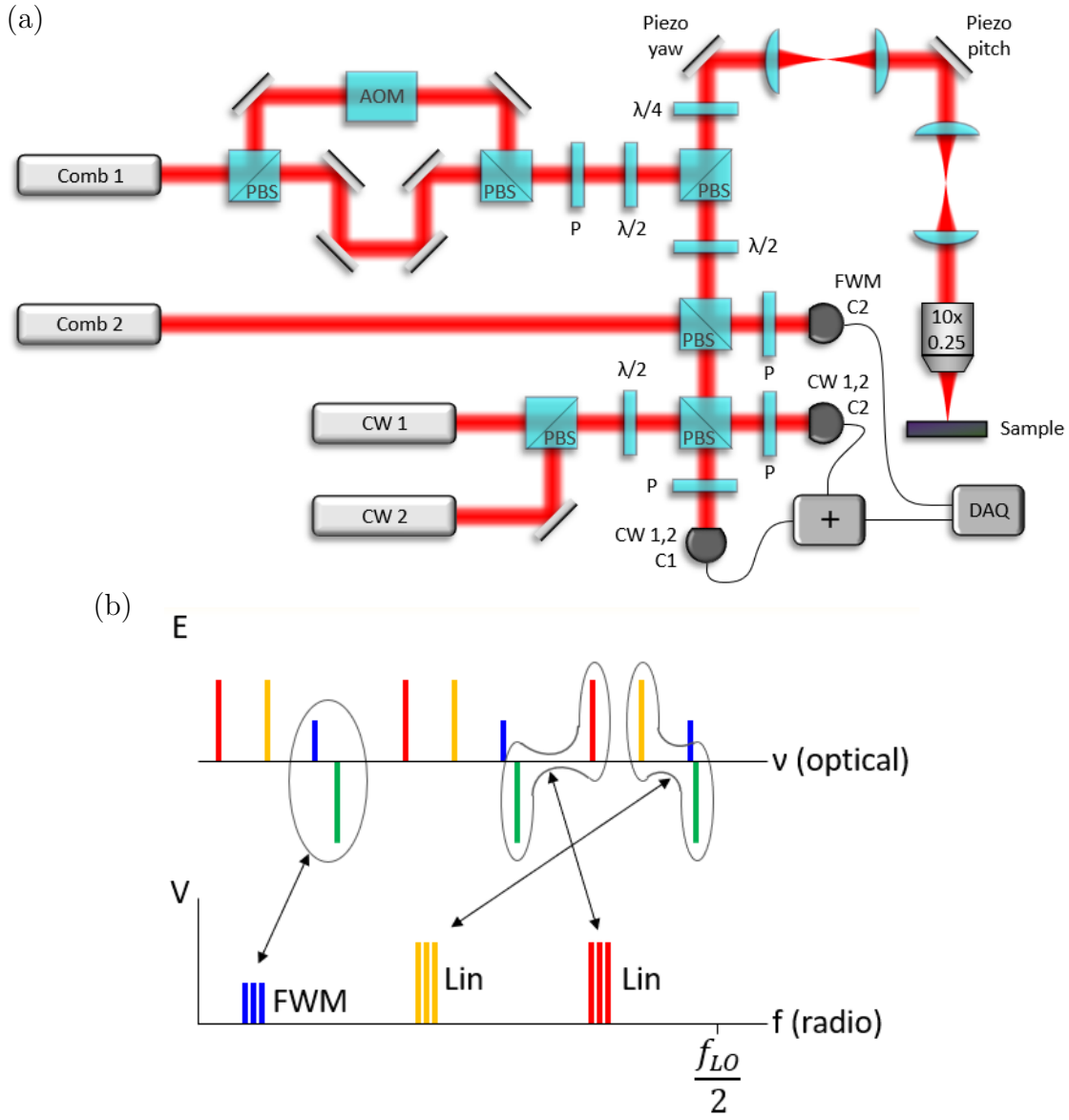

Figure 5.3: (a) Simplified schematic representation of the FWM hyperspectral microscopy experiment. P = polarizer, $\lambda/4$ = QWP, and $\lambda/2$ = HWP. (b) Mapping of optical comb teeth (red - comb 1, yellow - AOM shifted comb 1, blue - relevant FWM comb, green - comb 2) beating onto detector rf spectrum. Not shown is a large "time-zero" beat-note at 13 MHz (93 MHz repetition rate subtract 80 MHz AOM frequency) corresponding to beating between the AOM-shifted and non-AOM-shifted pump comb lines.

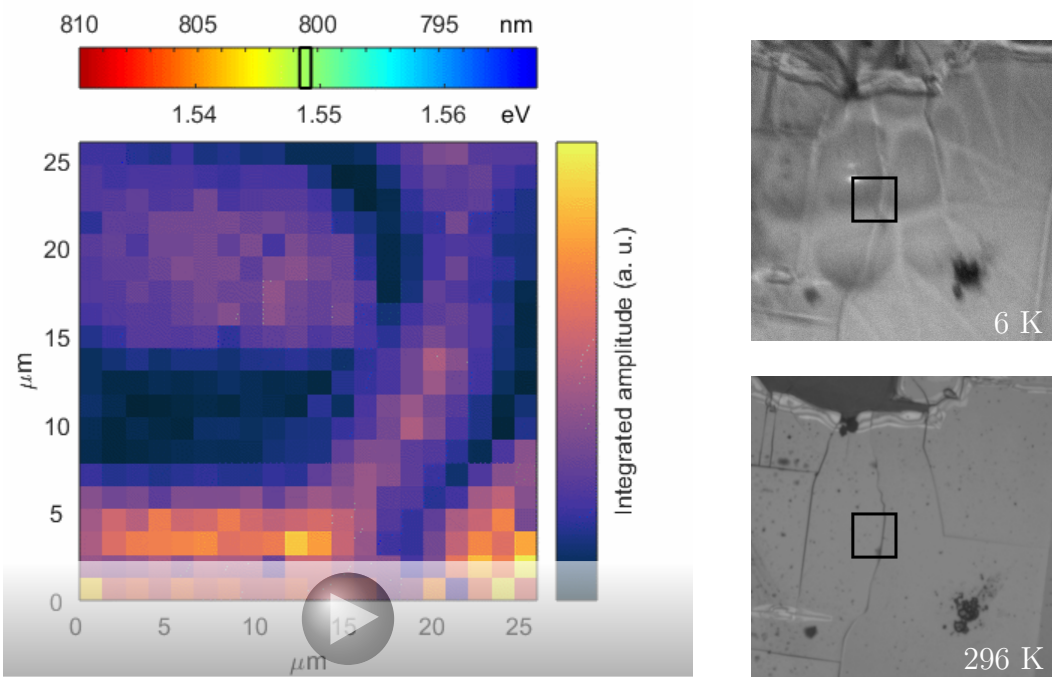

Figure 5.4: Left: initial hyperspectral image showing the spectrally integrated amplitude of the fully corrected FWM-LO heterodyne signal. Repetition rates and CW frequencies were slightly different than those described in text. 75 ms of data (6 bursts) were collected per pixel. Prior to integration, the spectrum was multiplied with a Gaussian whose FWHM is represented by the black box on the upper colorbar. Right: Corresponding white-light images during experiment (6 K - in high-vacuum cryostat) and eight months later at STP. The black square represents the hyperspectral scan area.

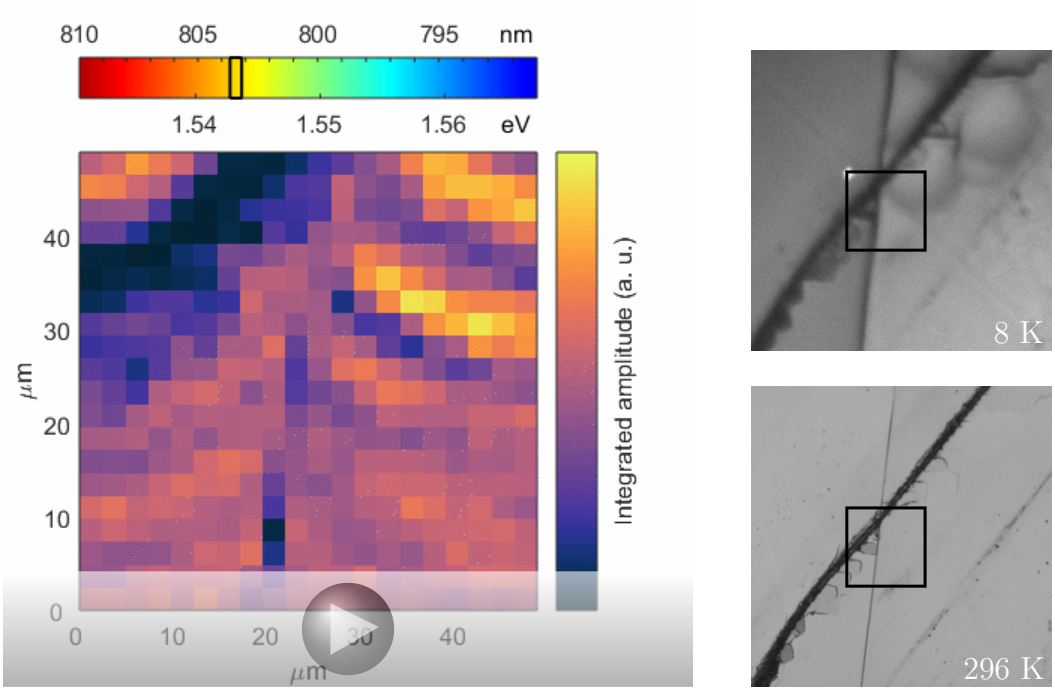

Figure 5.5: Left: hyperspectral image showing the spectrally integrated amplitude of the fully corrected FWM-LO heterodyne signal. 120 ms of data (8 bursts) were collected per pixel. Prior to integration, the spectrum was multiplied with a Gaussian whose FWHM is represented by the black box on the upper colorbar. Right: Corresponding white-light images during experiment (8 K - in high-vacuum cryostat) and eight months later (STP). The black square represents the hyperspectral scan area.

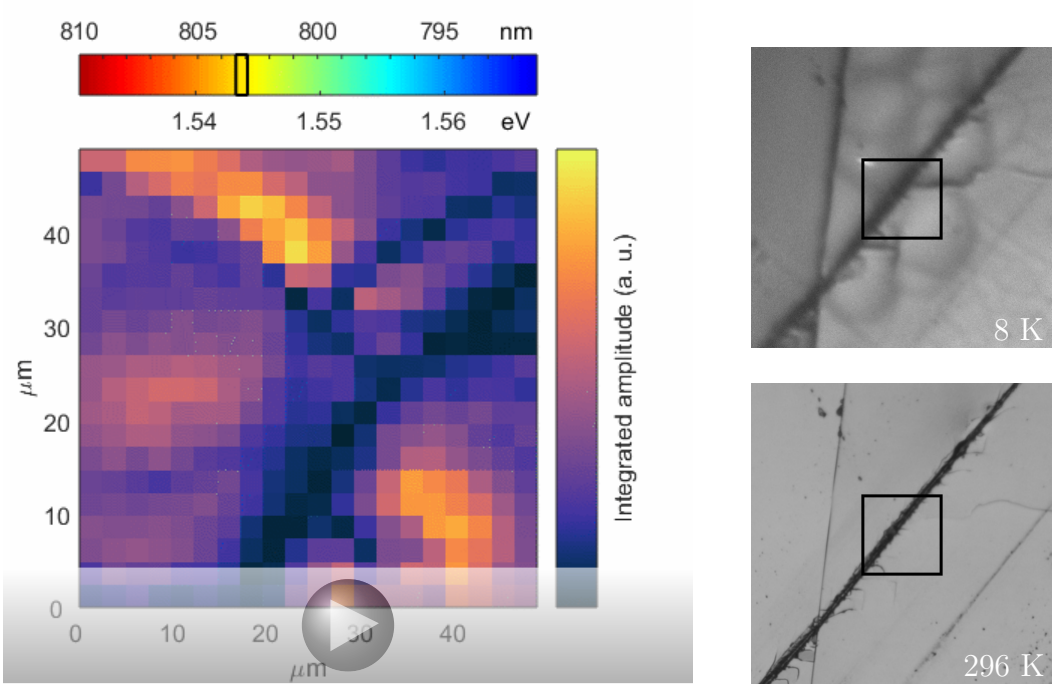

Figure 5.6: Left: hyperspectral image showing the spectrally integrated amplitude of the fully corrected FWM-LO heterodyne signal. Prior to integration, the spectrum was multiplied with a Gaussian whose FWHM is represented by the black box on the upper colorbar. Right: Corresponding white-light images during experiment (8 K - in high-vacuum cryostat) and eight months later (STP). The black square represents the hyperspectral scan area.

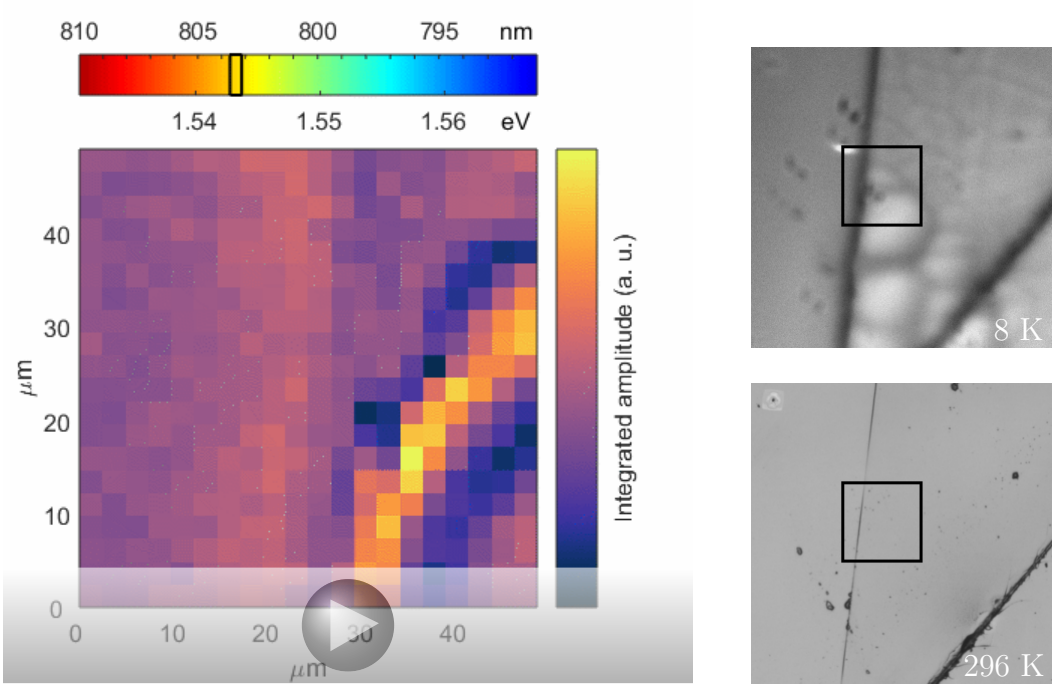

Figure 5.7: Left: hyperspectral image showing the spectrally integrated amplitude of the fully corrected FWM-LO heterodyne signal. Prior to integration, the spectrum was multiplied with a Gaussian whose FWHM is represented by the black box on the upper colorbar. Right: Corresponding white-light images during experiment (8 K - in high-vacuum cryostat) and eight months later (STP). The black square represents the hyperspectral scan area.

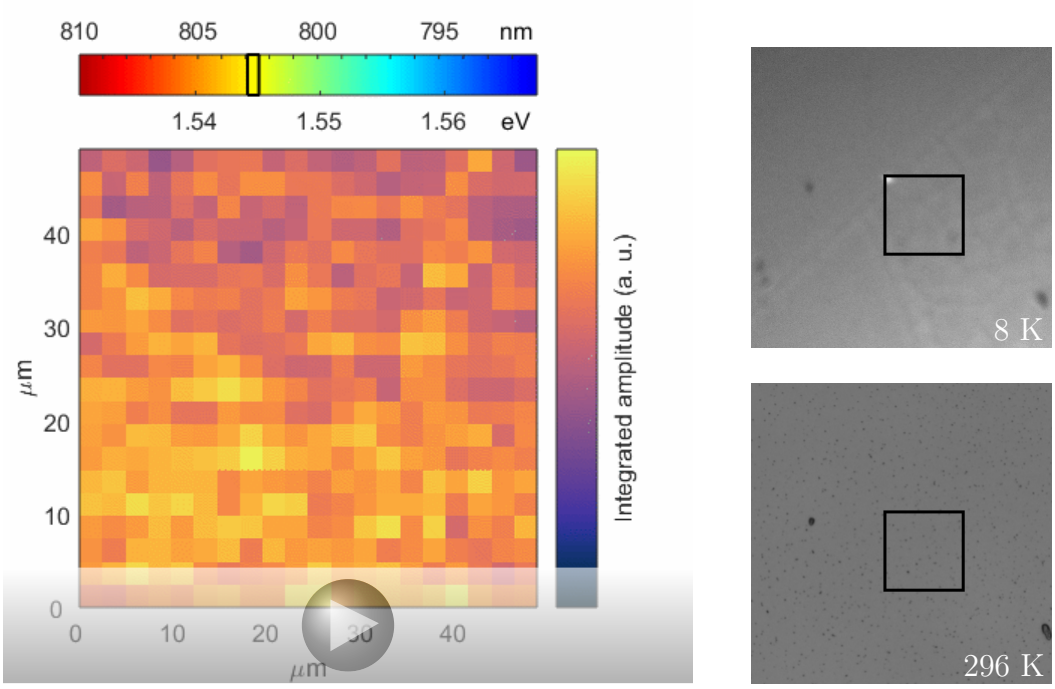

Figure 5.8: Left: hyperspectral image showing the spectrally integrated amplitude of the fully corrected FWM-LO heterodyne signal. Prior to integration, the spectrum was multiplied with a Gaussian whose FWHM is represented by the black box on the upper colorbar. Right: Corresponding white-light images during experiment (8 K - in high-vacuum cryostat) and eight months later (STP). The black square represents the hyperspectral scan area.

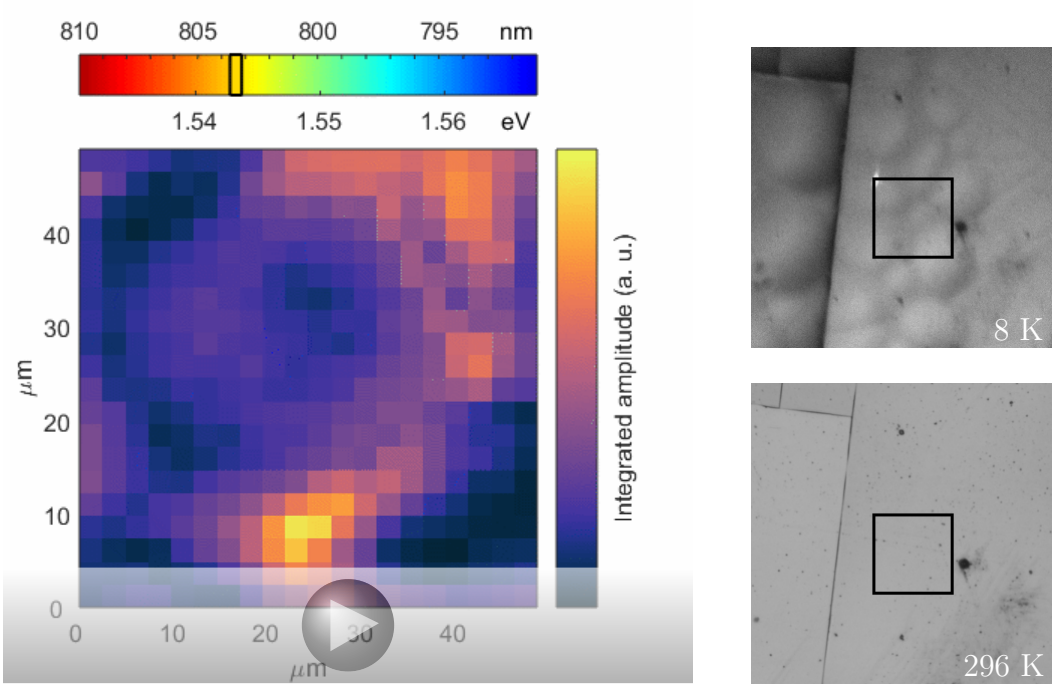

Figure 5.9: Left: hyperspectral image showing the spectrally integrated amplitude of the fully corrected FWM-LO heterodyne signal. Prior to integration, the spectrum was multiplied with a Gaussian whose FWHM is represented by the black box on the upper colorbar. Right: Corresponding white-light images during experiment (8 K - in high-vacuum cryostat) and eight months later (STP). The black square represents the hyperspectral scan area.

CHAPTER VI

Tri-comb spectroscopy

Compared to linear hyperspectral imaging, the technique presented in Chap. V offers increased spatial resolution and can in principle measure oscillator strengths and the density of states by comparing linear and nonlinear spectra [99]. However, it cannot distinguish between homogeneous and inhomogeneous broadening, determine whether or not certain energy levels are coupled, nor isolate signals from different species within a mixture. These benefits can be obtained by spectrally resolving $\boldsymbol{\chi}^{(3)}$ which requires a nonlinear extension of FTS known as MDCS (see Appx. E and Refs. [100, 101]).

In a typical MDCS experiment a series of three pulses pump the sample to generate a FWM signal. Using the analogy presented in the Chap. I, the pump pulses create a nonlinear polarization "tail" in the sample (see Fig. 1.3). When optical heterodyne detection is employed, a fourth pulse heterodynes with the nonlinear, radiated signal on a photodetector. As explained in Appx. E, the third-order response function can be extracted from the calculated third-order polarization density by scanning the time delays between all of the pulses and measuring the signal in a coherent (phase preserving) manner. In many circumstances it is only necessary to scan one of the inter-pump-pulse time delays and leave the other one fixed. In this case a projection of $\boldsymbol{\chi}^{(3)}$ onto some plane weighted by the pump field spectra is obtainable.

There are many existing techniques which can perform this type of measurement as shown in Fig. 6.1 [61,88,102–111]. Many of them employ mechanical delay stages - those that do not, typically have lower spectral resolution. Since MDCS is essentially "non-linear" FTS and can be accomplished using delay stages, one might wonder if replacing those stages with frequency combs would lead to a similar spectroscopic revolution as when dual frequency combs replaced the delay stage in FTIR (see discussion in Chap. III). This chapter details an experimental approach that accomplishes exactly this. Since it requires three combs and parallels DCS, the technique is coined TCS.

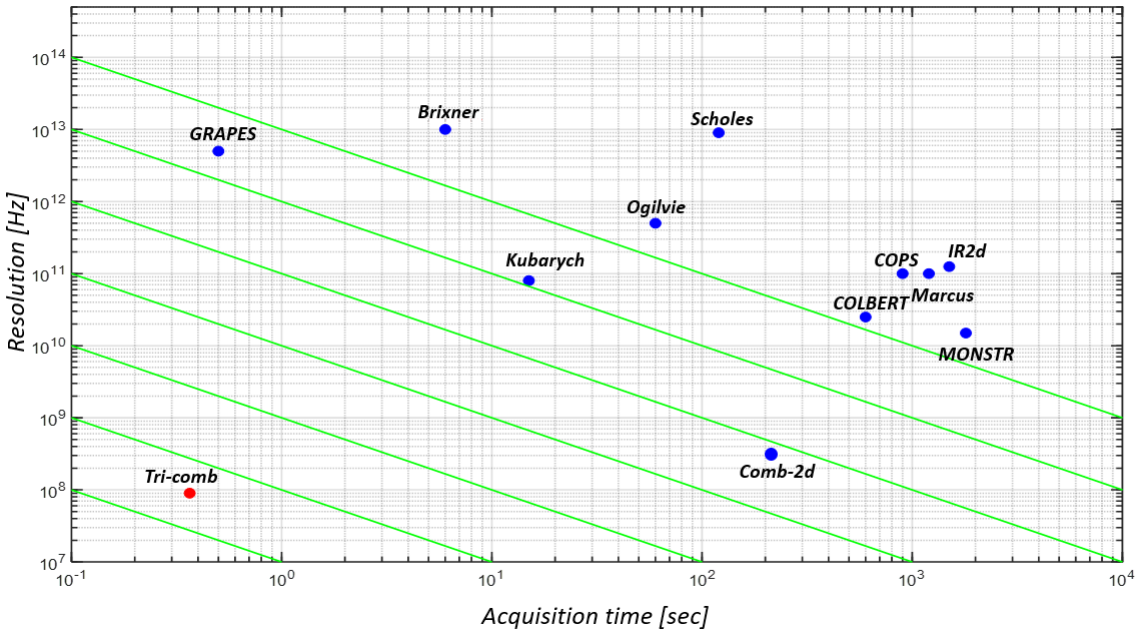

Figure 6.1: Spectral resolution vs. acquisition time for various MDCS techniques [61, 88, 102–111]. A figure of merit for any MDCS demonstration can be defined as the product of the resolution and the acquisition time. Green lines indicate constant figures of merit.

Just like Chap. V, the fundamental challenge in this work lies in isolating the FWM signal from all other signals (e.g. linear signals). For example, the box geometry can be employed [107] but this has limited microscopy applications because it prohibits a diffraction-limited spot size. Another technique called frequency tagging

involves modulating all the pump pulses (which have the same repetition rate) at different frequencies which leads to a FWM signal that is modulated at some linear combination of the pump modulation frequencies [88]. This enables lock-in detection to be employed to detect only the FWM signal however delay stages are required since the repetition rates are all the same. From a comb perspective, this is equivalent to using several combs with the same repetition rate but different offset frequencies and no modulators (as shown in Chap. V AOMs shift the offset frequency of a comb). To eliminate the need for delay stages and assuming T is fixed (the delay between the second and third pump pulses - see Fig. E.1), one could then choose three combs with slightly different repetition rates (leading to TCS) or electronically delay the pulses of three identical repetition rate combs for example by changing the phase of the reference signal that the combs are locked to (leading to DTCS - see Chap. VII). In this chapter, the former approach is taken. Note that simultaneously scanning T would require a fourth comb – quad-comb spectroscopy. Perhaps an ambitious future student will pursue this technique.

6.1 Experimental design

For an inhomogeneously broadened sample, a $\mathbf{S}_{\mathrm{I}}$-rephasing sequence of pulses will generate a photon echo (see Appx. E) with a τ vs t dependence cartooned in Fig. E.3(a) (sometimes referred to as a "time-time" plot). In order to perform the 2-dimensional Fourier transform necessary for creating a "2D" plot, the phase and amplitude of the photon echo must be measured at a sufficient number of points on the time-time plot. Choosing specific repetition rates for the three combs (mentioned in the previous paragraph) amounts to choosing some trajectory through t-τ space. Several trajectory options are shown in Fig. 6.2. In the following paragraph some experimental details that pertain to all trajectories will be discussed. After that, details for specific trajectories will be laid out.

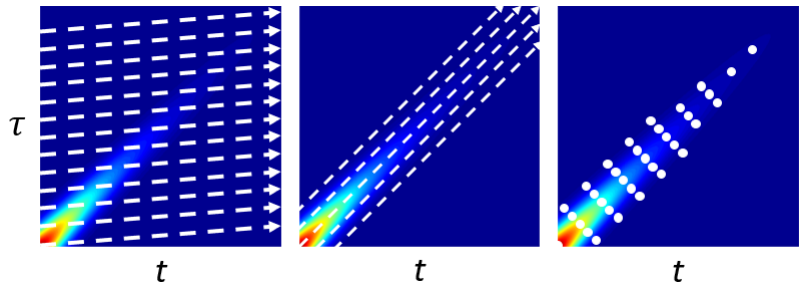

Figure 6.2: Tri-comb trajectories along photon echo time-time plots. (a) First attempt at TCS: $f_{\mathrm{A}} = f_{\mathrm{BC}} + \epsilon/n$ and $f_{\mathrm{LO}} = f_{\mathrm{BC}} - \epsilon$ where n is an integer. (b) "Echo-scan" used in TCS [105]: $f_{\mathrm{A}} = f_{\mathrm{BC}} + \epsilon$ and $f_{\mathrm{LO}} = f_{\mathrm{BC}} - \epsilon$. Parallel trajectories are obtained by phase shifting the reference repetition rate locking signal of LO comb. (c) Most efficient sampling proposed for future work described in Chap. VII: $f_{\mathrm{A}} = f_{\mathrm{BC}} = f_{\mathrm{LO}}$. Different data points are sampled by phase shifting the reference locking signals of the necessary combs. Photon echo illustration courtesy of Bachana Lomsadze.

In this work $T = 0$ which allows the actions of pulses B and C to originate from the same physical pulse. This reduces experimental complexity and allows the use of the two-pulse pump sequence depicted in Fig. 6.3. The experimental schematic is presented in Fig. 6.4. Beams from two separate combs are combined on a PBS. For alignment, CCDs were used (see Chap. V for details). These beams are now co-propagating, but orthogonally polarized. The beams were then filtered using a 3 nm optical band-pass filter centered on the D1 lines of Rubidium. This prevents unwanted excitation of other non-D1 Rb energy levels. The beams are focused using an approximately 3 cm positive lens into a 100 μm thick Rubidium vapor cell (natural abundance mixture of ^{85}Rb and ^{87}Rb isotopes) heated to approximately 100°C to generate a FWM signal. The FWM comb is non-trivial (see Fig. 6.4(b)) and looks like a comb of mini-combs. Interestingly, its FSR is ϵ (tiny!) but its repetition rate is $f_{\mathrm{FWM}} = f_{\mathrm{LO}} = f_{\mathrm{BC}} - \epsilon$ (not a true repetition rate because each successive pulse is smaller due to homogeneous decay – the true repetition rate is actually ϵ). The temperature of the cell was controlled using a resistive heater driven by a Variac 120 V outlet-powered transformer and measured using a thermocouple.

As a result of selection rules for the orthogonal pump polarization scheme used

here, the FWM signal will have the same polarization as pulse A. This is referred to as an HVVH scheme because pulse A (from comb 1) is horizontally polarized, pulses B and C (from a single comb 2 pulse) are vertically polarized, and the FWM is horizontally polarized. The FWM signal was re-collimated using another approximately 3 cm positive lens and combined with comb 3 on a PBS (again CCDs were used for alignment). One of the exit beams was sent through another 3 nm optical band-pass filter centered on the D1 lines of Rubidium to enable faster acquisition speeds by allowing greater differences in the repetition rates to be used before rf signal overlap occurs. This beam was then polarized at 45° and the heterodyne beat notes were photodetected. The other exit beam was used to measure repetition rate and offset frequency fluctuations via the same technique described in Chap. V. However, only one CW laser was needed for this experiment because the repetition rate fluctuations were sufficiently small such that the FWM comb could be locally resolved well enough using offset corrections alone as long as the frequency of the CW laser was sufficiently close the Rb D1 lines (in this experiment it was about 10 GHz away). Otherwise the technique is identical to that in Chap. V. The photodetected signals were also electrically filtered, amplified, and digitized following the same procedure in Chap. V. To perform the 2D Fourier transform, the t and τ values for all data points must be known. These values can be measured from the three linear dual-comb signals that were also recorded simultaneously. For example, when $\tau = 0$, the interferogram between combs 1 and 2 is at a maximum.

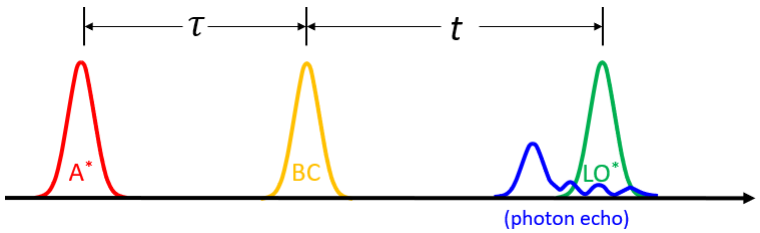

Figure 6.3: Pulse sequence for TCS.

Our first attempt at TCS followed the trajectory in Fig. 6.2(a) by choosing

$f_A = f_{BC} + \epsilon/n$ and $f_{LO} = f_{BC} - \epsilon$ where n is an integer. The requirement for n to be an integer ensures that the trajectory will repeat itself indefinitely. In principle this approach could work and would yield full comb resolution in the 2D-plot, but it had several practical limitations. In order to avoid rf signal overlap, ϵ had to be less than about 300 Hz. In order to sufficiently resolve the inhomogeneity, n had to be at least a couple hundred. This comes by comparing the inhomogeneous linewidth (hundreds of MHz due primarily to Doppler broadening) to the repetition rate of the combs (93.5 MHz) or equivalently the inhomogeneous decay time to the pulse period. This implies that the trajectory only samples the photon echo maximum about every second. This makes optimizing the signal during the experiment a painstaking endeavor. Furthermore, in order to acquire enough interferograms to achieve a reasonable SNR via averaging meant recording multiple seconds worth of data. At 100 MS/s with a 16-bit resolution this leads to enormous data files that are computationally difficult to process (and frequently crash Matlab!). This could potentially be remedied by employing some real-time processing techniques [91, 92]. Fortunately though, these difficulties drove the inspiration behind the TCS trajectory shown in Fig. 6.2(b).

We realized that the difficulties in the first trajectory all stemmed from sampling the large amount of "dead-time" where the photon echo is highly decayed. This lead us to explore trajectories that minimized the dead-time. The intrinsic diagonal structure of the photon echo suggested that diagonally scanning ($n = 1$) would minimize dead-time. But this would only sample a single line through t-τ space – it would require some other means of delaying τ and/or t to sample other diagonal lines. Bachana Lomsadze posited shifting the phase of the reference signal used for repetition rate locking (see Appx. C) for one of the combs to achieve this thereby providing an all-electronic means of controlling pulse delay. The direct digital synthesizer (DDS) controlling that locking signal has a 14-bit programmable phase which corresponds

to a minimum pulse delay change of 235 fs (since 360° corresponds to a full repetition period). This limits the optical bandwidth to about 2.13 THz (about 9 meV or 4.5 nm near 800 nm) before rf spectral overlap occurs. This is insufficient for many solid-state or liquid materials, but for atomic Rb it is more than enough.

Scanning the main diagonal ($\tau = t$) results in a signal that samples the photon echo maximum much more frequently (274 times per second as opposed to once per second) making signal optimization much easier. Moreover, because the data is now acquired in small chunks it is much easier and faster to process. This approach also automatically achieves full comb resolution along the homogeneous direction (cross-diagonal on 2D-plot) and allows user choice for resolution and bandwidth along the inhomogeneous direction (diagonal on 2D-plot) – see Fig. E.3(b). For the Rb sample, we collected 101 diagonal scans (with 100 bursts each using $\epsilon = 274$ Hz) with a *horizontal* spacing of 20 ps by incrementing the LO comb locking reference phase in steps of 0.6732°. Again, just as in Chap. V, the large size of the data files that needed to be saved meant the experiment took about 10 minutes of laboratory time to perform even though only 40 s worth of data were collected.

6.2 Results

The tri-comb spectra are shown in Fig. 6.5. In Fig. 6.5(a) the total data record is truncated such that only one burst per diagonal scan remains (365 ms of total data). This was done to highlight the potential for TCS to enable the rapid acquisition of MDCS data. Again, the data was acquired over a period much longer than 365 ms in the lab but this was circumstantial and not fundamental to the technique. In Fig. 6.5(b) the total data record is truncated such that only five bursts per diagonal scan remain (about 2 s of total data). Fig. 6.5(c) corresponds to the entire 40 s of data collected (100 bursts per diagonal scan).

6.3 Discussion

Compared to other MDCS techniques, TCS is either orders of magnitude faster or has a spectral resolution orders of magnitude greater or both depending on which other technique it is compared to (see Fig. 6.1). While the use of three combs may seem overly complicated, it is worth noting that the ease of use, compactness, and power requirements of combs (particularly microresonators) are rapidly improving. Recently, three combs with different repetition rates were generated from a single microresonator [112] and from a single fiber laser [113]. Furthermore, both DCS and ultrafast ranging have been proven to receive benefits when three combs are used. For both applications, the ambiguity regions are removed leading to absolute ranging [114] and absolute dead-band-free triple DCS [115]. As mentioned earlier the implementation of TCS used here actually simultaneously acquires three dual-comb spectra for (t, τ) determination which could also be used for this latter application if desired.

While the results of TCS are indeed impressive, the technique does suffer several limitations. First, even if the DDS had better phase resolution, the maximum optical bandwidth usable for TCS is even stricter than DCS because both linear and FWM signals much be digitized. Unlike DCS though, this requirement cannot be eased through the use of higher repetition rates because that lowers the SNR [16]. Second, full diagonal scans are always acquired regardless of the photon echo decay parameters (see Fig. 6.2). This means for short lived samples that dead-time could be significantly lowering the SNR. Third, the calculation of (t, τ) points from the linear dual-comb data is not very precise. This makes little difference for long-lived samples like Rb, but could destroy MDCS plots for shorter lived samples. These limitations are addressed in the following chapter.

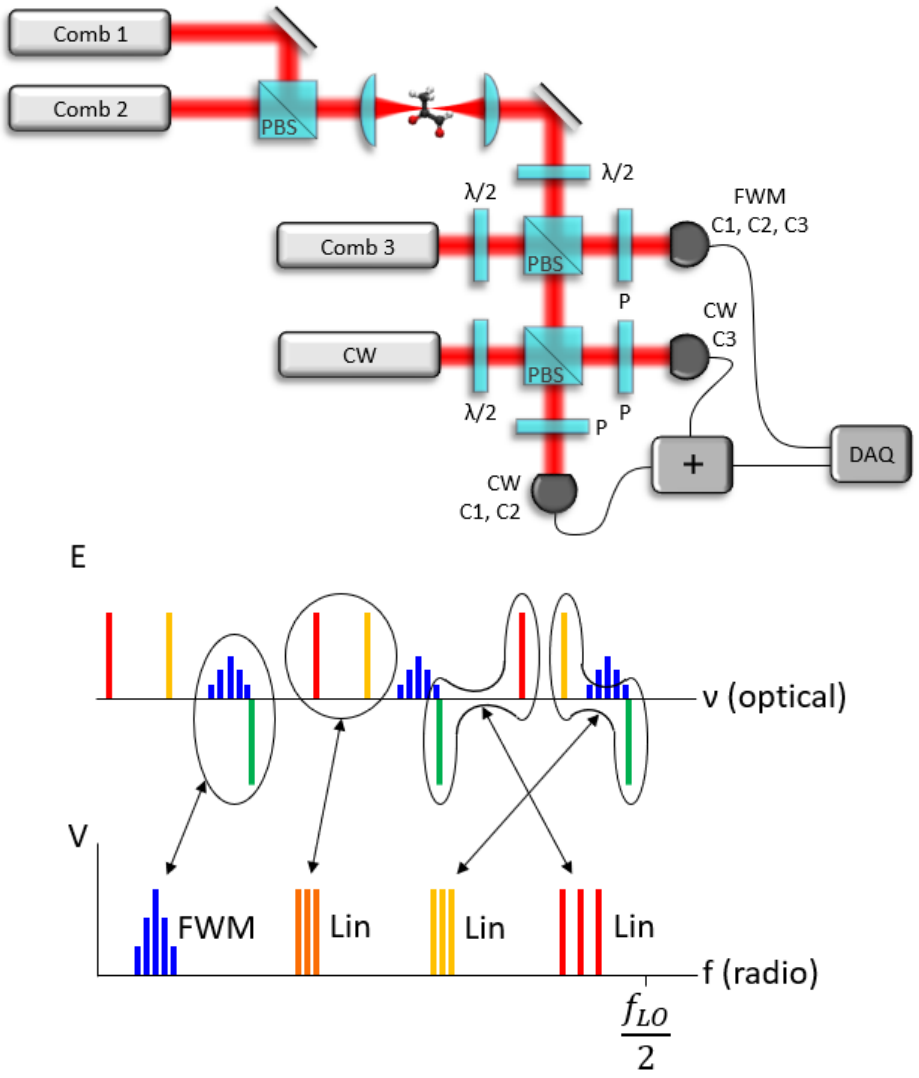

Figure 6.4: (a) Simplified experimental schematic for TCS. P = polarizer and $\lambda/2$ = HWP. (b) Mapping of optical comb teeth (red - comb 1, yellow - comb 2, blue - relevant FWM comb, green - comb 3) beating onto detector rf spectrum. Note the FSR of the FWM comb is ϵ but its quasi repetition rate is $f_{\mathrm{FWM}} = f_{\mathrm{LO}} = f_{\mathrm{BC}} - \epsilon$ (see text).

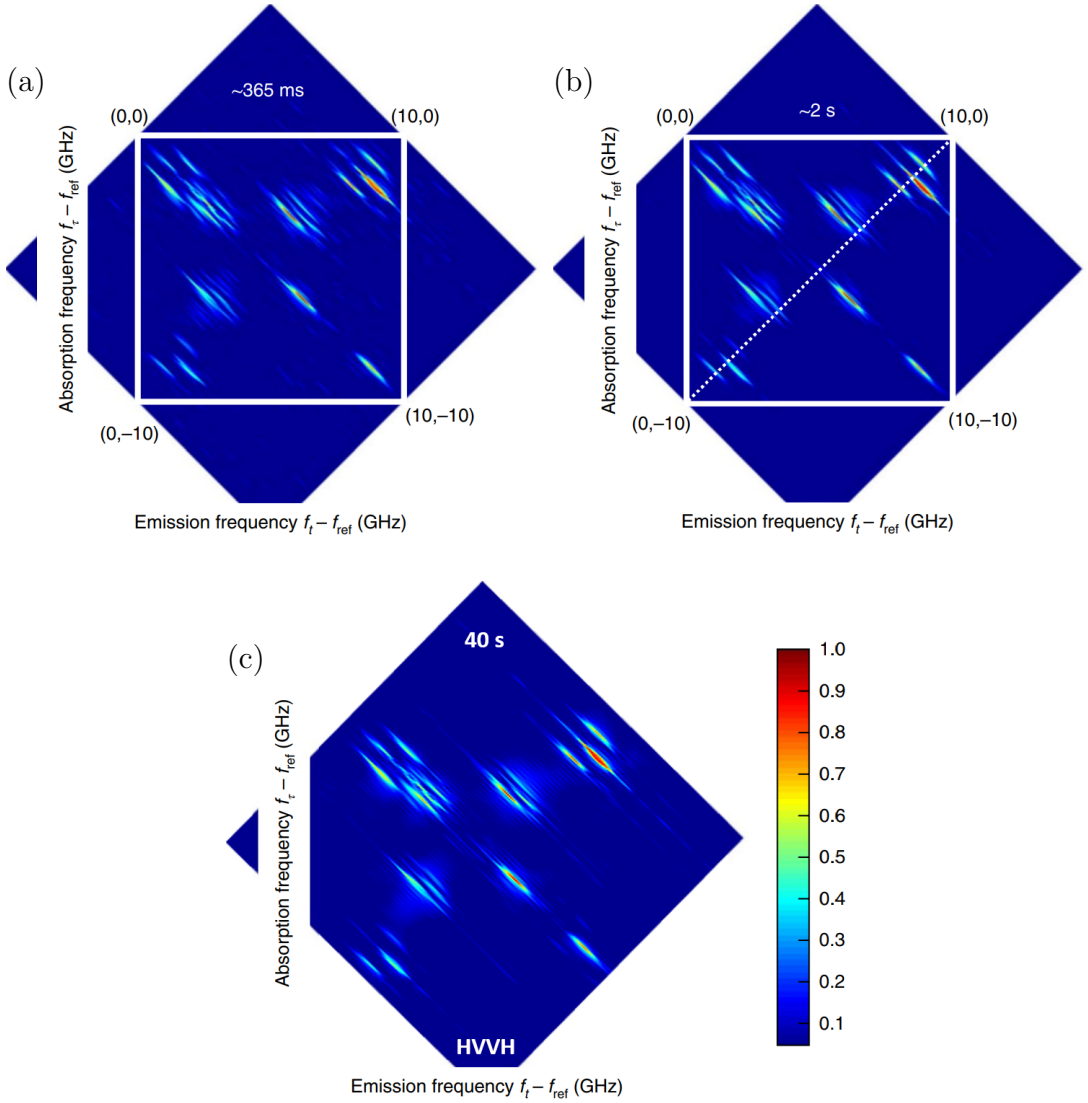

Figure 6.5: Tri-comb spectrum of D1 lines of ^{85}Rb and ^{87}Rb. (a) 365 ms worth of total data (1 burst per diagonal scan). (b) 2 s worth of total data (5 bursts per diagonal scan). (c) entire 40 s data record (100 bursts per diagonal scan). All plots are separately normalized.

CHAPTER VII

Outlook

The realization of the frequency comb caused a paradigm shift in spectroscopy leading to the development of a plethora of comb sources that have provided unprecedented accuracy, precision, and speed for a host of applications (see Chap. II). The rate of development of both sources and applications has been truly remarkable. Just this year (2018), a self-referenced, ultrafast, optical comb with few-cycle pulses was carved directly from CW light using an electro-optic modulation approach [116], the first battery-powered comb was fashioned by photonically integrating a microresonator and its pump onto a single chip [69], and significant steps towards a chip-scale atomic clock were made by photonically integrating several key optical atomic clock components [117]. This dissertation provides novel contributions within the realm of comb-based spectroscopy that aim to maintain the rapid progress of frequency comb technologies.

In Chap. III the practical question, "what comb characteristics are optimal for a given DCS application?" was addressed initially in terms of the repetition rates and later generalized to the achievable SNR and spectral point spacing. The latter dissection has applications beyond spectroscopy – it could benefit any kind of peak fitting analysis. In Chap. IV a novel comb source – the phase-locked laser diode – was characterized and used to demonstrate DCS and battery-powered operation.

The results suggest laser diodes could one day give rise to smart-phone-sized dual-comb spectrometers. In Chap. V a high-precision, potentially high-speed, nonlinear hyperspectral microscopy technique was developed. As comb sources become more compact and robust, it could perhaps be commercialized into a device that attaches to standard microscopes. Lastly, the $\boldsymbol{\chi}^{(3)}$-resolving, triple-comb technique (TCS) developed in Chap. VI smashed the resolution record for MDCS while simultaneously having the (potentially) fastest acquisition time.

Using two combs with different repetition rates to detect and read-out either a linear (e.g. DCS) or nonlinear (e.g. TCS) signal can offer incredible spectral resolutions by measuring coherences temporally overall the entire pulse repetition period. But is this much resolution really needed? Chap. III addressed closely related questions for DCS – it was found that increasing the resolution by decreasing the signal comb repetition rate ends up decreasing the SNR and that these effects, roughly speaking, cancel out assuming all else is equal. But as Chap. I pointed out, lower repetition rates generally increase the SNR for nonlinear measurements [16]. However, they also impose stricter limits on the allowable optical bandwidth before rf spectral overlap occurs. Thus, tighter locking is required. Chaps. I and VI addressed this and other limitations by considering the use of combs with the *same* repetition rate and delaying their pulses by some electronic means. This offers four main advantages. First, there is no longer a limit on the optical bandwidth that can be used. Second, the SNR and acquisition time can be improved by choosing to only sample meaningful, high SNR points (dead-time is avoided). Third, multiple quantum pathways can be measured simultaneously as mentioned in Appx. E including both linear and nonlinear. Fourth, the resolution is no longer determined by the comb FSR, but by the user. The remainder of this chapter explores the degenerate repetition rate approach in more detail as a teaser for future dual-comb (linear) and tri-comb (nonlinear) experiments.

Both linear and nonlinear FTS-based techniques rely on knowing the relative op-

tical phase and delay between pulses. Hence, data must be phase-coherently recorded as a function of the delay(s) in order for Fourier transforms to be used. The relative optical phase (and its noise) can be completely addressed using the one-CW approach described in Appx. D. This is can be observed in normal DCS where it removes the offset frequency and locks the carrier of the rf comb to its envelope. There is no reason to believe the same technique would fail when the repetition rates are nearly the same. So, all that remains is determining the pulse delay timing and its fluctuations. When a DDS can be used to control the pulse delays (see Chap. VI), it's phase value linearly correlates to an expected pulse delay (there could still be noise). This worked well for the long-lived atomic sample and free-running combs in Ref. [105] because the delays did not need to be known with high precision for accurate results to be obtained. But for broadband samples, the DDS phase resolution is insufficient and problematic aliasing would occur (see Chap. VI). To address this, the repetition rates can be modulated or the noise in the comb repetition rates can be leveraged to increase the bandwidth by sampling more closely spaced points.

No matter the mechanism, the delay between successive pulses must be tracked. Using two CW reference lasers, m comb modes apart from each other, one can create a clock which tracks m times the difference in repetition rates (and thus m times the pulse delay) between two combs:

$$C(t) \propto e^{2m\pi i \Delta f_{\mathrm{rep}}\, t} \; . \tag{7.1}$$

This is accomplished by mixing all four beat notes with each other. By unwrapping the phase of this clock (which technically shouldn't really need to be unwrapped if $\Delta f_{\mathrm{rep}} \approx 0$) one calculates:

$$\phi(t) \equiv 2m\pi \Delta f_{\mathrm{rep}}\, t \; . \tag{7.2}$$

We know that if ϕ changes by $2m\pi$ then the LO pulse has slipped $1/f_{\text{rep}}$ away in time relative to a signal pulse. Thus, the pulse delay $\tau(t)$ is related to ϕ by:

$$\tau(t) = \frac{\phi(t)}{2m\pi f_{\text{rep}}} + \tau(0) \; . \tag{7.3}$$

The precision in calculating τ (and therefore the maximum allowable optical bandwidth) is directly related to the precision in measuring ϕ. Clearly, large m values lead to greater precision for τ. For example, a phase precision of 10 degrees with $f_{\text{rep}} \approx 100$ MHz gives a τ precision of 280 ps for $m = 1$ (could use a single CW laser and monitor the nearest comb teeth on both sides) and 0.6 fs for $m = 470000$ (CW laser center frequencies at 750 nm and 850 nm). Roughly speaking the distance between the CW laser center frequencies is on the same order of magnitude as the maximum allowable optical comb bandwidth. $\tau(0)$ corresponds to the beginning pulse delay which can be calculated from the corrected data by using the fact that the maximum interferogram amplitude occurs at zero pulse delay. An incorrect $\tau(0)$ leads to a phase ramp in the calculated spectrum. Eq. (7.3) provides a map between lab time and pulse delay. Thus, randomly sampled data points can be reorganized to create the interferogram. Since the space between these τ points is non-uniform, the spectral information can be recovered either by resampling to a uniform spacing followed by an fast Fourier transform (FFT) or directly by using a non-uniform fast Fourier transform (NUFFT) as discussed in Appx. D. The only difference between this approach and conventional DCS is that in the latter many consecutive interferograms are recovered where here only a fraction of one is sampled. For this reason, one possible name for this approach is sub-interferogram comb (SIC) spectroscopy. The names degenerate DCS and degenerate TCS were suggested earlier as well. Experiments to verify this degenerate-repetition rate technique for both linear and nonlinear measurements are already underway.

The flexibility enabled by degenerate repetition rate techniques (user controlled bandwidth, resolution, quantum pathway, etc.) combined with its potentially increased SNR and acquisition speed make it a unique and interesting way to use combs. If the advent of frequency combs represented a shift in thinking towards the frequency domain, then degenerate repetition rate techniques may constitute a step towards a dual, time-frequency approach. This is because the periodicity of combs is used to generate a non-periodic interferogram. This allows utilization of the optical comb teeth to track the relative pulse delay while maintaining highly efficient sampling of the interferogram. It remains to be seen whether this shift proves useful. Thank you and congratulations for making it to the end of my dissertation! I hope you found it useful.

APPENDICES

APPENDIX A

Nonlinearity in the Lorentz oscillator model

The Lorentz oscillator model (LOM) has been a staple in optics for over 100 years [118]. It's original formulation played a major role in the acceptance of the electron due to its explanation of the Zeeman effect [119–122]. The calculated electron charge to mass ratio agreed with J. J. Thomson's experiment the following year which further confirmed the particle's existence [123, 124]. Today, the LOM is useful for gaining an intuitive understanding of the physical interaction between light and matter and is frequently seen in an educational context. When only the electric term is retained in the Lorentz force and its spatial dependence ignored (electric dipole approximation) the LOM captures a surprising number of features (dispersion, absorption, etc.) for such a simple model. The expression obtained for the atomic polarizability even has the same structure as one obtained via quantum mechanics and also satisfies Kramers-Kronig relations [125].

Although Lorentz retained the magnetic force from an applied static magnetic field, the force from the optical magnetic field was still neglected [119]. In modern textbooks it is argued that since the magnetic force from a plane wave is about v/c (where v is a particle's speed and c is the speed of light) times smaller in magnitude than the corresponding electric force it may be neglected for driving fields of

non-relativistic strength [126]. However, this overlooks the fact that these forces are usually orthogonal and occur at different frequencies. So, while it may be small, the optical magnetic force is sometimes the only force that drives motion in a particular direction or at a particular frequency. Because of this the contributions of the magnetic force can be significant even for low intensities of light. For example, the optical magnetic force is responsible for the transfer of light's momentum to matter and leads to the photon drag effect (discussed in Sec. A.4.3.1).

Several works have included the optical magnetic force but only considered special cases within the electric dipole approximation: in Ref. [127] the electric and magnetic fields are restricted to be monochromatic and non-static while Ref. [128] cannot support a static magnetic field. In this work the full magnetic force is retained in addition to anharmonic restoring forces and perturbation solutions are obtained beyond the electric dipole approximation. These solutions qualitatively and quantitatively (within an order of magnitude) describe magneto-optic effects (the normal, linear Zeeman, Faraday, and surface magneto-optic Kerr effects), electro-optic effects (the linear Stark, Pockels, and Kerr effects), the momentum and angular momentum of a photon in matter (contributing to the Abraham-Minkowski debate), and other three-wave mixing processes allowed in centrosymmetric media (the photon drag and inverse Faraday effects and sum-frequency and second-harmonic generation). Although this extended version of the LOM may not capture the finer details found using semi-classical or fully quantized approaches, its simplicity makes it an ideal choice for building intuition, crude calculations, and qualitative study.

A.1 Equations of motion

A description of the LOM written by H. A. Lorentz can be found in Ref. [118]. It was known at the time that a charged particle oscillating at a certain frequency would radiate light having that same frequency. From this, Lorentz conjectured

that the spectral lines in a material could be the result of harmonically bound pairs of oppositely charged particles with each spectral line corresponding to a different binding stiffness. A modern description which more closely follows this work can be found in Ref. [126]. The LOM consists of two point masses referred to here as the nucleus, with mass m_n and charge q, and electron, with mass m_e and charge $-q$ (see Fig. A.1). With no external forces, the equilibrium positions of each particle are assumed to be the same as the result of a conservative restoring force between the two particles. For small excursions from equilibrium a Taylor series expansion of the corresponding potential energy yields a Hooke's law type force as the leading term followed by anharmonic terms. Damping forces are inserted phenomenologically to account for energy loss (see Ref. [10] for a detailed discussion). Lastly, the electric and magnetic fields are coupled to each particle via the Lorentz force.

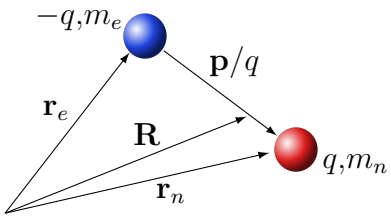

Figure A.1: Coordinates in the LOM.

A.1.1 Newton's second law

The equations of motion for the positions of the electron, $\mathbf{r}_e(t)$, and nucleus, $\mathbf{r}_n(t)$ are provided by Newton's second and third laws:

$$m_n \ddot{\mathbf{r}}_n = \mathbf{F}_{ln} + \mathbf{F}_{dn} + \mathbf{F}_r \tag{A.1}$$

$$m_e \ddot{\mathbf{r}}_e = \mathbf{F}_{le} + \mathbf{F}_{de} - \mathbf{F}_r \ . \tag{A.2}$$

The Lorentz forces are $\mathbf{F}_{ln} = q\,\mathbf{E}(\mathbf{r}_n) + q\,\dot{\mathbf{r}}_n \times \mathbf{B}(\mathbf{r}_n)$ and $\mathbf{F}_{le} = -q\,\mathbf{E}(\mathbf{r}_e) - q\,\dot{\mathbf{r}}_e \times \mathbf{B}(\mathbf{r}_e)$ where $\mathbf{E}$ and $\mathbf{B}$ are the local electric and magnetic fields respectively, the

phenomenological damping forces are $\mathbf{F}_{dn} = -m_n \boldsymbol{\gamma} \cdot \dot{\mathbf{r}}_n$ and $\mathbf{F}_{de} = -m_e \boldsymbol{\gamma} \cdot \dot{\mathbf{r}}_e$ where $\boldsymbol{\gamma}$ is a symmetric rank-two tensor, and the restoring force is $\mathbf{F}_r = -\mathbf{k}^{(1)} \cdot \mathbf{p}/q - \mathbf{k}^{(2)} : \mathbf{pp}/q^2 - \mathbf{k}^{(3)} \vdots \mathbf{ppp}/q^3 + \cdots$ where $\mathbf{p}$ is the electric dipole moment defined in Eq. (A.3) and $\mathbf{k}^{(1)}$, $\mathbf{k}^{(2)}$, and $\mathbf{k}^{(3)}$ are symmetric tensors of rank two, three, and four, describing the first-order (harmonic), second-order (anharmonic), and third-order (anharmonic) restoring forces respectively (see Ref. [8]).

It is convenient to express the equations of motion in the center of mass coordinate system defined by

$$\mathbf{R} \equiv \frac{m_e \mathbf{r}_e + m_n \mathbf{r}_n}{m_e + m_n} \qquad \text{and} \qquad \mathbf{p} \equiv q\,(\mathbf{r}_n - \mathbf{r}_e) \tag{A.3}$$

where $\mathbf{R}(t)$ is the position of the center of mass of the system and $\mathbf{p}(t)$ is the electric dipole moment (see Fig. A.1). Using this coordinate system and the explicit forms of the forces the equations of motion are

$$\begin{aligned} \ddot{\mathbf{R}} + \boldsymbol{\gamma} \cdot \dot{\mathbf{R}} = \frac{1}{M} \Bigg\{ & q \Big[\mathbf{E}(\mathbf{r}_n) - \mathbf{E}(\mathbf{r}_e) \Big] \\ & + q\, \dot{\mathbf{R}} \times \Big[\mathbf{B}(\mathbf{r}_n) - \mathbf{B}(\mathbf{r}_e) \Big] \\ & + \frac{\dot{\mathbf{p}}}{M} \times \Big[m_e\, \mathbf{B}(\mathbf{r}_n) + m_n\, \mathbf{B}(\mathbf{r}_e) \Big] \Bigg\} \end{aligned} \tag{A.4}$$

for the center of mass and

$$\begin{aligned} \ddot{\mathbf{p}} + \boldsymbol{\gamma} \cdot \dot{\mathbf{p}} + \frac{\mathbf{k}^{(1)}}{m} \cdot \mathbf{p} = \frac{q}{m} \Bigg\{ & qm \left[\frac{\mathbf{E}(\mathbf{r}_n)}{m_n} + \frac{\mathbf{E}(\mathbf{r}_e)}{m_e} \right] \\ & + qm\, \dot{\mathbf{R}} \times \left[\frac{\mathbf{B}(\mathbf{r}_n)}{m_n} + \frac{\mathbf{B}(\mathbf{r}_e)}{m_e} \right] \\ & + \frac{m\, \dot{\mathbf{p}}}{M} \times \left[\frac{m_e\, \mathbf{B}(\mathbf{r}_n)}{m_n} - \frac{m_n\, \mathbf{B}(\mathbf{r}_e)}{m_e} \right] \\ & - \frac{\mathbf{k}^{(2)}}{q^2} : \mathbf{pp} - \frac{\mathbf{k}^{(3)}}{q^3} \vdots \mathbf{ppp} \Bigg\} \end{aligned} \tag{A.5}$$

for the electric dipole moment where $M \equiv m_n + m_e$ and $m \equiv m_n m_e/M$ are the system's total and reduced mass respectively .

A.1.2 Taylor expansion

Eqs. (A.4) and (A.5) require knowledge of $\mathbf{E}$ and $\mathbf{B}$ at the positions of each particle for all time making it difficult to find solutions directly. As long as the maximum displacement of the particles from $\mathbf{R}$ is much less than the wavelength of the fields it is justifiable to expand the electric and magnetic fields in a Taylor series about the center of mass position $\mathbf{R}$ [126]. Retaining only the first term corresponds to making the usual electric dipole approximation. The following terms incorporate higher-order multipole moments. Each series will be truncated such that the equations of motion are valid to second-order in the perturbation expansion presented in Sec. A.2 (see Supplemental Material for higher-order expressions and a discussion of their usefulness). Thus, up to second-order the equations of motion become

$$\ddot{\mathbf{R}} + \boldsymbol{\gamma} \cdot \dot{\mathbf{R}} = \frac{1}{M}\Big[(\mathbf{p} \cdot \nabla)\, \mathbf{E} + \dot{\mathbf{p}} \times \mathbf{B} \Big] , \tag{A.6}$$

for the center of mass and

$$\begin{aligned} \ddot{\mathbf{p}} + \boldsymbol{\gamma} \cdot \dot{\mathbf{p}} + \frac{\mathbf{k}^{(1)}}{m} \cdot \mathbf{p} = \frac{q}{m}\Big[& q\, \mathbf{E} - \xi_2\, (\mathbf{p} \cdot \nabla)\, \mathbf{E} \\ & + q\, \dot{\mathbf{R}} \times \mathbf{B} - \xi_2\, \dot{\mathbf{p}} \times \mathbf{B} \\ & - \frac{\mathbf{k}^{(2)}}{q^2} : \mathbf{pp} \Big] , \end{aligned} \tag{A.7}$$

for the electric dipole moment where the gradients and all fields are evaluated at $\mathbf{R}$ and where we have defined the dimensionless factor $\xi_2 \equiv (m_n^2 - m_e^2)/M^2$ which ranges from -1 to 1. See Ref. [125] for a detailed discussion of the force terms in Eq. (A.6).

A.2 Perturbation expansion

Contrary to the typical linear response LOM these new equations of motion are nonlinear and have no known analytical solutions. For this reason a procedure similar to Rayleigh-Schrödinger perturbation theory can be used to obtain perturbation solutions [8]. For simplicity $\mathbf{v} \equiv \dot{\mathbf{R}}$ is the velocity of the atom. First, $\mathbf{v}$ and $\mathbf{p}$ are expanded in a power series of the perturbation parameter λ

$$\mathbf{v} = \mathbf{v}^{(0)} + \lambda\,\mathbf{v}^{(1)} + \lambda^2\,\mathbf{v}^{(2)} + \cdots \tag{A.8}$$

$$\mathbf{p} = \mathbf{p}^{(0)} + \lambda\,\mathbf{p}^{(1)} + \lambda^2\,\mathbf{p}^{(2)} + \cdots\ . \tag{A.9}$$

Note that $\mathbf{v}^{(0)}$ and $\mathbf{p}^{(0)}$ represent homogeneous solutions (which are ignored in this work) and all other terms represent particular solutions. Next, the driving fields are treated as perturbations by taking $\mathbf{E} \to \lambda\mathbf{E}$ and $\mathbf{B} \to \lambda\mathbf{B}$. Inserting these expressions into Eqs. (A.6) and (A.7) yields two equations in many powers of λ. When the coefficients of each power of λ are gathered and set equal to zero, two infinite series of simultaneous equations are produced. The first few equations of these series are

$$\dot{\mathbf{v}}^{(1)} + \boldsymbol{\gamma} \cdot \mathbf{v}^{(1)} = \mathbf{0}\,, \tag{A.10}$$

$$\dot{\mathbf{v}}^{(2)} + \boldsymbol{\gamma} \cdot \mathbf{v}^{(2)} = \frac{1}{M}\left[\left(\mathbf{p}^{(1)} \cdot \nabla\right)\mathbf{E} + \dot{\mathbf{p}}^{(1)} \times \mathbf{B}\right], \tag{A.11}$$

for the velocity and

$$\ddot{\mathbf{p}}^{(1)} + \boldsymbol{\gamma} \cdot \dot{\mathbf{p}}^{(1)} + \frac{\mathbf{k}^{(1)}}{m} \cdot \mathbf{p}^{(1)} = \frac{q^2}{m}\,\mathbf{E}\,, \tag{A.12}$$

$$\ddot{\mathbf{p}}^{(2)} + \boldsymbol{\gamma} \cdot \dot{\mathbf{p}}^{(2)} + \frac{\mathbf{k}^{(1)}}{m} \cdot \mathbf{p}^{(2)} = \frac{q}{m}\Big[q\, \mathbf{v}^{(1)} \times \mathbf{B} - \xi_2 \left(\mathbf{p}^{(1)} \cdot \nabla\right) \mathbf{E} - \xi_2\, \dot{\mathbf{p}}^{(1)} \times \mathbf{B} - \frac{\mathbf{k}^{(2)}}{q^2} : \mathbf{p}^{(1)}\mathbf{p}^{(1)} \Big] \,. \tag{A.13}$$

for the electric dipole moment.

Solutions to each equation can be obtained in the frequency domain using Fourier transforms of the form:

$$\mathbf{h}(t) = \int_{-\infty}^{\infty} \mathrm{d}\omega\; \tilde{\mathbf{h}}(\omega)\; e^{-i\omega t} \,. \tag{A.14}$$

For example, the solution to the traditional linear LOM (see Eq. (A.12)) is $\mathbf{p}^{(1)}(\omega) = \varepsilon_0\, \boldsymbol{\alpha}^{(1)}(\omega) \cdot \tilde{\mathbf{E}}(\omega)$ where the linear polarizability is $\boldsymbol{\alpha}^{(1)}(\omega) \equiv q^2/(m\varepsilon_0)[\mathbf{k}^{(1)}/m - \omega^2 \boldsymbol{\delta} - i\omega\boldsymbol{\gamma}]^{-1}$ and $\boldsymbol{\delta}$ is the unit dyadic.

A.2.1 Other multipole moments

Perturbation solutions can also be obtained for other multipole moments of the oscillator as well. For example, the magnetic dipole moment in the center of mass frame (which is the appropriate frame to use later for spatial averaging - see Ref. [7]) is:

$$\begin{aligned} \mathbf{m} &\equiv \frac{1}{2} \sum_{\alpha} q_\alpha (\mathbf{r}_\alpha - \mathbf{R}) \times (\dot{\mathbf{r}}_\alpha - \dot{\mathbf{R}}) \\ &= -\frac{\xi_2}{2q} \mathbf{p} \times \dot{\mathbf{p}} \,. \end{aligned} \tag{A.15}$$

Since our solution for $\mathbf{p}$ is already a perturbation expansion in the fields, a perturbation solution for $\mathbf{m}$ can be obtained by expanding

$$\mathbf{m} = \mathbf{m}^{(0)} + \lambda\,\mathbf{m}^{(1)} + \lambda^2\,\mathbf{m}^{(2)} + \cdots \ . \tag{A.16}$$

with the same perturbation parameter λ and inserting Eq. (A.9) into Eq. (A.15). Gathering terms of equal power in λ reveals

$$\mathbf{m}^{(1)} = \mathbf{0} \ , \tag{A.17}$$

$$\mathbf{m}^{(2)} = -\frac{\xi_2}{2q}\,\mathbf{p}^{(1)} \times \dot{\mathbf{p}}^{(1)} \ . \tag{A.18}$$

In a similar manner, perturbation solutions may be obtained for the electric quadrupole moment

$$\mathfrak{q}^{(1)} = \mathbf{0} \ , \tag{A.19}$$

$$\mathfrak{q}^{(2)} = -\frac{\xi_2}{2q}\,\mathbf{p}^{(1)}\mathbf{p}^{(1)} \ . \tag{A.20}$$

The magnetic quadrupole and electric octupole moments appear at third-order as discussed in the Supplementary Material.

A.3 Constitutive relations

The LOM can be used to obtain macroscopic constitutive relations for the polarization density, $\mathbf{P}$, the magnetization density, $\mathbf{M}$, and the electric quadrupolarization density, $\mathbf{Q}$ (and higher order terms if desired - see Supplementary Material) by treat-

ing matter as a collection of non-interacting oscillators each with their own resonant and damping frequencies and following the spatial averaging procedure in Ref. [7]. Assuming non-interacting oscillators is analogous to treating matter as an ensemble of non-interacting two-level, quantum mechanical systems – each oscillator represents a single two-level system. However, real materials often exhibit responses that imply coupling between more than two energy levels (and thus coupling between oscillators) which is beyond the scope of this work. Despite this, the extension of the LOM presented here can still describe many real optical phenomena.

For simplicity local field corrections are ignored (i.e. the local fields in Sec. A.2 are assumed equal to the macroscopic fields). Furthermore, the constitutive relations below are written assuming a homogeneous material consisting only of a single species of oscillator with number density N_s. Wherever it is necessary to consider multiple species the expressions below can be summed or integrated over all species. For example, in resonant effects (e.g. the photon drag effect - see Sec. A.4.3.1) a large response can come entirely from a single species of oscillator that may comprise a very small subset of the medium.

A.3.1 Polarization density

Since the solution for $\mathbf{p}$ is already a perturbation expansion in $\mathbf{E}$ and $\mathbf{B}$, a perturbation solution for $\mathbf{P}$ can be obtained by expanding

$$\mathbf{P} = \mathbf{P}^{(0)} + \lambda\,\mathbf{P}^{(1)} + \lambda^2\,\mathbf{P}^{(2)} + \cdots\ . \tag{A.21}$$

with the same perturbation parameter λ and following the spatial averaging procedure of Ref. [7]. Gathering terms of equal power in λ up to second-order and expressing

the results in the frequency-domain reveals

$$\tilde{\mathbf{P}}_i^{(1)}(\omega) = \varepsilon_0 N_s \, \boldsymbol{\alpha}^{(1)}(\omega) \cdot \tilde{\mathbf{E}}(\omega) \; , \tag{A.22}$$

and

$$\begin{aligned} \tilde{P}_i^{(2)}(\omega) = \varepsilon_0 \int_{-\infty}^{\infty} \mathrm{d}\omega_1 \int_{-\infty}^{\infty} \mathrm{d}\omega_2 \; \delta(\omega_1 + \omega_2 - \omega) \\ \Bigg\{ N_s \, \alpha_{ijkl}^{(L)}(\omega_1, \omega_2) \Big[i\omega_1 \tilde{E}_j(\omega_1) \epsilon_{klm} \tilde{B}_m(\omega_2) \\ + \tilde{E}_j(\omega_1) \nabla_k \tilde{E}_l(\omega_2) \Big] \\ + N_s \, \alpha_{ijk}^{(2)}(\omega_1, \omega_2) \, \tilde{E}_j(\omega_1) \tilde{E}_k(\omega_2) \Bigg\} \; , \end{aligned} \tag{A.23}$$

where the Lorentz polarizability is

$$\alpha_{ijkl}^{(L)}(\omega_1, \omega_2) \equiv \frac{-\xi_2 \varepsilon_0}{q} \, \alpha_{il}^{(1)}(\omega_1 + \omega_2) \, \alpha_{kj}^{(1)}(\omega_1) \; , \tag{A.24}$$

and the Pockels/Stark polarizability, $\boldsymbol{\alpha}^{(2)}$, is

$$\alpha_{ijk}^{(2)}(\omega_1, \omega_2) \equiv \frac{-\varepsilon_0^2}{q^3} \, k_{lmn}^{(2)} \, \alpha_{il}^{(1)}(\omega_1 + \omega_2) \, \alpha_{mj}^{(1)}(\omega_1) \, \alpha_{nk}^{(1)}(\omega_2) \; . \tag{A.25}$$

A.3.2 Magnetization

In a similar manner to $\mathbf{P}$, the perturbation solution for $\mathbf{M}$ up to second-order is

$$\mathbf{M}^{(1)} = \mathbf{0} \; , \tag{A.26}$$

$$\mathbf{M}^{(2)} = -\frac{\xi_2 N_s}{2q} \mathbf{p}^{(1)} \times \dot{\mathbf{p}}^{(1)} \; . \tag{A.27}$$

In the frequency-domain the last equation may be written as

$$\tilde{M}_i^{(2)}(\omega) = \epsilon_0 \int_{-\infty}^{\infty} \mathrm{d}\omega_1 \int_{-\infty}^{\infty} \mathrm{d}\omega_2 \; \delta(\omega_1 + \omega_2 - \omega) \\ N_s \, \alpha_{jklm}^{(M)}(\omega_1, \omega_2) \tilde{E}_j(\omega_1) \, \epsilon_{ikl} \, i\omega_2 \tilde{E}_m(\omega_2) \; , \tag{A.28}$$

where the Inverse Faraday polarizability is

$$\alpha_{jklm}^{(M)}(\omega_1, \omega_2) \equiv -\frac{\xi_2 \varepsilon_0}{2q} \alpha_{lj}^{(1)}(\omega_1) \, \alpha_{km}^{(1)}(\omega_2) \; . \tag{A.29}$$

Eqs. (A.27)-(A.29) agree with other classical calculations based on the Lorentz force [129, 130].

A.3.3 Electric quadrupolarization

Likewise the perturbation solution for $\mathbf{Q}$ up to second-order is

$$\mathbf{Q}^{(1)} = \mathbf{0} \; , \tag{A.30}$$

$$\mathbf{Q}^{(2)} = -\frac{\xi_2 N_s}{2q} \mathbf{p}^{(1)} \mathbf{p}^{(1)} \; . \tag{A.31}$$

In the frequency-domain the last equation may be written as

$$\tilde{Q}_{ij}^{(2)}(\omega) = \varepsilon_0 \int_{-\infty}^{\infty} \mathrm{d}\omega_1 \int_{-\infty}^{\infty} \mathrm{d}\omega_2 \; \delta(\omega_1 + \omega_2 - \omega) \\ N_s \, \alpha_{ijkl}^{(Q)}(\omega_1, \omega_2) \tilde{E}_k(\omega_1) \tilde{E}_l(\omega_2) \; . \tag{A.32}$$

where

$$\alpha_{ijkl}^{(Q)}(\omega_1, \omega_2) \equiv -\frac{\xi_2 \varepsilon_0}{2q} \, \alpha_{ik}^{(1)}(\omega_1) \, \alpha_{jl}^{(1)}(\omega_2) \; . \tag{A.33}$$

All of the susceptibilities defined above possess intrinsic permutation symmetry as expected [8].

A.4 Physical phenomena

Maxwell's equations require constitutive relations in order to be complete - without them it is impossible to predict the evolution of $\mathbf{E}$ of $\mathbf{B}$ in the presence of matter. Furthermore, the constitutive relations physically describe the interaction between the electromagnetic fields and matter and therefore contain all of the physical effects observed in experiments. The standard undergraduate approach (ignore $\mathbf{B}$, $\mathbf{M}$, $\mathbf{Q}$, and anharmonicity) captures a surprising number of linear optical effects. But by extending the LOM in the manner above many more optical effects can be accounted for both qualitatively and roughly quantitatively.

Every polarizability in the perturbation solutions for $\mathbf{P}$, $\mathbf{M}$, and $\mathbf{Q}$ (see Eqs. (A.22), (A.23), (A.28), and (A.32)) gives rise to one or more physical effects. The second-order effects are collectively known as three-wave mixing processes and are explored below.

A.4.1 Linear magneto-optic effects

Linear magneto-optic effects occur when the optical properties of a material have a linear dependence on a quasi-static magnetic field. Clearly these effects arise from the first term in Eq. (A.23). When a static magnetic field with strength $\mathbf{B}_0$ is present in an isotropic material the second-order response that depends on this field (given by Eq. (A.23)) is

$$\tilde{\mathbf{P}}^{(FZ)}(\omega) = i\omega\varepsilon_0 \, N_s \alpha^{(L)}(\omega, 0) \, \mathbf{B}_0 \times \tilde{\mathbf{E}}(\omega) \, . \tag{A.34}$$

When this polarization is inserted into the wave equation the cross product necessarily implies that it's contribution to the susceptibility is strictly off-diagonal and anti-symmetric which is the hallmark of the Faraday effect, Zeeman effect, and magneto-optic Kerr effect (MOKE) [89,119,131]. The qualitative and quantitative descriptions of the Faraday and linear, "normal" Zeeman effects provided by the LOM are quite remarkable (see Appx. A.6). However, the MOKE and its primary application – the surface magneto-optic Kerr effect (SMOKE) – generally use magnetic materials because the change in polarization is much larger. Since the LOM neglects both spin and exchange interactions which are fundamental to magnetism it cannot accurately predict the size of these effects in magnetic materials. Therefore, the main practical value in the LOM for describing the MOKE and SMOKE is that it correctly attributes these effects to consequences of the magnetic component of the Lorentz force.

A.4.2 Linear electro-optic effects

Linear electro-optic effects occur when the optical properties of a material have a linear dependence on a quasi-static electric field. These effects arise from the anharmonic (last) term in Eq. (A.23). When a static electric field with strength $\mathbf{E}_0$ is present in a non-centrosymmetric material the second-order response that depends linearly on this field (given by Eq. (A.23)) is

$$\tilde{\mathbf{P}}^{(SP)}(\omega) = 2\varepsilon_0 \, N_s \boldsymbol{\alpha}^{(2)}(0,\omega) : \mathbf{E}_0 \tilde{\mathbf{E}}(\omega) \; . \tag{A.35}$$

When this polarization is inserted into the wave equation the effective susceptibility is modified leading to the Pockels effect [89] (and linear Stark effect as argued below). The qualitative agreement with experimental results on the Pockels effect is excellent while the quantitative agreement (when using a reasonable estimation for $\mathbf{k}^{(2)}$) is less admirable but still decent [8].

In Appx. A.6 the connection between the Faraday and linear Zeeman effects as a reflection of the Kramers-Kronig relations was discussed. Since the Pockels and linear Stark effects are the electric analogs of the Faraday and linear Zeeman effects respectively one might suspect that they too are different aspects of the same physical interaction. In fact, W. Voigt's predictions for the Stark effect in 1901 were based on adding an anharmonic restoring force term to the LOM [132, 133]. Modern literature generally only associates the Pockels effect with the anharmonic restoring force making the linear Stark effect appear unrelated. However, there is simply no other way to represent a small linear resonance shift in a constitutive relation besides through $\boldsymbol{\alpha}^{(2)}$ (or $\boldsymbol{\chi}^{(2)}$). To remedy this, a simple argument for presenting both effects as $\boldsymbol{\alpha}^{(2)}$ effects is presented in Appx. A.7.

In principle linear electro-optic effects could also arise from Eqs. (A.28), (A.32), and the middle term of Eq. (A.23). However, in unstructured media their magnitudes are estimated to be at least d/λ times smaller than the standard $\boldsymbol{\chi}^{(2)}$ effects for off-resonant excitation where d is the lattice constant and λ is the wavelength of light. This comes by comparing the magnitudes of the polarizabilities in Eqs. (A.25) and (A.24) and using the standard estimate of $k^{(2)} = m\omega_0^2/d$ [8]. Still, in a centrosymmetric material (where $\boldsymbol{\chi}^{(2)} = \mathbf{0}$) it might be possible to observe them. On the other hand these effects could become appreciable in nano-scale devices or meta-materials where field gradients much stronger than E/λ can exist.

A.4.3 Difference-frequency generation and optical rectification

Both DFG and optical rectification (OR) occur when a material responds at the difference between two (typically optical) field frequencies. All of the second-order constitutive relations (Eqs. (A.23), (A.28), and (A.32)) support DFG and OR. The standard $\chi^{(2)}$ effects are covered extensively in the literature (e.g. Ref. [8]) so only the remaining terms will be discussed here.

The difference frequency part of the first term in Eq. (A.23) is a consequence of the transfer of linear momentum between the optical fields and matter known as the photon drag effect (PDE) - it is discussed in Sec. A.4.3.1. Eq. (A.28) leads to the Inverse Faraday effect which is the rotational analog of the PDE - it is discussed in Sec. A.4.3.2. The quadrupole response in Eq. (A.32) is of similar magnitude and is largest for two non-collinear beams or a single tightly-focused one. The second term of Eq. (A.23) combined with the PDE term has the same structure as the force on the center-of-mass (see Eq. (A.11)) that gives rise to optical tweezers [125]. Therefore, the LOM predicts that optical tweezers should polarize objects as they are accelerated so long as $m_e \neq m_n$. This, and the other effects in this section, lead to the conclusion that light preferentially imparts its momentum, angular momentum, and energy, to the lighter charge carrier which may subsequently transfer these quantities to its heavier partner via the restoring force.

A.4.3.1 Photon drag effect

One of the key features of the LOM is the ability to microscopically track the flow of energy and momentum. This makes the LOM a natural choice for describing the PDE which is characterized by the transfer of the Minkowski momentum ($n'\hbar\omega/c$) per quantum of light to the absorbing electrons in a material where n' is the real part of the refractive index of the medium and ω is the angular frequency of the light [134–136]. This momentum transfer polarizes the material parallel or anti-parallel to the direction of propagation of light. The PDE arises from the time-averaged (or difference-frequency) part of the first term of Eq. (A.23). However, since the PDE is most often seen in semiconductors one may first convert the LOM to the Drude model by taking $\omega_0 \to 0$ and examining the time-averaged current $\langle \mathbf{j}_P \rangle \equiv \langle \dot{\mathbf{P}} \rangle$.

Appx. A.8 tracks the energy and momentum of light quanta inside a material by

comparing the power and force provided by a plane wave propagating in a material. To summarize the results, the momentum of each quantum of light with energy $\hbar\omega_0$ propagating inside a material is the average of the Abraham and Minkowski values (given by Eq. (A.60)) which is exclusively transferred to the electrons (assuming $m_e \ll m_n$). An electron resonantly absorbing light acquires the Minkowski momentum per photon (Eq. (A.59)) while the remaining electrons receive the remaining momentum. These results agree with those derived using quantum optical and other classical methods [137,138]. By considering pulses of light the momentum transfer at surfaces versus in bulk can be distinguished [138,139].

The voltage predicted by the LOM for typical PDE experiments (open-circuit conditions) can be obtained by first calculating the electric field that counteracts the time-averaged Lorentz force acting on the resonant absorbers. Turning Eq. (A.58) into a force density acting on the electrons of identical oscillators under resonant illumination yields

$$\left\langle \mathbf{f}_{le}^{(1,2)} \right\rangle = \frac{\kappa I_0}{c} e^{-\kappa z}\, \hat{\mathbf{k}}\,, \tag{A.36}$$

where I_0 is the light's peak intensity (Poynting vector magnitude) in vacuum ignoring reflections, κ is the extinction coefficient, and the light is normally incident on the material's surface lying at $z = 0$. This assumes $N_s\alpha'' = \chi''$ where N_s is the number density of resonant absorbers (free carriers). This division of the medium into resonant oscillators (which only contribute to χ'') and host oscillators (which only contribute to χ') is appropriate for the materials used [140]. Eq. (A.36) is identical to the first equation in Ref. [136] - the induced voltage can be calculated by following that work which agrees very well with their experimental results. If all of the light is absorbed, an order of magnitude estimate of the voltage is $V \approx I_0/(qcN_s)$ where N_s is the number density of resonant absorbers. Recall that I_0/c is also the radiation pressure

from light. The physical upshot is that optical momentum transfer can polarize a material and/or drive a current so long as $m_e \neq m_n$.

A.4.3.2 Inverse Faraday effect

The inverse Faraday effect (IFE) is essentially the angular momentum analog of the photon drag effect. The extension of the LOM presented here predicts that circularly polarized photons each transfer an angular momentum of magnitude $\hbar$ to the electrons in a material. This transfer of angular momentum magnetizes the medium parallel or anti-parallel to the direction of propagation of light. The IFE arises from the time-averaged (or difference-frequency) part of Eq. (A.28).

Appx. A.9 tracks the energy and angular momentum of light quanta inside a material by comparing the power and torque provided by a plane wave propagating in a material. To summarize the results, the angular momentum of each quantum of light with energy $\hbar\omega_0$ propagating inside a material (given by Eq. (A.64)) is $\mathbf{0}$ for linearly polarized light and $\hbar\hat{\mathbf{k}}$ ($-\hbar\hat{\mathbf{k}}$) for left (right) circularly polarized light from the viewpoint of the receiver which is exclusively transferred to the electrons (assuming $m_e \ll m_n$). Unlike the linear momentum, this angular momentum is independent of the refractive index and the photon's energy and all of it is transferred to the electron that absorbs the photon.

The magnetic field created by the magnetization in Eq. (A.28) must satisfy Maxwell's equations and can be found using the Biot-Savart law. Note that although plane waves can produce a magnetization, they cannot induce a magnetic field – this would violate Gauss's law and is a reflection of the fact that plane waves carry zero total angular momentum [141]. So, Gaussian beams will be considered instead. For a medium composed of many species of oscillator, two limiting cases for the induced magnetic field are presented here - both ignore reflections and assume a monochromatic Gaussian beam with waist w_0 (the radius where the intensity falls to $1/e^2$ of its peak value)

and Jones vector $\boldsymbol{\mathcal{E}}$ is normally incident on a slab of material. Note that any material with a large Faraday effect should also have a large IFE [142].

Off resonance the magnetic field induced in the middle of a material whose length is much greater than w_0 is

$$\langle \mathbf{B} \rangle \approx \frac{i\pi\xi_2 I_0}{q\lambda_0 N c^2} \frac{(n'^2-1)^2}{n'^2}\, \hat{\boldsymbol{\mathcal{E}}} \times \hat{\boldsymbol{\mathcal{E}}}^* \,, \tag{A.37}$$

where N is the number density of all oscillators. This expression assumes the magnitudes of each polarizability are roughly equivalent far from any resonance. An order-of-magnitude estimate for the magnetic field induced by visible light in typical condensed matter is 1 μG/MW/cm^2 which agrees well with experiment [143]. In magnetic materials the effect can be orders of magnitude greater [144].

On resonance the magnetization is a manifestation of the optical orientation of spin carriers that is of interest to the spintronics community [145]. According to the LOM the induced magnetic field at the surface in the middle of the beam is

$$\langle \mathbf{B} \rangle = \frac{i\xi_2 I_v \lambda_0 \kappa^2}{8\pi q c^2 N_s}\, f\Big(\frac{w_0\kappa}{2}\Big)\; \hat{\boldsymbol{\mathcal{E}}} \times \hat{\boldsymbol{\mathcal{E}}}^* \,, \tag{A.38}$$

where I_0 is the light's peak intensity (Poynting vector magnitude) in vacuum ignoring reflections, κ is the extinction coefficient, and

$$f\,(x) \equiv 1 - \sqrt{\pi}\, x + x^2 e^{-x^2}\Big[\pi f_i(x) - f_e(x^2)\Big] \,, \tag{A.39}$$

where $f_i(x) \equiv \mathrm{erf}(ix)/i$ is the imaginary error function and $f_e(x) \equiv -\int_{-x}^{\infty} e^{-x}/x \; \mathrm{d}x$ is the exponential integral function. This expression uses the same approximation as Sec. A.4.3.1 namely that $N_s\alpha'' = \chi''$ where N_s is the number density of resonant absorbers. It also assumes *all* of the light is resonant. For a sense of scale, if all of the nuclear spins in GaAs point in the same direction the electrons see a magnetic

field of about 5 T [146]. This would correspond to an electron spin polarization of about 1% which can easily be achieved by exciting a material with resonant circularly polarized light [145]. Similar to the PDE, the IFE is a consequence of the conservation of angular momentum. The transfer of angular momentum from optical fields to the charge carriers in a material will magnetize it so long as $m_e \neq m_n$.

A.4.4 Sum-frequency and second-harmonic generation

Both sum frequency generation (SFG) and second harmonic generation (SHG) occur when a material responds at the sum of two (typically optical) field frequencies – in the latter the frequencies are the same. All of the second-order constitutive relations (Eqs. (A.23), (A.28), and (A.32)) support SFG and/or SHG. The standard $\chi^{(2)}$ effects are covered extensively in the literature (e.g. Ref. [8]) so only the remaining terms will be discussed here.

As discussed in Sec. A.4.2 the other second-order polarizabilities are expected to be at least approximately d/λ times smaller than $\boldsymbol{\alpha}^{(2)}$ where d is the lattice constant and λ is the wavelength of light. This limits the practical value of these other terms. Still, they have been observed in natural, centrosymmetric media [147–149]. It is worth noting these effects are largest when two orthogonally-polarized, non-collinear excitation beams are used. Furthermore, Eq. (A.28) implicitly forbids second-harmonic magnetization in isotropic media.

A.5 Summary

This work extends the LOM by retaining $\mathbf{B}$ in the equations of motion and also deriving expressions for the multipole moments $\mathbf{m}$ and $\mathfrak{q}$. The physical phenomena described via this extension are now united in a single classical model rather than phenomenological or quantum mechanical ones. Given this, the accuracy (both qualitative and quantitative) of the LOM is remarkable (discussed in Sec. A.4). The

advantage of this presentation is the simplicity of working with a two-body system and Newton's second law. This is ideal for educational settings, order-of-magnitude calculations, and building physical intuition.

There are several limitations to this presentation of the LOM worth noting. First, since spin is neglected it cannot describe magnetic materials, the anomalous Zeeman effect, etc. Second, there is no inclusion of acoustic (e.g. Raman or Brillouin) effects. Third, there are several "free" parameters (e.g. resonance frequency or oscillator strength) that must be known a priori (usually by experiment or quantum-mechanical calculation). Ultimately the trade-off made with the LOM is the surrender of veracity for simplicity which is indeed desirable under certain circumstances.

A.6 Faraday and Zeeman effects

Since Eq. (A.34) can be cast in a form similar to Eq. (A.22) one can define an effective linear polarizability of the oscillator as

$$\alpha_{ij}(\omega) = \alpha^{(1)}(\omega)\,\delta_{ij} + i\omega\,\alpha^{(L)}(\omega,0)\,B_{0,k}\,\epsilon_{ikj}\ . \tag{A.40}$$

The Levi-Civita symbol in the second term implies that its contribution is strictly anti-symmetric and off-diagonal. For a macroscopic medium composed of this single species of oscillators this leads to an induced circular birefringence in isotropic materials [89]. For plane waves propagating parallel to the applied magnetic field the eigenmodes are left and right circularly polarized with corresponding susceptibilities (via Eq. (A.24)) given by

$$\chi_{\pm}(\omega) = \chi^{(1)}(\omega) \pm \frac{\xi_2 \varepsilon_0 \omega B_0}{qN_s}\,\chi^{(1)}(\omega)\,\chi^{(1)}(\omega) \tag{A.41}$$

where + and − correspond to left and right circular polarizations respectively from the viewpoint of the receiver. In the limit $\gamma \ll \omega$ (which is true for most materials at optical frequencies), these susceptibilities can be written as

$$\chi_{\pm} = \chi^{(1)} \pm \omega_L \frac{\partial \chi^{(1)}}{\partial \omega} \, . \tag{A.42}$$

where $\omega_L \equiv \xi_2 q B_0/(2m)$. Comparing this to a Taylor expansion of $\chi^{(1)}$ reveals

$$\chi_{\pm}(\omega) \approx \chi^{(1)} \left(\omega \pm \omega_L\right) \tag{A.43}$$

assuming ω_L is sufficiently small. In normal matter $m_e \ll m_n$ so $\xi_2 \to 1$ and the applied magnetic field shifts the resonance by $\pm q B_0/(2m_e)$ which was the result Lorentz first obtained in 1896 [119]. Lorentz shared his theory with P. Zeeman which was used to calculate the charge to mass ratio of the oscillating charged particles in matter months before J. J. Thomson's discovery of the "corpuscle" and calculation of its charge to mass ratio [121, 150]. In the same year, J. Larmor obtained the same theoretical result as Lorentz using a classical model where the electron orbits a nucleus [151]. Furthermore, this shift is surprisingly the same as one predicted by a quantum mechanical treatment of a spin-less electron in an $l = 1$ state [152]. Using the known electron charge and mass, the linear Zeeman shift predicted by the LOM is approximately 1 MHz/G. Of course, the LOM cannot explain the "anomalous" Zeeman effect because spin is fundamental to the latter but neglected in the former.

Shortly after the discovery of the Zeeman effect it was realized that the Faraday and linear Zeeman effects were both manifestations of the same physical interaction which lead H. Becquerel to derive his expression for the Verdet constant [153]. The corresponding refractive indices for Eq. (A.42) are:

$$n_{\pm} = n_0 \pm \omega_L \frac{\partial n_0}{\partial \omega} \, , \tag{A.44}$$

where $n_0^2 \equiv 1 + \chi^{(1)}$. The specific rotatory power for Faraday rotation is $\rho \equiv \pi(n_+ - n_-)/\lambda$ where λ is the vacuum wavelength [89]. Using Eq. (A.44) this can be rewritten as $\rho = \mathcal{V}B_0$ where

$$\mathcal{V} = -\frac{\xi_2 q\lambda}{2mc}\frac{\partial n_0}{\partial \lambda} \,, \tag{A.45}$$

is the Verdet constant. This impressively accurate expression (with $\xi_2 \to 1$) was derived by Becquerel one year after Zeeman's discovery of the Zeeman effect [153]. Ultimately the connection between the Faraday and linear Zeeman effects exemplifies the relationship between the real and imaginary parts of the refractive index or susceptibility illustrated by the Kramers-Kronig relations. The shift of an absorption resonance must be accompanied by a change in phase velocity off-resonance [154].

In atomic Positronium, $m_e = m_n$ so $\xi_2 \to 0$ and the LOM correctly predicts that atomic Positronium should have zero linear "normal" Zeeman shift [155].

A.7 Stark and Pockels effects

Exploring the connection between the linear Stark and Pockels effects can be done by following a procedure similar to that used in Appx. A.6, assuming the optical electric field is weak enough, and using Eq. (A.22), (A.23), and (A.25). However, this approach depends critically on both the symmetry of the medium and the orientation of the applied quasi-static electric field. To keep the discussion as general as possible these details will be ignored. Instead, by comparing the first and last terms in Eq. (A.23) (and using Eqs. (A.22), (A.25), and (A.24) and the results of Appx. A.6) one may estimate the magnitude of the resonance shift as

$$\omega_S \equiv \frac{qk^{(2)}E_0}{2m^2\omega_0^3} \,. \tag{A.46}$$

Using the typical estimation of $k^{(2)} = m\omega_0^2/d$ where d is the lattice constant (see Ref. [8]) the linear Stark shift is approximately

$$\omega_S \approx \frac{qE_0\lambda_0}{4\pi mcd} \tag{A.47}$$

where λ_0 is the vacuum wavelength corresponding to the resonance. This expression agrees well with real experimental values. For example, using a "lattice" constant of the Bohr radius Eq. (A.47) predicts a linear Stark shift of 18 GHz/MV/m for the Lyman-α line in atomic Hydrogen whereas the real value is 40 GHz/Mv/m [152]. As another example, the predicted linear Stark shift for Nitrogen-vacancy defect centers in diamond is 13 GHz/MV/m while the measured value is approximately 6.3 GHz/MV/m [156].

Interestingly atomic Hydrogen exhibits a linear Stark effect despite the Coulomb force being spherically symmetric which seems to contradict the attribution of the Stark effect to an anharmonic restoring force. However, it is well known that the first excited states of atomic hydrogen that experience linear Stark shifts also possess permanent electric dipole moments even in the absence of an applied external field [157]. This implies a lack of inversion symmetry which is ultimately due to the angular momentum of each state. For the LOM this implies the restoring forces representing these transitions must lack inversion symmetry. In general, time-reversal symmetry guarantees that any non-degenerate state cannot have a permanent electric dipole moment hence no linear Stark shift either [158].

As suggested above, the linear Stark effect appears to be described both qualitatively and quantitatively by an anharmonic restoring force (and hence $\boldsymbol{\chi}^{(2)}$). Indeed the only form of constitutive relation that can describe the linear Stark effect is the last term in Eq. (A.23). Since the Pockels effect is well described by the off-resonant part of the same susceptibility this supports the claim that the Pockels and linear

Stark effects are simply different manifestations of the same physical interaction and that they are related through the Kramers-Kronig relations.

A.8 Photon momentum in matter

The momentum transferred per photon in matter can be determined by dividing the time-averaged rate of momentum transferred by a plane wave by the time-averaged rate at which photons are absorbed. Although the LOM is purely classical, photons can be realized by positing the quantization of the field energy in units of $\hbar\omega_0$ per photon. The time-averaged mechanical power absorbed from arbitrary fields by a single oscillator is then

$$\langle \mathcal{P}_m \rangle = \langle \mathcal{N} \rangle \, \hbar\omega_0 \; , \tag{A.48}$$

where $\langle \mathcal{N} \rangle$ is the average number of photons absorbed per unit time and the angled brackets denote time-averaging. On the other hand, the time-averaged rate of mechanical work done on each particle by the fields via the Lorentz force may be written as

$$\langle \mathcal{P}_n \rangle = \langle \dot{\mathbf{r}}_n \cdot \mathbf{F}_{ln} \rangle \qquad\qquad \langle \mathcal{P}_e \rangle = \langle \dot{\mathbf{r}}_e \cdot \mathbf{F}_{le} \rangle \; . \tag{A.49}$$

The velocities of each particle may be expressed in the center-of-mass coordinate system using Eqs. (A.3) and their perturbation solutions in Eqs. (A.10)-(A.13). To first order

$$\dot{\mathbf{r}}_n = \frac{m_e}{qM} \dot{\mathbf{p}}^{(1)} \qquad\qquad \dot{\mathbf{r}}_e = -\frac{m_n}{qM} \dot{\mathbf{p}}^{(1)} \; . \tag{A.50}$$

Similarly, the Lorentz forces can be Taylor expanded about the center-of-mass in the same manner as Sec. A.1.2 and the perturbation solutions for $\mathbf{p}$ and $\mathbf{R}$ inserted. Up

to second-order

$$\mathbf{F}_{ln}^{(1,2)} = q\mathbf{E} + \left(\frac{m_n}{M} - \xi_2\right)\left[(\mathbf{p}^{(1)}\cdot\nabla)\mathbf{E} + \dot{\mathbf{p}}^{(1)}\times\mathbf{B}\right] - \mathbf{k}^{(2)} : \mathbf{p}^{(1)}\mathbf{p}^{(1)} \tag{A.51}$$

$$\mathbf{F}_{le}^{(1,2)} = -q\mathbf{E} + \left(\frac{m_e}{M} + \xi_2\right)\left[(\mathbf{p}^{(1)}\cdot\nabla)\mathbf{E} + \dot{\mathbf{p}}^{(1)}\times\mathbf{B}\right] + \mathbf{k}^{(2)} : \mathbf{p}^{(1)}\mathbf{p}^{(1)} \ . \tag{A.52}$$

So the leading order powers delivered to each particle are

$$\langle\mathcal{P}_n\rangle = \frac{m_e}{M}\left\langle\dot{\mathbf{p}}^{(1)}\cdot\mathbf{E}\right\rangle \qquad\qquad \langle\mathcal{P}_e\rangle = \frac{m_n}{M}\left\langle\dot{\mathbf{p}}^{(1)}\cdot\mathbf{E}\right\rangle \ . \tag{A.53}$$

For ordinary matter $m_e \ll m_n$ which implies that all of the energy delivered by light goes to the electron and not the nucleus. This limit will be taken throughout the remainder of this section for simplicity.

Using the solution to Eq. (A.12), the total power absorbed by an isotropic oscillator from a plane wave with angular frequency ω and Jones vector $\boldsymbol{\mathcal{E}}$ is

$$\langle\mathcal{P}_m\rangle = \frac{\varepsilon_0\omega\alpha''}{2}\left|\boldsymbol{\mathcal{E}}\right|^2 , \tag{A.54}$$

where $\alpha'' \equiv \mathrm{Im}[\alpha(\omega)]$. Comparing this result to Eq. (A.48) reveals that

$$\langle\mathcal{N}\rangle = \frac{\varepsilon_0\alpha''}{2\hbar}\left|\boldsymbol{\mathcal{E}}\right|^2 . \tag{A.55}$$

As expected $\langle\mathcal{N}\rangle$ is proportional to the imaginary part of $\alpha^{(1)}$ (and hence the absorption coefficient) and to the square of the electric field amplitude (and hence the optical power).

By Newton's second law, the Lorentz forces $\mathbf{F}_{ln}$ and $\mathbf{F}_{le}$ (see Eqs. (A.51) and (A.52)) are the rates at which momentum is being transferred from the fields to

the nucleus and electron respectively. For centrosymmetric, ordinary matter where $m_e \ll m_n$ the time-averaged forces produced by arbitrary fields are

$$\left\langle \mathbf{F}_{ln}^{(1,2)} \right\rangle = \mathbf{0} \tag{A.56}$$

$$\left\langle \mathbf{F}_{le}^{(1,2)} \right\rangle = \left\langle (\mathbf{p}^{(1)} \cdot \nabla)\mathbf{E} \right\rangle + \left\langle \dot{\mathbf{p}}^{(1)} \times \mathbf{B} \right\rangle \ . \tag{A.57}$$

Again all of the momentum is delivered to the electron because only it is accelerated by the fields. The restoring force then transfers momentum to the nucleus. For the same plane wave considered earlier with complex wave vector $\mathbf{k} = (k' + ik'')\hat{\mathbf{k}}$,

$$\left\langle \mathbf{F}_{le}^{(1,2)} \right\rangle = \frac{\varepsilon_0}{2} \left(\alpha'' k' - \alpha' k''\right) |\boldsymbol{\mathcal{E}}|^2 \, \hat{\mathbf{k}} \ . \tag{A.58}$$

Suppose that the frequency of the plane wave is resonant with the oscillator as is the case for common PDE experiments where resonant light excites free carriers [134–136]. Then, $\alpha' = 0$ and dividing Eq. (A.58) by Eq. (A.55) reveals that each resonant electron receives a momentum of

$$\langle \boldsymbol{\Upsilon} \rangle_M = \frac{n' \hbar \omega}{c} \, \hat{\mathbf{k}} \ , \tag{A.59}$$

per photon where $n^2 \equiv 1 + \chi^{(1)}(\omega)$ is the square of the refractive index at ω and $k = n\omega/c$ was assumed. This is precisely the Minkowski value.

However, the total momentum of the photon (which is determined by the refractive index) is still unknown. To find it, a similar approach can be taken but the entire material (treated as a collection of multiple oscillator species) must be considered instead of just a single oscillator. Equations that are the volume density equivalents of Eq. (A.58) and Eq. (A.55) can then be obtained (the left-hand-sides are now a force density and a number of photons absorbed per unit volume while on the right-

hand-side $\alpha \to \chi$). Taking their ratio reveals the total momentum per photon is

$$\langle \boldsymbol{\Upsilon} \rangle_{AM} = \frac{\hbar\omega}{c} \frac{n' + n'^{-1}}{2} \hat{\mathbf{k}} \,. \tag{A.60}$$

where $n''^2 \ll 1$ was assumed. Eq. (A.60) implies that when photons are inside a material their total momentum is the average of the Abraham and Minkowski values which agrees with other derivations [137, 138].

A.9 Photon angular momentum in matter

The angular momentum of a photon in matter can be determined following a similar procedure to Appx. A.8 but tracking torque instead of force. To leading order the time-averaged torque in the center of mass frame from the Lorentz force on each particle is

$$\boldsymbol{\tau}_n \approx \frac{m_e}{M} \mathbf{p}^{(1)} \times \mathbf{E} \qquad\qquad \boldsymbol{\tau}_e \approx \frac{m_n}{M} \mathbf{p}^{(1)} \times \mathbf{E} \,. \tag{A.61}$$

In the limit of $m_e \ll m_m$, then

$$\boldsymbol{\tau}_n = \mathbf{0} \qquad\qquad \boldsymbol{\tau}_e = \mathbf{p} \times \mathbf{E} \,, \tag{A.62}$$

and all of the angular momentum is delivered to the electron.

A plane wave with Jones vector $\boldsymbol{\mathcal{E}}$ delivers a time-averaged torque to the electron of an isotropic oscillator of

$$\langle \boldsymbol{\tau}_e \rangle = \frac{i\varepsilon_0 \alpha''}{2} \boldsymbol{\mathcal{E}} \times \boldsymbol{\mathcal{E}}^* \,. \tag{A.63}$$

Dividing Eq. (A.55) by Eq. (A.63) we find the average angular momentum deliv-

ered per absorbed photon is

$$\langle \boldsymbol{\mathcal{L}} \rangle = i\hbar\, \hat{\boldsymbol{\mathcal{E}}} \times \hat{\boldsymbol{\mathcal{E}}}^{*} \,. \tag{A.64}$$

For linearly polarized light, $\langle \boldsymbol{\mathcal{L}} \rangle = \mathbf{0}$ while for left (right) circularly polarized light $\langle \boldsymbol{\mathcal{L}} \rangle$ is $\hbar\hat{\mathbf{k}}$ ($-\hbar\hat{\mathbf{k}}$). Note that the transferred angular momentum does not depend on the photon energy nor the refractive index like the transferred linear momentum does.

The total angular momentum of a photon in matter can be calculated by considering a material composed of many oscillators rather than a single oscillator. One finds the photon's total angular momentum is also given by Eq. (A.64). This implies the angular momentum is only transferred to the electrons responsible for absorption (this contrasts with the PDE).

APPENDIX B

Fourier transform spectroscopy

Fourier transform spectroscopy is an umbrella term for any technique that measures coherences in a radiative source (typically light). When applied in the infrared spectral range, the technique is FTIR and is a predecessor of dual-comb spectroscopy [11]. The standard approach to FTIR is depicted in Fig. B.1.

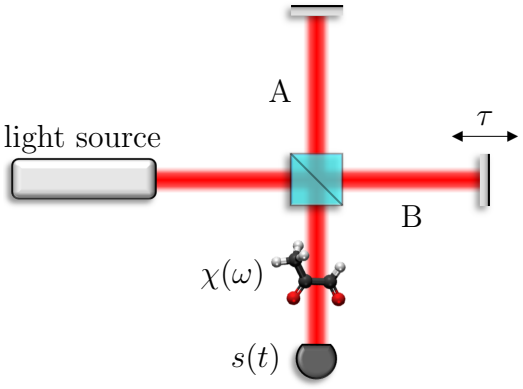

Figure B.1: Basic schematic for Fourier transform spectroscopy. An arbitrary light source is sent into a Michelson interferometer with fixed arm A and scanning arm B with total temporal delay τ. The sample of interest with susceptibility $\chi(\omega)$ is usually placed in front of the detector whose signal is $s(t)$.

The part of the signal that depends on both arms is

$$s(t;\tau) \propto \mathbf{E}_{\mathrm{A}}(t) \cdot \mathbf{E}_{\mathrm{B}}(t;\tau) \ , \tag{B.1}$$

or, in the frequency-domain (see Chap. II for convention),

$$\tilde{s}(\omega;\tau) \propto \int_{-\infty}^{\infty} \mathrm{d}\omega_1 \int_{-\infty}^{\infty} \mathrm{d}\omega_2 \; \tilde{\mathbf{E}}_{\mathrm{A}}(\omega_1) \cdot \tilde{\mathbf{E}}_{\mathrm{B}}(\omega_2;\tau) \; \delta(\omega - \omega_1 - \omega_2) \; , \tag{B.2}$$

where the fields are spatially evaluated in front of the detector. Assuming each beam has the same polarization, the time-averaged signal on the detector (or zero-frequency component) is then

$$\tilde{s}(0;\tau) \propto \int_{-\infty}^{\infty} \mathrm{d}\omega \; \tilde{E}^*_{\mathrm{A}}(\omega) \tilde{E}_{\mathrm{B}}(\omega;\tau) \; . \tag{B.3}$$

(To avoid the $1/f$ noise associated with measuring a low-frequency signal, several tricks could be used such as placing an acousto-optic modulator in one or both arms – I don't know if this is actually done in practice). The time-delay in arm B manifests as a phase ramp in the frequency-domain since $\mathbf{E}_{\mathrm{B}}(t;\tau) = \mathbf{E}_{\mathrm{B}}(t-\tau;0)$ (see Fourier shift theorem in Chap. II) so

$$\tilde{s}(0;\tau) \propto \int_{-\infty}^{\infty} \mathrm{d}\omega \; \tilde{E}^*_{\mathrm{A}}(\omega) \tilde{E}_{\mathrm{B}}(\omega;0) \, e^{-i\omega\tau} \; . \tag{B.4}$$

The effect of the material under study is a multiplicative transfer function in the frequency-domain for a plane wave (i.e. linear response). Ignoring reflections, one has

$$\begin{aligned} \tilde{s}(0;\tau) &\propto \int_{-\infty}^{\infty} \mathrm{d}\omega \; \tilde{E}^*_{\mathrm{A}}(\omega) e^{in^*(\omega)\omega L/c} \tilde{E}_{\mathrm{B}}(\omega;0) e^{-in(\omega)\omega L/c} \, e^{-i\omega\tau} \\ &\propto \int_{-\infty}^{\infty} \mathrm{d}\omega \; \tilde{E}^*_{\mathrm{A}}(\omega) \tilde{E}_{\mathrm{B}}(\omega;0) e^{\kappa(\omega)L} \, e^{-i\omega\tau} \; , \end{aligned} \tag{B.5}$$

where $n^2(\omega) \equiv 1 + \chi(\omega)$ is the square of the refractive index, $\kappa(\omega) \equiv n''\omega/c$ is the extinction coefficient, $n'' \equiv \mathrm{Im}[n]$, L is the material's length, and the fields are now

evaluated at a the point before the sample.

Even if the fields before the sample are known, Eq. (B.5) cannot be directly solved for κ. Now we'll see why it's called Fourier transform spectroscopy. If data is collected for many different τ (called an interferogram) then one can Fourier transform over τ. In practice, the signal is usually undersampled in time (this limits the amount of optical bandwidth usable before alias overlap occurs, but allows high resolution measurements with fewer points). This introduces a super-handy delta function on the right-hand side,

$$\begin{aligned}\tilde{s}(0;\omega_\tau) &\propto \int_{-\infty}^{\infty} \mathrm{d}\omega\ \tilde{E}^*_{\mathrm{A}}(\omega)\tilde{E}_{\mathrm{B}}(\omega;0)e^{\kappa(\omega)L}\,\delta(\omega+\omega_\tau) \\ &\propto \tilde{E}_{\mathrm{A}}(\omega_\tau)\tilde{E}^*_{\mathrm{B}}(\omega_\tau;0)e^{-\kappa(\omega_\tau)L}\ , \end{aligned} \tag{B.6}$$

and leaves us with a simple algebraic equation for $\kappa(\omega)$.

Note that if the sample were placed at the entrance to the Michelson interferometer (see Fig. B.1) the same result would be obtained. These two arrangements (where both fields pass through the sample) are called collinear (or symmetric) FTS. They only obtain information about absorption – that is, all phase information is lost. On the other hand, if the sample were placed in arm A or B (so that only one field passes through the sample albeit twice) the arrangement is called dispersive (or asymmetric) FTS and phase information (i.e. the real part of the refractive index) is retained. DCS also has the same two types of arrangement.

FTS techniques even work with incoherent light sources such as thermal light which can greatly reduce the complexity and cost of commercial applications. At first this may seem strange given that FTS relies on interference. The key insight is that the sample creates a coherence in the transmitted light with a timescale related to widths of its spectral lines.

The main ideas behind FTS are summarized in Fig. B.2.

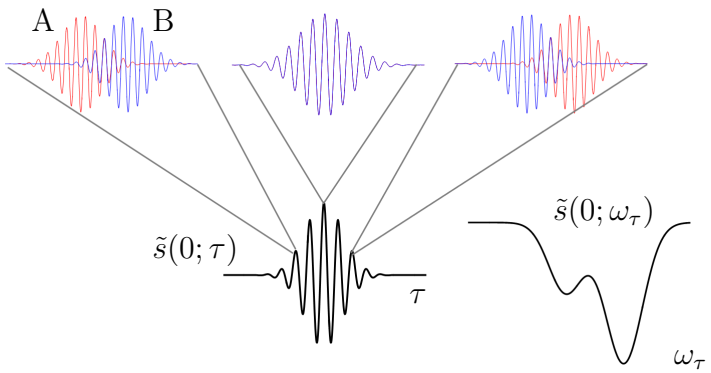

Figure B.2: Cartoon of Fourier transform spectroscopy with pulses of light. As the delay between the two arms is scanned the averaged detector value, $\tilde{s}(0;\tau)$, is recorded for each time delay τ and is called an interferogram. It's Fourier transform with respect to τ, $\tilde{s}(0;\omega_\tau)$, contains the spectral information of the sample.

APPENDIX C

Homemade combs

In this section are some specifics regarding two mode-locked, Ti:sapphire oscillators that I assembled (this is not intended to be a tutorial on mode-locked laser design). The first is a 93.5 MHz, >100 mW, >100 nm, linear-cavity oscillator (see Fig. C.1(a,b)) used for the experiment in Chap. VI. Some of its parts came from the first self-referenced comb [21]. During its construction I found Ref. [159] to be particularly helpful in addition to conversations with Bachana Lomsadze. The second laser is a bi-directionally mode-locked, 935 MHz, >300 mW, >15 nm, ring-cavity oscillator (see Fig. C.1(a,c)) which was largely influenced by Refs. [45, 160]. It will be used to validate the results in Chap. III.

Both lasers use a 2 mm Brewster-cut Ti:sapphire (unknown dopant concentration) crystal mounted in a copper housing which is water cooled to 20°C by an ancient Neslab refrigerating chiller (see Figs. C.1(b,c) for close-ups). Curved mirrors ($R =$ 10 cm in linear cavity and $R \approx 3$ in ring cavity) on either side of the crystal are angled at 20° to compensate for the astigmatism introduced by the Brewster-cut crystal. The linear cavity uses a fused-silica, Brewster-angled prism pair (I identified the material by measuring the apex angle and calculating the refractive index) for dispersion compensation while the ring cavity uses chirped mirror coatings (unknown

chirp) on all the cavity mirrors (except the output coupler). Both lasers are pumped by the same 532 nm diode-pumped solid-state laser (Sprout-G 18 W from Lighthouse Photonics) – usually 4.5 W for the linear cavity and 5.1 W for the ring cavity (both measured immediately before the respective pump lenses). Two pairs of PBSs and HWPs facilitate individual pump power control (visible in Fig. C.1(a)). Mode-locking for the linear cavity was usually initiated by pulling on a string attached to the first prism and for ring cavity by lightly striking the black breadboard with a 3/16 inch ball end hex driver.

Both combs also feature "loose" repetition rate locking (only slow drifts can be removed). The output coupler of the linear cavity and a folding mirror in the ring cavity are both mounted on single axis translation stages giving coarse, manual repetition rate control. In between the driving micrometer and the stage is a piezoelectric actuator (20 μm travel, 100 V for the linear cavity and unknown for the ring cavity) allowing precise, electronic control of the repetition rates. However, in this configuration the actuators have to move relatively large amounts of mass (as opposed to only moving a small optic) which greatly reduces the system's mechanical resonant frequency. Therefore, only repetition rate drifts can be corrected – the remaining noise in an experiment is monitored using CW lasers and corrected using the post-processing techniques described in Appx. D. To control the actuators, a feedback or "correction" signal is needed. This is generated by picking off a small percentage of the output beam from each laser and sending it to a high-speed, amplified photodetector. A single harmonic (typically first) of the repetition rate is filtered using a tunable band-pass filter and then amplified to an appropriate level for mixing. This signal is then mixed with a stable reference (provided by a DDS for the linear cavity and a function generator for the ring cavity) and filtered with a 100 kHz low-pass filter thereby generating an "error" signal. The error signal is fed into JILA built phase-locked loop (PLL) which has both proportional (gain) and integral

functionality to generate the correction signal. The correction signal is then sent to the piezo-controller which drives the actuator. The offset frequencies are completely free-running but usually do not drift more than several MHz per hour which is acceptable for performing an experiment. If needed, the offset frequencies can be manually adjusted by yawing the end mirror of the linear cavity or any mirror in the ring cavity.

For troubleshooting any problem with these lasers, two lab notebook exist – one for each laser. In addition, both Grace Kerber and Yiming Gong can operate these lasers and are familiar with their design and common troubleshooting techniques. And of course I am happy to assist in any way that I can.

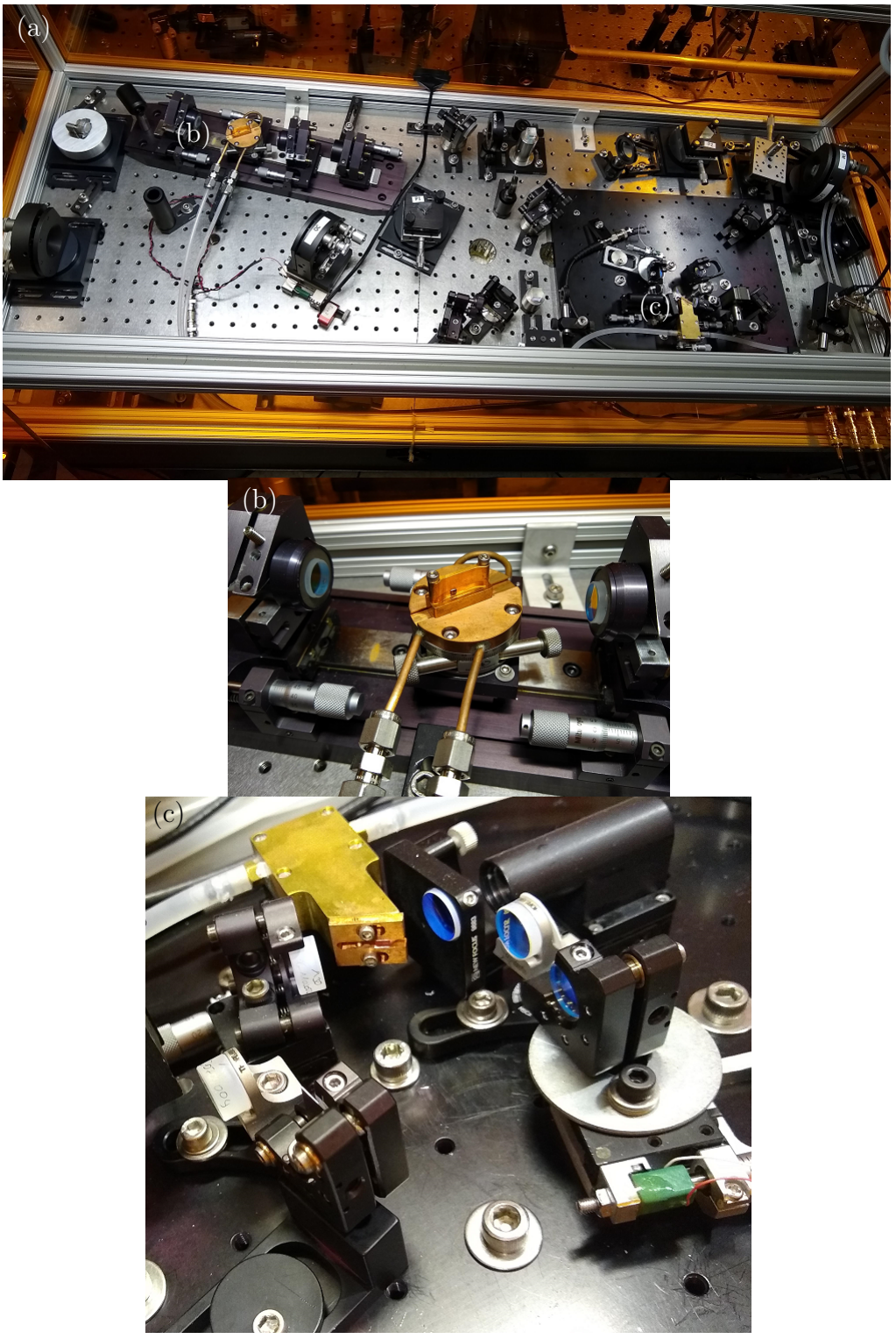

Figure C.1: (a) two homemade Ti:sapph frequency combs sharing one pump laser. (b) close-up of Brewster-cut, 2 mm Ti:sapph crystal and spherical curved mirrors for astigmatism correction in 93.5 MHz oscillator. (c) close-up of bi-directional 935 MHz mode-locked ring laser.

APPENDIX D

Post processing

For the standard implementation of DCS in which both repetition rates are nearly equal, the equation describing the rf comb is

$$y(t) = \sum_n A_n \, e^{2\pi i (n \, \Delta f_{\mathrm{rep}} + \Delta f_{\mathrm{off}}) t} \, . \tag{D.1}$$

This can be derived by calculating the product of the electric fields of two combs that each are each described by Eq. (2.10). From Eq. (D.1) it is clear that the rf comb is has its own repetition rate and offset frequency which are simply the difference in the optical repetition and offset frequencies of the combs that generated the signal. The amplitudes of the rf comb teeth, A_n, are the product of the amplitudes of the optical teeth that generated each line multiplied by the appropriate frequency component of the detector transfer function.

Any noise in the optical comb teeth (amplitude, repetition, offset) will be down-converted into the rf comb appropriately. All of the combs used in this work are "free-running" (see Ref. [12] for a discussion) and so the optical comb teeth are sufficiently noisy such that all digitized rf comb data do not show any comb structure upon Fourier transformation. An example of some real data is shown in Fig. D.1.

This appendix details the approaches taken in this dissertation that measure and remove noise from the rf comb.

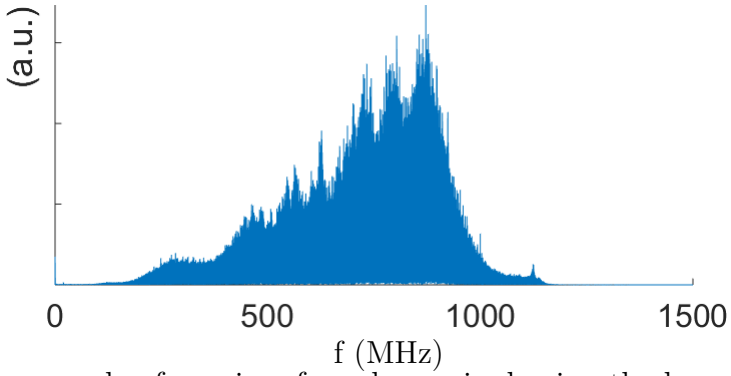

Figure D.1: An example of a noisy rf comb acquired using the laser diode combs of Chap. IV. No comb structure is visible (even on short time scales).

The only way DCS achieves a reasonable SNR is through the coherent use of many interferograms. This can be accomplished through coherent averaging as is required for real-time, long-running demonstrations [91,93] or equivalently by Fourier transforming a single data record containing many interferograms. Both approaches yield identical results when performed correctly (see Fig. D.5 and later discussion). Both of these techniques also require that all interferograms are identical to one another (this specifically refers to the number of data points per interferogram and the timing and phase of the envelope and carrier respectively). Rather than tightly locking the combs, the DCS community favors the use of free-running combs because for outside-the-lab applications, the environment may add considerable noise regardless. This leads to noisy rf combs like that in Fig. D.1. As such, a variety of data processing techniques have emerged, some of which have the potential to operate in real-time [71,94,161].

One approach we frequently use utilizes CW lasers as local oscillators to track fluctuations of the optical comb teeth [94]. In this technique, the frequency of a CW laser with a linewidth small compared to the FSR of either comb is tuned such that it is near one comb tooth from each comb. Beat notes between the CW laser and these

comb teeth are detected using heterodyne detection, electrically filtered and amplified, then digitized (analog techniques also exist for CW correction [92]). Each beat note is back-and-forth filtered (to remove group delay) using infinite impulse response (IIR) band-pass filters (using the `filtfilt` function in MATLAB) then added to its Hilbert transform to remove negative frequency components. Since finite impulse response (FIR) filters usually require more orders than IIR filters their use leads to significantly longer data processing. Amplitude noise is removed by normalizing all signals in the time-domain since only the phase is used for correction. If the frequency of the CW laser lies in between the optical comb teeth then the two beat notes are multiplied together in the time-domain. Otherwise, the beat note with the lower frequency is complex conjugated and then multiplied with the other one. This removes all fluctuations originating from the CW. All that remains is a single beat note between the two optical comb teeth capturing their relative fluctuations. This is equivalent to filtering out a single comb tooth from the rf comb and removing its amplitude noise. This beat note can be treated as a correction signal and is conjugated then multiplied with a one-sided version of the rf comb in the time-domain. This locks the corresponding rf comb tooth to DC thereby removing the offset noise from all the rf comb teeth leaving only repetition rate noise which now stretches the rf comb teeth relative to the comb tooth at DC. The results of applying this offset correction technique to the noisy rf comb shown in Fig. D.1 are shown in Fig. D.2.

Note that all of these noise reduction techniques require that the relative timing of all error signals is correct meaning that they track fluctuations that happened at the same time in the lab. This should always be the first check in troubleshooting! Once the offset correction is done, a second CW laser can be used to track repetition rate fluctuations [94] or a numerical approach can be taken. Both have the same underlying approach for correcting the signal and since a CW approach was examined in detail for the offset correction, a numerical approach will be detailed next, specifi-

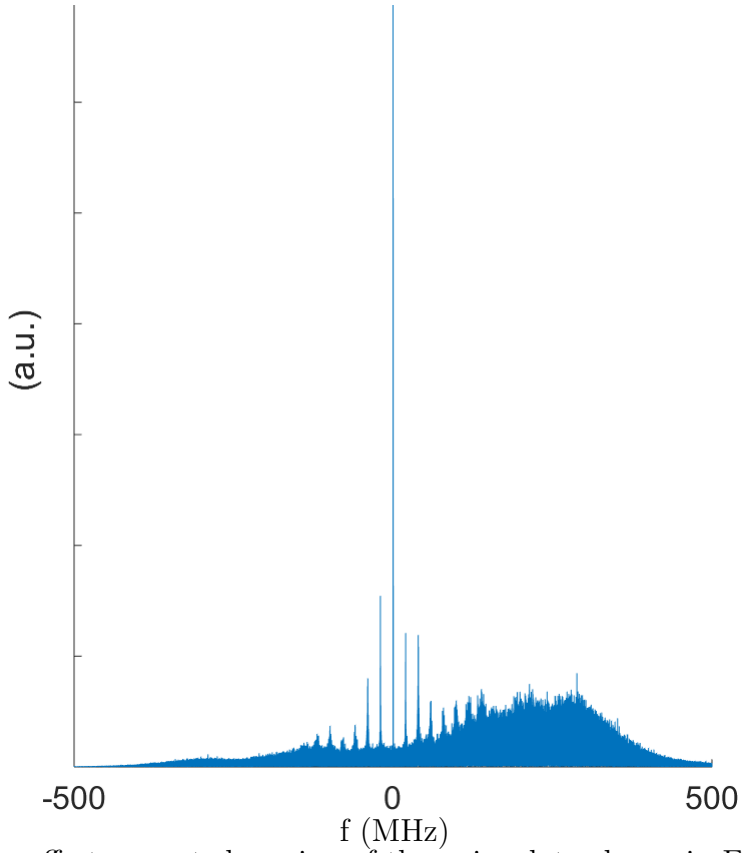

Figure D.2: The offset-corrected version of the noisy data shown in Fig. D.1. A CW laser monitored fluctuations in one comb tooth from each optical comb. These beat notes were mixed together generating a correction signal that was mixed with the noisy rf comb to lock down one of its teeth to DC.

cally DDFG [161]. In essence, a fluctuating repetition rate means that sometimes the signal is progressing too fast or too slow. One way to correct this is to resample the data onto a uniformly spaced time-axis. Alternatively, the necessary interpolation can be performed implicitly using a NUFFT [71, 162]. In either case, a clock must be generated which follows the fluctuations in the repetition rate. One means to accomplish this is to multiply the rf comb by its complex conjugate in the time-domain (hence the name DDFG). In the frequency-domain this corresponds to beating all of the rf comb teeth among each other which yields harmonics of the repetition rate as shown in Fig. D.3. For the two-CW approach, the mth harmonic of the repetition rate is calculated where m is the number of comb modes separating the CW lasers. In either case, one of the harmonics is back-and-forth IIR band-pass filtered (again

using MATLAB's `filtfilt` function) and added to its Hilbert transform. In my experience the narrowness of the required filter often makes it unstable, thus requiring an initial low-pass filtering, followed by decimation, then band-pass filtering, followed by upsampling to the original rate, and lastly the removal of negative frequencies. The phase of this clock is then unwrapped. Resampling is accomplished by interpolating the comb data in the time-domain using MATLAB's `interp1` function (with `pchip` option) such that uniform clock phase steps are taken. The comb structure can then be revealed using a standard FFT. Alternatively, the clock can be used to identify the non-uniform time-axis within the noisy data which can be corrected using a NUFFT as mentioned earlier [162]. For the resampling approach it is absolutely critical that the chosen phase step size creates interferograms that all have the same integer number of points thus guaranteeing that the same interferogram points are sampled each time (recall that the offset frequency was removed by during the offset correction step). Furthermore, the final data set must be truncated such that an integer number of interferograms remain. These conditions ensure that when Fourier transformed, the rf comb teeth line up exactly with the frequency grid ensuring that all of their energy is truly contained within a single bin. This not only maximizes the SNR, but is necessary to avoid any artificial systematic error effects. For example, choosing the wrong frequency grid leads to an effect similar to transmitting a frequency comb through a Fabry-Perot whose FSR does not match that of the comb. As such a periodic ripple is imprinted on the comb teeth. When the resampling is done appropriately to the offset-corrected data in Fig. D.2 the fully corrected rf comb spectrum emerges as shown in Fig. D.4. For dual-comb signals with large temporal dead-time (i.e. low-duty cycle bursts), the spectral SNR can be improved through temporal apodization (windowing). This takes advantage of the fact that in such scenarios the temporal SNR highly non-uniform – windowing diminishes the influence of low SNR points which would otherwise mostly contribute noise to the spectrum.

This comes at the cost of reduced spectral resolution – the resulting spectrum is the convolution of the original high-resolution spectrum with the coarser spectrum of the apodizer. Essentially, apodization is analogous to spectral smoothing. In Chap. V this technique was leveraged by multiplying the fully corrected time-domain data with a unit-amplitude Gaussian pulse train with a repetition period identical to the fully corrected data.

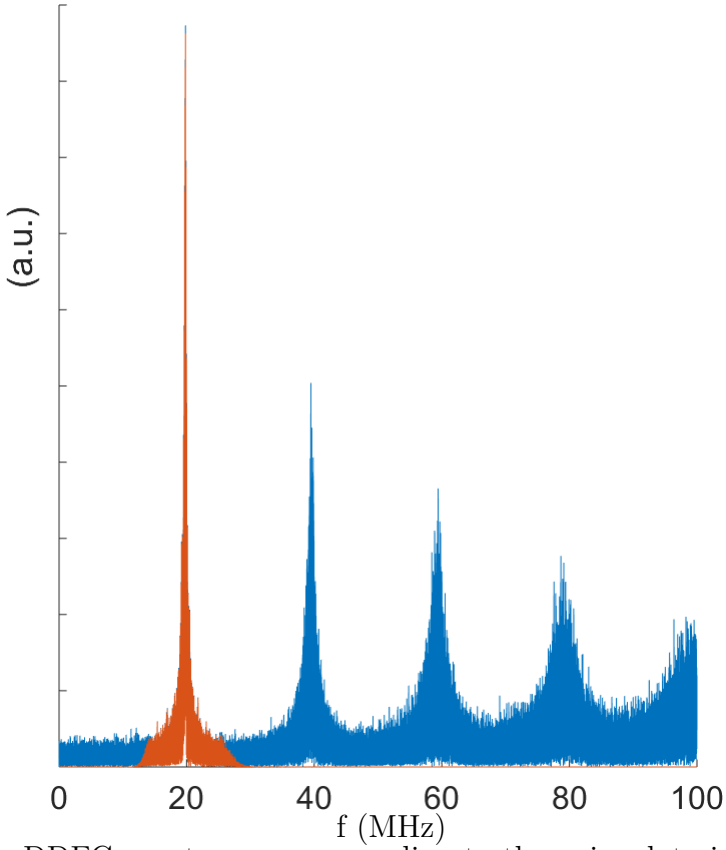

Figure D.3: The DDFG spectrum corresponding to the noisy data in Fig. D.1. The first harmonic is back-and-forth filtered using a one-sided IIR filter to act as a clock for resampling for repetition rate correction.

Now that the data has been fully corrected, one might suspect that averaging all of the corrected interferograms together could further improve the SNR. After all, averaging in most contexts leads to an SNR improvement equal to $\sqrt{N}$ where N is the number of objects averaged together. However, because the fully corrected comb shown in Fig. D.4 already represents all of the interferograms, one might argue it is

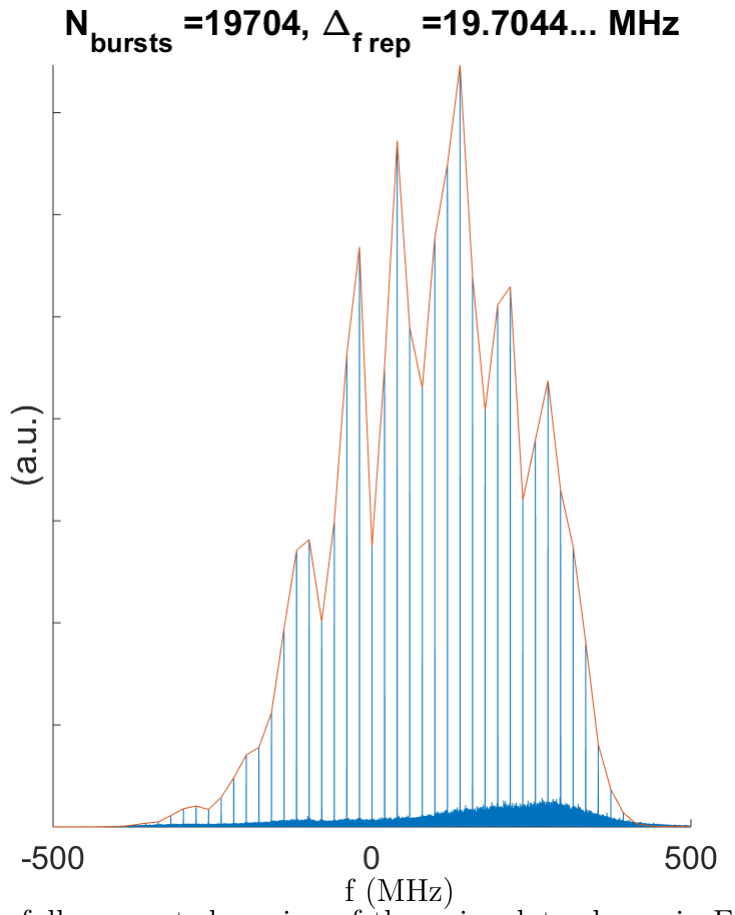

Figure D.4: The fully corrected version of the noisy data shown in Fig. D.1 using a CW laser for offset correction and DDFG for repetition rate correction.

nonsensical to expect that the *same* data could be used again to further enhance the SNR. Fig. D.5 shows side-by-side comparisons of the fully corrected comb in Fig. D.4 and three others generated using coherent averaging. Indeed no improvement in SNR is observed. This can be explained as follows: averaging does produce an interferogram with an SNR that is $\sqrt{N}$ times better but this also reduces the length of the data record. As such, the remaining noise is now concentrated in N times fewer frequency bins. This leads to an increase in the noise per bin by a factor of $\sqrt{N}$ in terms of amplitude because the noise adds in quadrature. Thus, the overall SNR remains constant. One practical difference between these two approaches is that coherent averaging produces a much smaller file size because only a single (or two) interferogram(s) need to be stored. Therefore, coherent averaging enables long-

running DCS implementations – which generally require a field-programmable gate array (FPGA) – that could in principle run indefinitely [93].

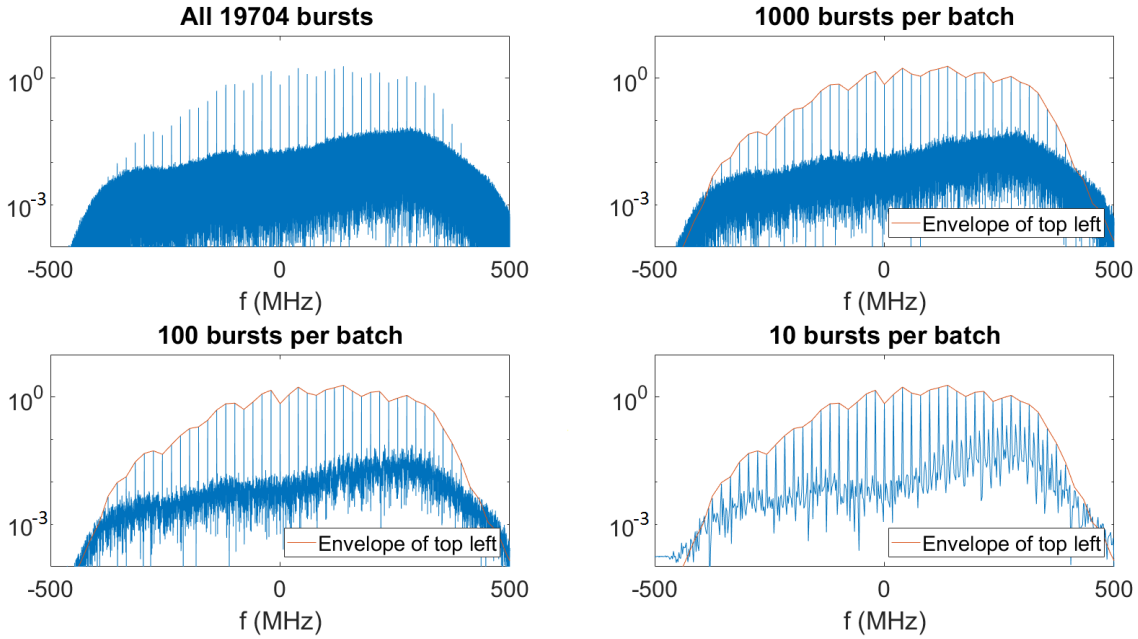

Figure D.5: Comparison of (a) the "full record" approach where a single, long train of approximately 19,704 interferograms are Fourier transformed vs (b)-(d) coherent averaging in which batches of interferograms are averaged together then Fourier transformed. All plots use the same data set which has been fully corrected and the y-axis is logarithmic. Clearly, both approaches yield identical results.

The most impressive numerical approach to correcting DCS spectra uses a Kalman filter [71]. It is impressive because it works even in situations where no comb structure is visible during any temporal slice of the data which usually baffle other techniques. This technique is currently being adapted for use in Chap. IV.

APPENDIX E

Multi-dimensional coherent spectroscopy

In this appendix, I present a brief nonlinear analog to Appx. B which lies at the heart of how MDCS experiments work. Indeed, MDCS can be thought of as a nonlinear version of FTS – the crux of each lies in measuring the temporal coherences that result when light interacts with matter. For this reason, I think a more descriptive name for MDCS would be nonlinear Fourier transform spectroscopy or $\boldsymbol{\chi}^{(3)}$ spectroscopy - it kind of rhymes too. Regardless, MDCS spectrally resolves $\boldsymbol{\chi}^{(3)}$ which contains much more information than its linear counterpart [101]. Throughout this appendix, the Fourier transform convention used is

$$\tilde{\mathbf{g}}(\omega) \equiv \int_{-\infty}^{\infty} \mathrm{d}t \; \mathbf{g}(t)\, e^{i\omega t} \; . \tag{E.1}$$

Although this is different than the convention used in the rest of this dissertation, it matches that used in Ref. [100] and is only off by 2π compared to Ref. [9]. This allows an easier comparison of results.

E.1 Connecting MDCS and classical NLO

I struggled for a long time trying to understand how MDCS works. One of the main causes of this was a fundamental difference in the response function formalism used in MDCS compared to what I have seen in classical (i.e. non-quantum mechanical) nonlinear optics (NLO). Although the connection between the two is known in the literature (see Ref. [100]), this section walks through it in detail with the intent to be helpful for future students.

In MDCS (see e.g. Ref. [100]) the third-order contribution to the polarization density is

$$\mathbf{P}^{(3)}(t) = \int_{-\infty}^{\infty} \mathrm{d}t_3 \int_{-\infty}^{\infty} \mathrm{d}t_2 \int_{-\infty}^{\infty} \mathrm{d}t_1 \; \mathbf{S}^{(3)}(t_1, t_2, t_3) \, | \\ \mathbf{E}(t - t_3 - t_2 - t_1) \, \mathbf{E}(t - t_3 - t_2) \, \mathbf{E}(t - t_3) \quad , \tag{E.2}$$

where it is evident that time-shift invariance is assumed. The spatial dependence of the fields has been dropped for brevity and the vertical bar denotes tensor contraction. Furthermore, $\mathbf{S}^{(3)}(t_1, t_2, t_3) = 0$ for all $t_1, t_2, t_3 < 0$. This is allegedly due to causality – but causality only implies the electric field arguments must be less than t to get a response at t (meaning there is no response unless $t_3 + t_2 + t_1, t_3 + t_2, t_3 > 0$). The tighter constraints arise due to the time-ordered nature of density matrix perturbation theory (which implies there is no response unless $t_3 + t_2 + t_1 > t_3 + t_2 > t_3$).

In classical NLO (see e.g. Ref. [9]) the form for $\mathbf{P}^{(3)}$ is

$$\mathbf{P}^{(3)}(t) = \epsilon_0 \int_{-\infty}^{\infty} \mathrm{d}\tau_3 \int_{-\infty}^{\infty} \mathrm{d}\tau_2 \int_{-\infty}^{\infty} \mathrm{d}\tau_1 \; \mathbf{R}^{(3)}(\tau_1, \tau_2, \tau_3) \, | \\ \mathbf{E}(t - \tau_1) \, \mathbf{E}(t - \tau_2) \, \mathbf{E}(t - \tau_3) \quad , \tag{E.3}$$

where again time-shift invariance is assumed and causality implies $\mathbf{R}^{(3)}(\tau_1, \tau_2, \tau_3) = 0$

for all $\tau_1, \tau_2, \tau_3 < 0$. At first appearance, it seems that simply changing variables in Eq. (E.3) reveals the relationship between $\mathbf{S}^{(3)}$ and $\mathbf{R}^{(3)}$ as

$$\mathbf{S}^{(3)}(t_1, t_2, t_3) \stackrel{?}{=} \epsilon_0 \, \mathbf{R}^{(3)}(t_1 + t_2 + t_3, t_2 + t_3, t_3) \quad . \tag{E.4}$$

However, this relationship is clearly wrong when one considers for example $t_1 < 0$, $t_2 > |t_1|$, and $t_3 = 0$. The left hand side of Eq. (E.4) is identically zero (since $\mathbf{S}^{(3)}$ has a negative argument) while the right hand side is unconstrained.

The fundamental difference between Eqs. (E.2) and (E.3) is that MDCS uses a time-ordered response formalism whereas classical NLO does not. A relationship between the response functions can be found by accounting for this difference. First, $\mathbf{R}^{(3)}$ is split up into six parts corresponding to the six different electric field ordering sequences as

$$\mathbf{R}^{(3)} = \mathbf{R}^{(123)} + \mathbf{R}^{(132)} + \mathbf{R}^{(213)} + \mathbf{R}^{(312)} + \mathbf{R}^{(321)} + \mathbf{R}^{(231)} \quad . \tag{E.5}$$

The time-ordering is enforced in the form of each part. For example,

$$\mathbf{R}^{(123)}(\tau_1, \tau_2, \tau_3) \equiv \mathbf{R}^{(3)}(\tau_1, \tau_2, \tau_3) \, \Theta(\tau_1 - \tau_2) \, \Theta(\tau_2 - \tau_3) \quad , \tag{E.6}$$

where the Heaviside functions along with causality ensure that $\mathbf{R}^{(123)}(\tau_1, \tau_2, \tau_3)$ is zero except when $\tau_1 > \tau_2 > \tau_3 > 0$. This corresponds to the electric field paired with its first time argument being evaluated at the earliest time followed by the electric fields paired with the second and third arguments sequentially. Using the results from the

Math 1 section below, Eq. (E.3) can be rewritten as

$$\mathbf{P}^{(3)}(t) = 6\,\epsilon_0 \int_{-\infty}^{\infty} \mathrm{d}t_3 \int_{-\infty}^{\infty} \mathrm{d}t_2 \int_{-\infty}^{\infty} \mathrm{d}t_1\, \mathbf{R}^{(123)}(t_1 + t_2 + t_3, t_2 + t_3, t_3)\, | \\ \mathbf{E}(t - t_1 - t_2 - t_3)\, \mathbf{E}(t - t_2 - t_3)\, \mathbf{E}(t - t_3) \quad , \tag{E.7}$$

which when compared with Eq. (E.2) identifies the connection between MDCS and NLO as

$$\mathbf{S}^{(3)}(t_1, t_2, t_3) = 6\,\epsilon_0\, \mathbf{R}^{(123)}(t_1 + t_2 + t_3, t_2 + t_3, t_3) \quad . \tag{E.8}$$

Clearly $\mathbf{S}^{(3)}$ is a time-ordered version of $\mathbf{R}^{(3)}$ which stems from the fact that density matrix perturbation theory is inherently time-ordered. Changing variables using $t_1 \to \tau_1 - \tau_2$, $t_2 \to \tau_2 - \tau_3$, and $t_3 \to \tau_3$, reveals that that the total NLO response function is

$$\mathbf{R}^{(3)}(\tau_1, \tau_2, \tau_3) = \frac{1}{6\,\epsilon_0}\, \mathbb{P}\, \mathbf{S}^{(3)}(\tau_1 - \tau_2, \tau_2 - \tau_3, \tau_3) \quad , \tag{E.9}$$

where $\mathbb{P}$ is the index-argument permutation operator defined in the Math 1 section below. Eq. (E.9) can be seen in Ref. [100].

To introduce $\boldsymbol{\chi}^{(3)}$, Eq. (E.9) can be Fourier transformed which results in

$$\boldsymbol{\chi}^{(3)}(\omega_1, \omega_2, \omega_3) = \frac{1}{6\,\epsilon_0}\, \mathbb{P}\, \tilde{\mathbf{S}}^{(3)}(\omega_1, \omega_1 + \omega_2, \omega_1 + \omega_2 + \omega_3) \quad . \tag{E.10}$$

Aside from the factor of ϵ_0 which is purely a matter of convention, this is exactly the result obtained in Eq. 5.43(b) of Ref. [100]. The inverse relationship can be found by Fourier Transforming Eq. (E.8) which reveals

$$\tilde{\mathbf{S}}^{(3)}(\omega_\tau, \omega_T, \omega_t) = 6\,\epsilon_0\, \boldsymbol{\chi}^{(123)}(\omega_\tau, \omega_T - \omega_\tau, \omega_t - \omega_T) \quad , \tag{E.11}$$

where we've defined $\boldsymbol{\chi}^{(123)}$ (a time-ordered piece of $\boldsymbol{\chi}^{(3)}$) as the Fourier transform of $\mathbf{R}^{(123)}$. Using the results of the Math 2 section below, this can be rewritten in terms of $\boldsymbol{\chi}^{(3)}$ as

$$\tilde{\mathbf{S}}^{(3)}(\omega_\tau,\omega_T,\omega_t) = \frac{3\,\epsilon_0}{2}\int_{-\infty}^{\infty}\mathrm{d}\omega_1\int_{-\infty}^{\infty}\mathrm{d}\omega_2\int_{-\infty}^{\infty}\mathrm{d}\omega_3\;\boldsymbol{\chi}^{(3)}(\omega_1,\omega_2,\omega_3)\,\delta(\omega_1+\omega_2+\omega_3-\omega_t)$$
$$\left[\delta(\omega_3-\omega_t+\omega_T)+\frac{i}{\pi}\,\mathcal{P}\frac{1}{\omega_3-\omega_t+\omega_T}\right]$$
$$\left[\delta(\omega_1-\omega_\tau)-\frac{i}{\pi}\,\mathcal{P}\frac{1}{\omega_1-\omega_\tau}\right] \quad , \tag{E.12}$$

where $\mathcal{P}$ denotes the Cauchy principle value. Clearly time-ordering is enforced in a much more complicated way in the frequency-domain when compared to its time-domain counterpart in Eq. (E.6). In practice, it may be simpler to obtain $\tilde{\mathbf{S}}^{(3)}$ by directly Fourier transforming Eq. (E.8).

In summary, $\mathbf{S}^{(3)}$ is proportional to a time-ordered piece of $\mathbf{R}^{(3)}$ which arises from the time-ordered nature of density matrix perturbation theory. One implication is that $\mathbf{S}^{(3)}$ does not possess the intrinsic permutation symmetry that $\mathbf{R}^{(3)}$ and $\boldsymbol{\chi}^{(3)}$ do as indicated by Eqs. (E.6) and (E.8). It may lack other symmetries as well but I have yet to explore them – spatial symmetries may be particularly interesting. Regardless, the relationships developed here should help someone with a classical NLO background to better understand MDCS and vice-versa.

E.2 Math 1 - Time-ordering classical NLO

In index notation, Eq. (E.3) can be written as

$$P_i^{(3)}(t) = \epsilon_0\int_{-\infty}^{\infty}\mathrm{d}\tau_3\int_{-\infty}^{\infty}\mathrm{d}\tau_2\int_{-\infty}^{\infty}\mathrm{d}\tau_1\;R_{ijkl}^{(3)}(\tau_1,\tau_2,\tau_3)\,|$$
$$E_j(t-\tau_1)\,E_k(t-\tau_2)\,E_l(t-\tau_3) \quad , \tag{E.13}$$

using the Einstein summation convention. By inspecting Eq. (E.13) it can be seen that $\mathbf{P}^{(3)}$ is unaltered under any exchange of the index-argument pairs (j,τ_1), (k,τ_2), (l,τ_3) in $\mathbf{R}^{(3)}$. This implies that $\mathbf{R}^{(3)}$ possesses intrinsic permutation symmetry meaning that all of its components generated by swapping its index-argument pairs are equal $(R_{ijkl}(\tau_1,\tau_2,\tau_3) = R_{ijlk}(\tau_1,\tau_3,\tau_2) = \cdots)$.

By inspecting Eq. (E.6) and using the intrinsic permutation symmetry of $\mathbf{R}^{(3)}$, it can be seen that

$$\begin{aligned} R^{(123)}_{ijkl}(\tau_1,\tau_2,\tau_3) &\equiv R^{(3)}_{ijkl}(\tau_1,\tau_2,\tau_3)\,\Theta(\tau_1-\tau_2)\,\Theta(\tau_2-\tau_3) \\ &= R^{(3)}_{ijlk}(\tau_1,\tau_3,\tau_2)\,\Theta(\tau_1-\tau_2)\,\Theta(\tau_2-\tau_3) \\ &= R^{(132)}_{ijlk}(\tau_1,\tau_3,\tau_2) \\ &\;\;\vdots \quad . \end{aligned} \tag{E.14}$$

Note that this means that $\mathbf{R}^{(3)}$ can be written entirely in terms of $\mathbf{R}^{(123)}$ as

$$\begin{aligned} R^{(3)}_{ijkl}(\tau_1,\tau_2,\tau_3) &= R^{(123)}_{ijkl}(\tau_1,\tau_2,\tau_3) + R^{(123)}_{ijlk}(\tau_1,\tau_3,\tau_2) \\ &\quad + R^{(123)}_{ikjl}(\tau_2,\tau_1,\tau_3) + R^{(123)}_{iljk}(\tau_3,\tau_1,\tau_2) \\ &\quad + R^{(123)}_{iklj}(\tau_2,\tau_3,\tau_1) + R^{(123)}_{ilkj}(\tau_3,\tau_2,\tau_1) \\ &= \mathbb{P}\; R^{(123)}_{ijkl}(\tau_j,\tau_k,\tau_l) \quad , \end{aligned} \tag{E.15}$$

where $\mathbb{P}$ is the index-argument permutation operator that sums the operand over all possible permutations of its index-argument pairs (j,τ_1), (k,τ_2), and (l,τ_3). By Fourier transforming this equation, one can see that

$$\boldsymbol{\chi}^{(3)}(\omega_1,\omega_2,\omega_3) = \mathbb{P}\;\boldsymbol{\chi}^{(123)}(\omega_1,\omega_2,\omega_3) \quad , \tag{E.16}$$

where $\boldsymbol{\chi}^{(123)}$ (a time-ordered piece of $\boldsymbol{\chi}^{(3)}$) is defined as the Fourier transform of

$\mathbf{R}^{(123)}$.

The intrinsic permutation symmetry of $\mathbf{R}^{(3)}$ implies that all of the time-ordered responses produce identical polarizations densities. For example, the 132 time-ordered response can be written as

$$P_i^{(132)}(t) = \epsilon_0 \int_{-\infty}^{\infty} \mathrm{d}\tau_3 \int_{-\infty}^{\infty} \mathrm{d}\tau_2 \int_{-\infty}^{\infty} \mathrm{d}\tau_1 \; R_{ijkl}^{(132)}(\tau_1, \tau_2, \tau_3) \, | \\ E_j(t-\tau_1)\, E_k(t-\tau_2)\, E_l(t-\tau_3) \quad . \tag{E.17}$$

Using Eq. (E.14), this can be rewritten as

$$\begin{aligned} P_i^{(132)}(t) &= \epsilon_0 \int_{-\infty}^{\infty} \mathrm{d}\tau_3 \int_{-\infty}^{\infty} \mathrm{d}\tau_2 \int_{-\infty}^{\infty} \mathrm{d}\tau_1 \; R_{ijlk}^{(123)}(\tau_1, \tau_3, \tau_2) \, | \\ &\quad E_j(t-\tau_1)\, E_k(t-\tau_2)\, E_l(t-\tau_3) \\ &= \epsilon_0 \int_{-\infty}^{\infty} \mathrm{d}\tau_2 \int_{-\infty}^{\infty} \mathrm{d}\tau_3 \int_{-\infty}^{\infty} \mathrm{d}\tau_1 \; R_{ijkl}^{(123)}(\tau_1, \tau_2, \tau_3) \, | \\ &\quad E_j(t-\tau_1)\, E_l(t-\tau_3)\, E_k(t-\tau_2) \\ &= P_i^{(123)}(\mathbf{r}, t) \quad , \end{aligned} \tag{E.18}$$

where in the middle step we changed dummy variables $\tau_2 \leftrightarrow \tau_3$ and indices $k \leftrightarrow l$. So the total third-order polarization density is

$$\mathbf{P}^{(3)}(t) = 6\, \mathbf{P}^{(123)}(t) \quad . \tag{E.19}$$

Eq. (E.7) is found by changing variables using $\tau_1 \to t_1 + t_2 + t_3$, $\tau_2 \to t_2 + t_3$, and $\tau_3 \to t_3$.

E.3 Math 2 - Time-ordered susceptibility

The time-ordered susceptibility $\boldsymbol{\chi}^{(123)}$ is defined as the Fourier transform of $\mathbf{R}^{(123)}$. So,

$$\begin{aligned}
\boldsymbol{\chi}^{(123)}(\omega_1,\omega_2,\omega_3) &\equiv \int_{-\infty}^{\infty} \mathrm{d}\tau_1 \int_{-\infty}^{\infty} \mathrm{d}\tau_2 \int_{-\infty}^{\infty} \mathrm{d}\tau_3\; \mathbf{R}^{(123)}(\tau_1,\tau_2,\tau_3)\; e^{i(\omega_1\tau_1+\omega_2\tau_2+\omega_3\tau_3)} \\
&= \int_{-\infty}^{\infty} \mathrm{d}\tau_1 \int_{-\infty}^{\infty} \mathrm{d}\tau_2 \int_{-\infty}^{\infty} \mathrm{d}\tau_3\; \mathbf{R}^{(3)}(\tau_1,\tau_2,\tau_3)\,\Theta(\tau_1-\tau_2)\,\Theta(\tau_2-\tau_3) \\
&\quad e^{i(\omega_1\tau_1+\omega_2\tau_2+\omega_3\tau_3)} \\
&= \frac{1}{(2\pi)^3} \int_{-\infty}^{\infty} \mathrm{d}\omega_1' \int_{-\infty}^{\infty} \mathrm{d}\omega_2' \int_{-\infty}^{\infty} \mathrm{d}\omega_3'\; \boldsymbol{\chi}^{(3)}(\omega_1',\omega_2',\omega_3') \int_{-\infty}^{\infty} \mathrm{d}\tau_3 \int_{-\infty}^{\infty} \mathrm{d}\tau_2 \int_{-\infty}^{\infty} \mathrm{d}\tau_1 \\
&\quad \Theta(\tau_1-\tau_2)\,\Theta(\tau_2-\tau_3)\, e^{i[(\omega_1-\omega_1')\tau_1+(\omega_2-\omega_2')\tau_2+(\omega_3-\omega_3')\tau_3]} \quad . \qquad \text{(E.20)}
\end{aligned}$$

The time integrals are Fourier transforms of Heaviside functions which are given by

$$\frac{1}{2\pi} \int_{-\infty}^{\infty} \mathrm{d}\tau\; \Theta(\tau)\, e^{i\omega\tau} = \frac{1}{2}\left[\delta(\omega) + \frac{i}{\pi}\,\mathcal{P}\frac{1}{\omega}\right] \quad . \qquad \text{(E.21)}$$

which can be derived using the Sokhotski-Plemelj theorem. A more appropriate form is found by changing integration variables $\tau \to \tau - \tau_0$ or $\tau \to \tau_0 - \tau$ giving

$$\frac{1}{2\pi} \int_{-\infty}^{\infty} \mathrm{d}\tau\; \Theta(\pm\tau \mp \tau_0)\, e^{i\omega\tau} = \frac{1}{2}\, e^{i\omega\tau_0}\left[\delta(\omega) \pm \frac{i}{\pi}\,\mathcal{P}\frac{1}{\omega}\right] \quad , \qquad \text{(E.22)}$$

and to substitute $\omega \to \omega - \omega'$ giving

$$\frac{1}{2\pi} \int_{-\infty}^{\infty} \mathrm{d}\tau\; \Theta(\pm\tau \mp \tau_0)\, e^{i(\omega-\omega')\tau} = \frac{1}{2}\, e^{i(\omega-\omega')\tau_0}\left[\delta(\omega'-\omega) \mp \frac{i}{\pi}\,\mathcal{P}\frac{1}{\omega'-\omega}\right] \quad . \qquad \text{(E.23)}$$

Using this formula we find that

$$\begin{aligned}\boldsymbol{\chi}^{(123)}(\omega_1,\omega_2,\omega_3) &= \frac{1}{8\pi}\int_{-\infty}^{\infty}\mathrm{d}\omega_1'\int_{-\infty}^{\infty}\mathrm{d}\omega_2'\int_{-\infty}^{\infty}\mathrm{d}\omega_3'\,\boldsymbol{\chi}^{(3)}(\omega_1',\omega_2',\omega_3') \\ &\quad\left[\delta(\omega_1'-\omega_1)-\frac{i}{\pi}\mathcal{P}\frac{1}{\omega_1'-\omega_1}\right]\left[\delta(\omega_3'-\omega_3)+\frac{i}{\pi}\mathcal{P}\frac{1}{\omega_3'-\omega_3}\right] \\ &\quad\int_{-\infty}^{\infty}\mathrm{d}\tau_2\,e^{i[(\omega_1-\omega_1'+\omega_2-\omega_2'+\omega_3-\omega_3')\tau_2]} \\ &= \frac{1}{4}\int_{-\infty}^{\infty}\mathrm{d}\omega_1'\int_{-\infty}^{\infty}\mathrm{d}\omega_2'\int_{-\infty}^{\infty}\mathrm{d}\omega_3'\,\boldsymbol{\chi}^{(3)}(\omega_1',\omega_2',\omega_3') \\ &\quad\left[\delta(\omega_1'-\omega_1)-\frac{i}{\pi}\mathcal{P}\frac{1}{\omega_1'-\omega_1}\right]\left[\delta(\omega_3'-\omega_3)+\frac{i}{\pi}\mathcal{P}\frac{1}{\omega_3'-\omega_3}\right] \\ &\quad\delta(\omega_1'+\omega_2'+\omega_3'-\omega_1-\omega_2-\omega_3)\quad . \end{aligned} \tag{E.24}$$

E.4 Nonlinear FTS

MDCS is a FWM technique and pumps a sample using a sequence of three typically ultrafast pulses cartooned in Fig. E.1. In this work, a fourth pulse is used to read the emitted FWM signal via heterodyne detection.

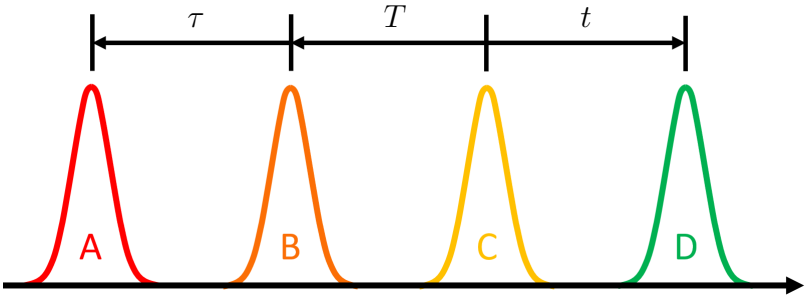

Figure E.1: Pulse sequence and temporal delays used in MDCS. Pulses A, B, and C, pump the system while pulse D "reads-out" the emitted signal similar to asymmetric or dispersive FTS.

Ignoring finite pulse duration effects and using the sequence in Fig. E.1 the FWM

polarization that depends on pulses A, B, and C, is

$$\mathbf{P}^{(3)}(t;\tau,T) = \int_{-\infty}^{\infty} \mathrm{d}t_3 \int_{-\infty}^{\infty} \mathrm{d}t_2 \int_{-\infty}^{\infty} \mathrm{d}t_1 \; \mathbf{S}^{(3)}(t_1,t_2,t_3) \, | \\ \mathbf{E}_{\mathrm{A}}(t-t_3-t_2-t_1;\tau,T) \, \mathbf{E}_{\mathrm{B}}(t-t_3-t_2;T) \, \mathbf{E}_{\mathrm{C}}(t-t_3) \; , \tag{E.25}$$

as given by Eq. (E.2). Pulse D is used to measure something (for example a radiated field from the polarization) that allows one to determine $\mathbf{P}^{(3)}(t;\tau,T)$ using an FTS approach. The math would be similar to Appx. B so it will skipped here. Technically, this would require some back propagation using Maxwell's equations but this is rarely done in practice as long as the optical density of the sample is sufficiently low [163–166]. Essentially, by scanning the t delay one can sample $\mathbf{P}^{(3)}(t;\tau,T)$ in a way similar to FTS so the left-hand side of Eq. (E.25) is for all practical purposes "measured" for a given t and τ. In the frequency-domain (specifically with respect to t) Eq. (E.25) becomes

$$\tilde{\mathbf{P}}^{(3)}(\omega_t;\tau,T) = \int_{-\infty}^{\infty} \mathrm{d}\omega_1 \int_{-\infty}^{\infty} \mathrm{d}\omega_2 \int_{-\infty}^{\infty} \mathrm{d}\omega_3 \; \tilde{\mathbf{S}}^{(3)}(\omega_1,\omega_1+\omega_2,\omega_1+\omega_2+\omega_3) \, | \\ \tilde{\mathbf{E}}_{\mathrm{A}}(\omega_1;\tau,T) \, \tilde{\mathbf{E}}_{\mathrm{B}}(\omega_2;T) \, \tilde{\mathbf{E}}_{\mathrm{C}}(\omega_3) \, \delta(\omega_t-\omega_1-\omega_2-\omega_3) \; , \tag{E.26}$$

where we've made use of the Fourier shift theorem (see Chap. II but mind the change in Fourier convention) three times and defined

$$\tilde{\mathbf{S}}(\omega_1,\omega_2,\omega_3) \equiv \int_{-\infty}^{\infty} \mathrm{d}t_3 \int_{-\infty}^{\infty} \mathrm{d}t_2 \int_{-\infty}^{\infty} \mathrm{d}t_1 \; \mathbf{S}^{(3)}(t_1,t_2,t_3) e^{i(\omega_1 t_1+\omega_2 t_2+\omega_3 t_3)} \; . \tag{E.27}$$

The remaining time-delays manifest as phase ramps in the frequency-domain since $\mathbf{E}_{\mathrm{A}}(t;\tau,T) = \mathbf{E}_{\mathrm{A}}(t-\tau-T;0)$ and $\mathbf{E}_{\mathrm{B}}(t;\tau) = \mathbf{E}_{\mathrm{B}}(t-\tau;0)$ (again see Fourier shift

theorem in Chap. II and again mind the change in Fourier convention) so

$$\tilde{\mathbf{P}}^{(3)}(\omega_t;\tau,T) = \int_{-\infty}^{\infty} \mathrm{d}\omega_1 \int_{-\infty}^{\infty} \mathrm{d}\omega_2 \int_{-\infty}^{\infty} \mathrm{d}\omega_3 \; \tilde{\mathbf{S}}^{(3)}(\omega_1, \omega_1+\omega_2, \omega_1+\omega_2+\omega_3) \,|\, e^{i\omega_1(\tau+T)} e^{i\omega_2 T} \\ \tilde{\mathbf{E}}_{\mathrm{A}}(\omega_1;\tau,T)\, \tilde{\mathbf{E}}_{\mathrm{B}}(\omega_2;T)\, \tilde{\mathbf{E}}_{\mathrm{C}}(\omega_3)\, \delta(\omega_t - \omega_1 - \omega_2 - \omega_3) \;, \tag{E.28}$$

The goal of MDCS is to measure $\mathbf{S}^{(3)}$, but, analogous to FTS, it is impossible to directly invert the above equation even if all the fields are known. However, if data is collected for many different τ and T then one can Fourier transform over τ and T (the assumption of a pulse ordering sequence of ABC assumes that the response is $\tilde{\mathbf{P}}^{(3)} = \mathbf{0}$ for $\tau, T > 0$ – in practice this is where finite duration pulse effects occur [167]). This introduces super-handy delta functions just like in FTS on the right-hand side,

$$\tilde{\mathbf{P}}^{(3)}(\omega_t;\omega_\tau,\omega_T) = \int_{-\infty}^{\infty} \mathrm{d}\omega_1 \int_{-\infty}^{\infty} \mathrm{d}\omega_2 \int_{-\infty}^{\infty} \mathrm{d}\omega_3 \; \tilde{\mathbf{S}}^{(3)}(\omega_1, \omega_1+\omega_2, \omega_1+\omega_2+\omega_3) \,| \\ \delta(\omega_\tau - \omega_1)\delta(\omega_T - \omega_1 - \omega_2)\delta(\omega_t - \omega_1 - \omega_2 - \omega_3) \\ \tilde{\mathbf{E}}_{\mathrm{A}}(\omega_1;0,0)\, \tilde{\mathbf{E}}_{\mathrm{B}}(\omega_2;0)\, \tilde{\mathbf{E}}_{\mathrm{C}}(\omega_3) \\ = \tilde{\mathbf{S}}^{(3)}(\omega_\tau,\omega_T,\omega_t) \,|\, \tilde{\mathbf{E}}_{\mathrm{A}}(\omega_\tau;0,0)\, \tilde{\mathbf{E}}_{\mathrm{B}}(\omega_T-\omega_\tau;0)\, \tilde{\mathbf{E}}_{\mathrm{C}}(\omega_t-\omega_T) \;, \tag{E.29}$$

and leaves us with a simple algebraic equation for $\mathbf{S}^{(3)}$ (the components that can be solved for depend on the polarization of the pump pulses). Note that the last delta function on the second line (which is a statement of energy conservation in the fields required by time-shift invariance) implies that for ω_t to be a similar optical frequency to that of the pump fields one of ω_1, ω_2, or ω_3 must have a different sign from the others. A field associated with a negative frequency is called a conjugated field because in the analytic representation, negative frequencies only occur when

a field is conjugated. These conjugated pulses cause the sample to respond with a frequency evolution opposite to that of a non-conjugated pulse as shown in Fig. E.2. Note that any physical pulse in the lab (which has real-valued fields) can cause both conjugated and non-conjugated evolution. However, it is common to describe these physical pulses as conjugated or not because most experimental techniques are only sensitive to a single prescribed quantum pathway (e.g. $\mathbf{S}_{\mathrm{I}}$ - see below) even though in reality all pathways are realized. In principle, it is possible to measure multiple quantum pathways simultaneously – this could, for example, be achieved DTCS (see Chap. VII).

The order of conjugation is associated with different quantum evolution pathways as described by density matrix perturbation theory [100]. As such, $\mathbf{S}^{(3)}$ is broken spectrally into three parts corresponding to the three possible choices for which pulse is conjugated [164]: for a conjugated first (or second and third) pulse(s)

$$\begin{aligned}\mathbf{S}_{\mathrm{I}}(\omega_\tau,\omega_T,\omega_t) \equiv \mathbf{S}^{(3)}(\omega_\tau,\omega_T,\omega_t)\Big[&\Theta(-\omega_\tau)\,\Theta(\omega_T-\omega_\tau)\,\Theta(\omega_t-\omega_T)\\ &+\Theta(\omega_\tau)\,\Theta(-\omega_T+\omega_\tau)\,\Theta(-\omega_t+\omega_T)\Big]\,,\end{aligned} \tag{E.30}$$

for a conjugated second (or first and third) pulse(s)

$$\begin{aligned}\mathbf{S}_{\mathrm{II}}(\omega_\tau,\omega_T,\omega_t) \equiv \mathbf{S}^{(3)}(\omega_\tau,\omega_T,\omega_t)\Big[&\Theta(\omega_\tau)\,\Theta(-\omega_T+\omega_\tau)\,\Theta(\omega_t-\omega_T)\\ &+\Theta(-\omega_\tau)\,\Theta(\omega_T-\omega_\tau)\,\Theta(-\omega_t+\omega_T)\Big]\,,\end{aligned} \tag{E.31}$$

and for a conjugated third (or first and second) pulse(s)

$$\begin{aligned}\mathbf{S}_{\mathrm{III}}(\omega_\tau,\omega_T,\omega_t) \equiv \mathbf{S}^{(3)}(\omega_\tau,\omega_T,\omega_t)\Big[&\Theta(\omega_\tau)\,\Theta(\omega_T-\omega_\tau)\,\Theta(-\omega_t+\omega_T)\\ &+\Theta(-\omega_\tau)\,\Theta(-\omega_T+\omega_\tau)\,\Theta(\omega_t-\omega_T)\Big]\,.\end{aligned} \tag{E.32}$$

If no pulses are conjugated them ω_t is a large optical frequency (like a third harmonic of the pump frequency) and the "triple quantum" response function is

$$\mathbf{S}_{\mathrm{IV}}(\omega_\tau, \omega_T, \omega_t) \equiv \mathbf{S}^{(3)}(\omega_\tau, \omega_T, \omega_t) \Big[\Theta(\omega_\tau)\, \Theta(\omega_T - \omega_\tau)\, \Theta(\omega_t - \omega_T) + \Theta(-\omega_\tau)\, \Theta(-\omega_T + \omega_\tau)\, \Theta(-\omega_t + \omega_T) \Big] \quad . \tag{E.33}$$

In practice, scanning both t, τ, and T (sometimes called measuring the "full Hamiltonian") is rarely done because usually a shorter scan will contain the desired information. In this case, one of τ or T is held fixed and a projection of $\mathbf{S}^{(3)}$ onto some plane weighted by the pump fields is obtained. Combined with the fact that at least one pump pulse must be conjugated there are six possible types of measurement, two of which are redundant (see Fig. E.2).

In this work, only the rephasing sequence is used which is now described in detail. Pulse A (which is conjugated) creates a single quantum coherence between the ground state and one of the excited states. Pulse B (not conjugated) converts that coherence into a population of the same excited state. If the laser bandwidth is sufficiently large it may instead create a zero quantum coherence between the same excited state and a different excited state. Pulse C (not conjugated) then converts either of these possibilities into a single quantum coherence with a state near ground energy. This single quantum coherence then radiates a FWM photon taking the system into a low-energy population or zero quantum coherence. If the sample is inhomogeneously broadened, the individual subsystems (which all started out in phase with each other immediately after pulse A) all return to the same phase (i.e. re-phase with each other, hence the name rephasing sequence) a time τ after pulse C leading to a delayed burst of light called a photon echo. This signal is then heterodyned with a local oscillator on a photodetector. In this work, T is held fixed. Fig. E.3 depicts the photon echo in the time (τ-t) and frequency domains.

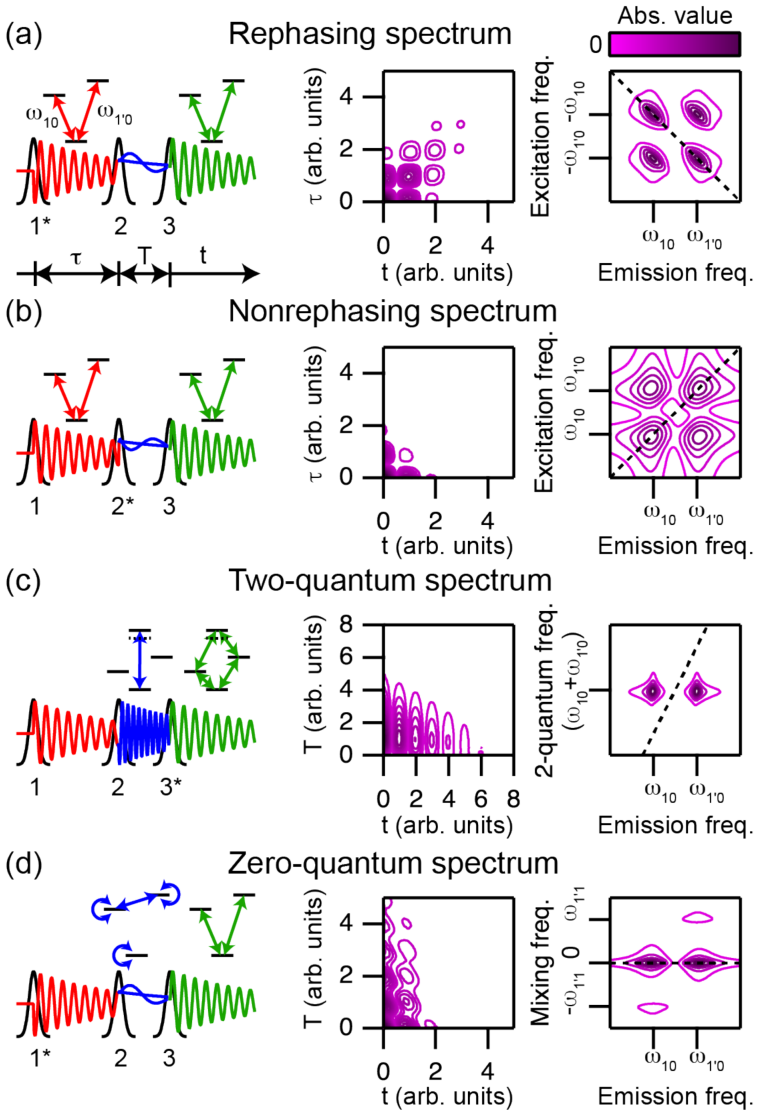

Figure E.2: Four types of MDCS measurement that fix one delay and have one conjugated pulse. On the left-hand sides are the pulse sequences and energy level diagrams to depict the evolution of the polarization. Pulses 1, 2, and 3 are pulses A, B, and C respectively. The plots are the absolute value of FWM signal for the appropriate quantum pathway in temporal and frequency domains. See Ref. [100] for detailed information. Figure credit: Chris Smallwood.

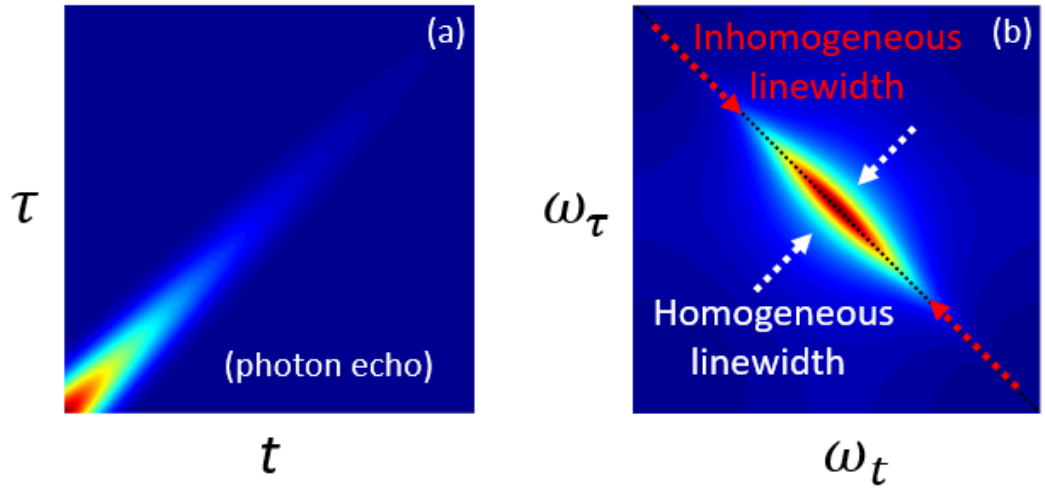

Figure E.3: Cartoon of a photon echo for an inhomogeneous ensemble of two-level systems. (a) τ-t domain (time-time plot). (b) ω_τ-ω_t domain ("2D plot") revealing the homogeneous and inhomogeneous linewidths.

BIBLIOGRAPHY

[1] B. C. Smith, J. F. Whitaker, and S. C. Rand, "Steerable THz pulses from thin emitters via optical pulse-front tilt," Opt. Express **24**, 20755–20762 (2016).

[2] B. C. Smith, J. F. Whitaker, and S. C. Rand, "The steering of THz pulses using thin emitters excited by tilted optical pulse-fronts," Frontiers in Optics 2016 p. FF3F.4 (2016).

[3] B. C. Smith and J. F. Whitaker, "Complete wavefront control of single-cycle THz pulses via optical pulse envelope manipulation," Conference on Lasers and Electro-Optics p. SM1J.6 (2017).

[4] A. Klee, J. Davila-Rodriguez, C. Williams, and P. Delfyett, "Characterization of semiconductor-based optical frequency comb sources using generalized multiheterodyne detection," IEEE J. Sel. Top. Quantum Electron. **19** (2013).

[5] G. B. Rieker, F. R. Giorgetta, W. C. Swann, J. Kofler, A. M. Zolot, L. C. Sinclair, E. Baumann, C. Cromer, G. Petron, C. Sweeney, P. P. Tans, I. Coddington, and N. R. Newbury, "Frequency-comb-based remote sensing of greenhouse gases over kilometer air paths," Optica **1**, 290–298 (2014).

[6] M. Ediger, G. Bester, A. Badolato, P. M. Petroff, K. Karrai, A. Zunger, and R. J. Warburton, "Peculiar many-body effects revealed in the spectroscopy of highly charged quantum dots," Nature Physics **3**, 774 (2007).

[7] J. D. Jackson, *Classical electrodynamics* (Wiley, New York, NY, 1998), 3rd ed.

[8] R. W. Boyd, *Nonlinear Optics* (Academic Press, Burlington, 2008), 3rd ed.

[9] P. N. Butcher and D. Cotter, *The Elements of Nonlinear Optics* (Cambridge University Press, Cambridge, 1990).

[10] A. E. Siegman, *Lasers* (University Science Books, Mill Valley, CA, 1986).

[11] S. P. Davis, M. C. Abrams, and J. W. Brault, *Fourier Transform Spectrometry* (Academic Press, Cambridge, 2001), 1st ed.

[12] I. Coddington, N. Newbury, and W. Swann, "Dual-comb spectroscopy," Optica **3**, 414 (2016).

[13] S. Coburn, C. B. Alden, R. Wright, K. Cossel, E. Baumann, G.-W. Truong, F. Giorgetta, C. Sweeney, N. R. Newbury, K. Prasad, I. Coddington, and G. B. Rieker, "Regional trace-gas source attribution using a field-deployed dual frequency comb spectrometer," Optica **5**, 320–327 (2018).

[14] T. J. Kippenberg, R. Holzwarth, and S. A. Diddams, "Microresonator-based optical frequency combs," Science **332**, 555–559 (2011).

[15] M.-G. Suh, Q.-F. Yang, K. Y. Yang, X. Yi, and K. J. Vahala, "Microresonator soliton dual-comb spectroscopy," Science **354**, 600–603 (2016).

[16] K. J. Mohler, B. J. Bohn, M. Yan, G. Mélen, T. W. Hänsch, and N. Picqué, "Dual-comb coherent Raman spectroscopy with lasers of 1-GHz pulse repetition frequency," Opt. Lett. **42**, 318–321 (2017).

[17] R. Teets, J. Eckstein, and T. W. Hänsch, "Coherent two-photon excitation by multiple light pulses," Phys. Rev. Lett. **38**, 760–764 (1977).

[18] J. N. Eckstein, A. I. Ferguson, and T. W. Hänsch, "High-resolution two-photon spectroscopy with picosecond light pulses," Phys. Rev. Lett. **40**, 847–850 (1978).

[19] S. T. Cundiff and J. Ye, "Colloquium: Femtosecond optical frequency combs," Rev. Mod. Phys. **75**, 325–342 (2003).

[20] S. A. Diddams, "The evolving optical frequency comb [Invited]," J. Opt. Soc. Am. B **27**, B51–B62 (2010).

[21] D. J. Jones, S. A. Diddams, J. K. Ranka, A. Stentz, R. S. Windeler, J. L. Hall, and S. T. Cundiff, "Carrier-envelope phase control of femtosecond mode-locked lasers and direct optical frequency synthesis," Science **288**, 635–639 (2000).

[22] A. Baltuska, T. Udem, M. Uiberacker, M. Hentschel, E. Goulielmakis, C. Gohle, R. Holzwarth, V. S. Yakovlev, A. Scrinzi, T. W. Hänsch, and F. Krausz, "Attosecond control of electronic processes by intense light fields," Nature **421**, 611 (2003).

[23] R. J. Jones, K. D. Moll, M. J. Thorpe, and J. Ye, "Phase-coherent frequency combs in the vacuum ultraviolet via high-harmonic generation inside a femtosecond enhancement cavity," Phys. Rev. Lett. **94**, 193201 (2005).

[24] M. Kourogi, K. Nakagawa, and M. Ohtsu, "Wide-span optical frequency comb generator for accurate optical frequency difference measurement," IEEE Journal of Quantum Electronics **29**, 2693–2701 (1993).

[25] A. J. Metcalf, V. Torres-Company, D. E. Leaird, and A. M. Weiner, "High-power broadly tunable electrooptic frequency comb generator," IEEE Journal of Selected Topics in Quantum Electronics **19**, 231–236 (2013).

[26] H. G. de Chatellus, L. R. Cortés, and J. Azaña, "Arbitrary energy-preserving control of the line spacing of an optical frequency comb over six orders of magnitude through self-imaging," Opt. Express **26**, 21069–21085 (2018).

[27] T. F. S. Büttner, I. V. Kabakova, D. D. Hudson, R. Pant, C. G. Poulton, A. C. Judge, and B. J. Eggleton, "Phase-locking and pulse generation in multi-frequency brillouin oscillator via four wave mixing," Scientific Reports **4**, 5032 (2014).

[28] T. Yasui, S. Yokoyama, H. Inaba, K. Minoshima, T. Nagatsuma, and T. Araki, "Terahertz frequency metrology based on frequency comb," IEEE Journal of Selected Topics in Quantum Electronics **17**, 191–201 (2011).

[29] F. C. Cruz, D. L. Maser, T. Johnson, G. Ycas, A. Klose, F. R. Giorgetta, I. Coddington, and S. A. Diddams, "Mid-infrared optical frequency combs based on difference frequency generation for molecular spectroscopy," Opt. Express **23**, 26814–26824 (2015).

[30] L. F. Tiemeijer, P. I. Kuindersma, P. J. A. Thijs, and G. L. J. Rikken, "Passive FM locking in InGaAsP semiconductor lasers," IEEE Journal of Quantum Electronics **25**, 1385–1392 (1989).

[31] M. Dong, S. T. Cundiff, and H. G. Winful, "Physics of frequency-modulated comb generation in quantum-well diode lasers," Phys. Rev. A **97**, 053822 (2018).

[32] A. Hugi, G. Villares, S. Blaser, H. C. Liu, and J. Faist, "Mid-infrared frequency comb based on a quantum cascade laser," Nature **492**, 229 (2012).

[33] A. Schliesser, M. Brehm, F. Keilmann, and D. W. van der Weide, "Frequency-comb infrared spectrometer for rapid, remote chemical sensing," Opt. Express **13**, 9029–9038 (2005).

[34] P. Trocha, M. Karpov, D. Ganin, M. H. P. Pfeiffer, A. Kordts, S. Wolf, J. Krockenberger, P. Marin-Palomo, C. Weimann, S. Randel, W. Freude, T. J. Kippenberg, and C. Koos, "Ultrafast optical ranging using microresonator soliton frequency combs," Science **359**, 887–891 (2018).

[35] S. T. Cundiff and A. M. Weiner, "Optical arbitrary waveform generation," Nature Photonics **4**, 760 (2010).

[36] G. G. Ycas, F. Quinlan, S. A. Diddams, S. Osterman, S. Mahadevan, S. Redman, R. Terrien, L. Ramsey, C. F. Bender, B. Botzer, and S. Sigurdsson, "Demonstration of on-sky calibration of astronomical spectra using a 25 GHz near-IR laser frequency comb," Opt. Express **20**, 6631–6643 (2012).

[37] M. C. Stowe, M. J. Thorpe, A. Pe'er, J. Ye, J. E. Stalnaker, V. Gerginov, and S. A. Diddams, *Direct frequency comb spectroscopy*, vol. 55 of *Advances In Atomic, Molecular, and Optical Physics* (Academic Press, 2008).

[38] A. D. Ludlow, M. M. Boyd, J. Ye, E. Peik, and P. O. Schmidt, "Optical atomic clocks," Rev. Mod. Phys. **87**, 637–701 (2015).

[39] J. Grotti, S. Koller, S. Vogt, S. Häfner, U. Sterr, C. Lisdat, H. Denker, C. Voigt, L. Timmen, A. Rolland, F. N. Baynes, H. S. Margolis, M. Zampaolo, P. Thoumany, M. Pizzocaro, B. Rauf, F. Bregolin, A. Tampellini, P. Barbieri, M. Zucco, G. A. Costanzo, C. Clivati, F. Levi, and D. Calonico, "Geodesy and metrology with a transportable optical clock," Nature Physics **14**, 437–441 (2018).

[40] R. M. Godun, P. B. R. Nisbet-Jones, J. M. Jones, S. A. King, L. A. M. Johnson, H. S. Margolis, K. Szymaniec, S. N. Lea, K. Bongs, and P. Gill, "Frequency ratio of two optical clock transitions in $^{171}Yb^{+}$ and constraints on the time variation of fundamental constants," Phys. Rev. Lett. **113**, 210801 (2014).

[41] S. Kolkowitz, I. Pikovski, N. Langellier, M. D. Lukin, R. L. Walsworth, and J. Ye, "Gravitational wave detection with optical lattice atomic clocks," Phys. Rev. D **94**, 124043 (2016).

[42] B. Zhang, D. F. Gardner, M. H. Seaberg, E. R. Shanblatt, C. L. Porter, R. Karl, C. A. Mancuso, H. C. Kapteyn, M. M. Murnane, and D. E. Adams, "Ptychographic hyperspectral spectromicroscopy with an extreme ultraviolet high harmonic comb," Opt. Express **24**, 18745–18754 (2016).

[43] C. J. Campbell, A. G. Radnaev, A. Kuzmich, V. A. Dzuba, V. V. Flambaum, and A. Derevianko, "Single-ion nuclear clock for metrology at the 19th decimal place," Phys. Rev. Lett. **108**, 120802 (2012).

[44] C. Wagner and N. Harned, "Lithography gets extreme," Nature Photonics **4**, 24 (2010).

[45] T. Ideguchi, "Dual-Comb Spectroscopy," Opt. Photon. News **28**, 32–39 (2017).

[46] N. R. Newbury, I. Coddington, and W. Swann, "Sensitivity of coherent dual-comb spectroscopy," Opt. Express **18**, 7929–7945 (2010).

[47] B. Bernhardt, A. Ozawa, P. Jacquet, M. Jacquey, Y. Kobayashi, T. Udem, R. Holzwarth, G. Guelachvili, T. W. Hänsch, and N. Picqué, "Cavity-enhanced dual-comb spectroscopy," Nat. Photonics **4**, 55–57 (2010).

[48] I. Coddington, W. C. Swann, and N. R. Newbury, "Coherent dual-comb spectroscopy at high signal-to-noise ratio," Phys. Rev. A **82**, 043817 (2010).

[49] G. Millot, S. Pitois, M. Yan, T. Hovhannisyan, A. Bendahmane, T. W. Hänsch, and N. Picqué, "Frequency-agile dual-comb spectroscopy," Nat. Photonics **10**, 27–30 (2015).

[50] A. Nishiyama, S. Yoshida, T. Hariki, Y. Nakajima, and K. Minoshima, "Sensitivity improvement of dual-comb spectroscopy using mode-filtering technique," Opt. Express **25**, 31730–31738 (2017).

[51] M. A. Duguay and J. W. Hansen, "Optical sampling of subnanosecond light pulses," Appl. Phys. Lett. **13**, 178–180 (1968).

[52] J. Davila-Rodriguez, M. Bagnell, C. Williams, and P. J. Delfyett, "Multiheterodyne detection for spectral compression and downconversion of arbitrary periodic optical signals," J. Lightwave Technol. **29**, 3091–3098 (2011).

[53] N. B. Hébert, S. Boudreau, J. Genest, and J.-D. Deschênes, "Coherent dual-comb interferometry with quasi-integer-ratio repetition rates," Opt. Express **22**, 29152–29160 (2014).

[54] L. Antonucci, X. Solinas, A. Bonvalet, and M. Joffre, "Asynchronous optical sampling with arbitrary detuning between laser repetition rates," Opt. Express **20**, 17928 (2012).

[55] K. Kikuchi, "Coherent Detection of Phase-Shift Keying Signals Using Digital Carrier-Phase Estimation," J. Light. Technol. **24**, 12–21 (2006).

[56] I. Coddington, F. R. Giorgetta, E. Baumann, W. C. Swann, and N. R. Newbury, "Characterizing fast arbitrary cw waveforms with 1500 THz/s instantaneous chirps," IEEE J. Sel. Top. Quantum Electron. **18**, 228–238 (2012).

[57] E. Baumann, F. R. Giorgetta, W. C. Swann, A. M. Zolot, I. Coddington, and N. R. Newburry, "Spectroscopy of the Methane ν_3 Band with an Accurate Mid-Infrared Coherent Dual- Comb Spectrometer," Phys. Rev. A **84**, 062513 (2011).

[58] Y.-D. Hsieh, Y. Iyonaga, Y. Sakaguchi, S. Yokoyama, H. Inaba, K. Minoshima, F. Hindle, T. Araki, and T. Yasui, "Spectrally interleaved, comb-mode-resolved spectroscopy using swept dual terahertz combs," Sci. Rep. **4**, 1–7 (2014).

[59] T. Ideguchi, S. Holzner, B. Bernhardt, G. Guelachvili, N. Picqué, and T. W. Hänsch, "Coherent raman spectro-imaging with laser frequency combs," Nature **502**, 355 (2013).

[60] B. Lomsadze and S. T. Cundiff, "Frequency comb-based four-wave-mixing spectroscopy," Opt. Lett. **42**, 2346–2349 (2017).

[61] B. Lomsadze and S. T. Cundiff, "Frequency combs enable rapid and high-resolution multidimensional coherent spectroscopy," Science **357**, 1389–1391 (2017).

[62] B. Lomsadze and S. T. Cundiff, "Multi-heterodyne two dimensional coherent spectroscopy using frequency combs," Scientific Reports **7**, 14018 (2017).

[63] A. Asahara and K. Minoshima, "Development of ultrafast time-resolved dual-comb spectroscopy," APL Photonics **2**, 041301 (2017).

[64] J.-D. Deschênes and J. Genest, "Heterodyne beats between a continuous-wave laser and a frequency comb beyond the shot-noise limit of a single comb mode," Phys. Rev. A **87**, 023802 (2013).

[65] T. O'Haver, *A Pragmatic Introduction to Signal Processing: with applications in scientific measurement* (CreateSpace Independent Publishing Platform, 2016), 2nd ed.

[66] J. Chen, J. W. Sickler, P. Fendel, E. P. Ippen, F. X. Kärtner, T. Wilken, R. Holzwarth, and T. W. Hänsch, "Generation of low-timing-jitter femtosecond pulse trains with 2 GHz repetition rate via external repetition rate multiplication," Opt. Lett. **33**, 959–961 (2008).

[67] M. S. Kirchner, D. A. Braje, T. M. Fortier, A. M. Weiner, L. Hollberg, and S. A. Diddams, "Generation of 20 GHz, sub-40 fs pulses at 960 nm via repetition-rate multiplication," Opt. Lett. **34**, 872–874 (2009).

[68] L. Yang, H. Yang, H. Zhang, H. Wei, and Y. Li, "Repetition rate multiplication of frequency comb using all-pass fiber resonator," Review of Scientific Instruments **87**, 093101 (2016).

[69] B. Stern, X. Ji, Y. Okawachi, A. L. Gaeta, and M. Lipson, "Battery-operated integrated frequency comb generator," Nature **562**, 401–405 (2018).

[70] K. Sato, "Optical pulse generation using fabry-perot lasers under continuous-wave operation," IEEE Journal of Selected Topics in Quantum Electronics **9**, 1288–1293 (2003).

[71] D. Burghoff, Y. Yang, and Q. Hu, "Computational multiheterodyne spectroscopy," Science Advances **2** (2016).

[72] Q. Li, X. He, Y. Wang, H. Liu, D. Xu, and F. Guo, "Review of spectral imaging technology in biomedical engineering: achievements and challenges," Journal of Biomedical Optics **18** (2013).

[73] E. Bauriegel and W. B. Herppich, "Hyperspectral and Chlorophyll Fluorescence Imaging for Early Detection of Plant Diseases, with Special Reference to Fusarium spec. Infections on Wheat," Agriculture **4**, 32–57 (2014).

[74] D.-W. Sun, *Hyperspectral Imaging for Food Quality Analysis and Control* (Elsevier, Inc., Burlington, 2010), 1st ed.

[75] F. Vasefi, N. MacKinnon, and D. Farkas, "Chapter 16 - hyperspectral and multispectral imaging in dermatology," in "Imaging in Dermatology," M. R. Hamblin, P. Avci, and G. K. Gupta, eds. (Academic Press, Boston, 2016), pp. 187 – 201.

[76] G. P. Garmire, M. W. Bautz, P. G. Ford, J. A. Nousek, and G. R. Ricker, "Advanced CCD imaging spectrometer (ACIS) instrument on the Chandra X-ray Observatory," Proc. SPIE **4851** (2003).

[77] "Specim IQ," `http://www.specim.fi/iq/`. Accessed: 2018-10-14.

[78] F. Sigernes, M. Syrjäsuo, R. Storvold, J. ao Fortuna, M. E. Grøtte, and T. A. Johansen, "Do it yourself hyperspectral imager for handheld to airborne operations," Opt. Express **26**, 6021–6035 (2018).

[79] H. Yuan, M. Meixell, J. Zhang, P. Bey, J. Kimchi, and L. C. Kilmer, "Low dark current small pixel large format InGaAs 2D photodetector array development at Teledyne Judson Technologies," Proc.SPIE **8353**, 8353 – 8353 – 8 (2012).

[80] A. Rogalski, J. Antoszewski, and L. Faraone, "Third-generation infrared photodetector arrays," Journal of Applied Physics **105**, 091101 (2009).

[81] T. Spirig, P. Seitz, O. Vietze, and F. Heitger, "The Lock-In CCD-Two-Dimensional Synchronous Detection of Light," IEEE J. Quantum Electron. **31**, 1705–1708 (1995).

[82] K. Shibuya, T. Minamikawa, Y. Mizutani, H. Yamamoto, K. Minoshima, T. Yasui, and T. Iwata, "Scan-less hyperspectral dual-comb single-pixel-imaging in both amplitude and phase," Opt. Express **25**, 21947–21957 (2017).

[83] Y. Jung, H. Chen, L. Tong, and J.-X. Cheng, "Imaging gold nanorods by plasmon-resonance-enhanced four wave mixing," The Journal of Physical Chemistry C **113**, 2657–2663 (2009).

[84] Z. J. Smith, T. R. Huser, and S. Wachsmann-Hogiu, "Modern trends in imaging vi: Raman scattering in pathology," Analytical Cellular Pathology **35**, 145–163 (2012).

[85] A. M. Barlow, A. D. Slepkov, A. Ridsdale, P. J. McGinn, and A. Stolow, "Label-free hyperspectral nonlinear optical microscopy of the biofuel microalgae haematococcus pluvialis," Biomed. Opt. Express **5**, 3391–3402 (2014).

[86] J. Kasprzak, B. Patton, V. Savona, and W. Langbein, "Coherent coupling between distant excitons revealed by two-dimensional nonlinear hyperspectral imaging," Nature Photonics **5**, 57–63 (2010).

[87] Mller, Squier, D. Lange, and Brakenhoff, "Cars microscopy with folded boxcars phasematching," Journal of Microscopy **197**, 150–158 (2001).

[88] G. Nardin, T. M. Autry, K. L. Silverman, and S. T. Cundiff, "Multidimensional coherent photocurrent spectroscopy of a semiconductor nanostructure," Opt. Express **21**, 28617–28627 (2013).

[89] A. Yariv and P. Yeh, *Optical Waves in Crystals: Propagation and Control of Laser Radiation* (Wiley-Interscience, New York, 1984).

[90] S. T. Cundiff, "Coherent spectroscopy of semiconductors," Opt. Express **16**, 4639–4664 (2008).

[91] J. Roy, J.-D. Deschênes, S. Potvin, and J. Genest, "Continuous real-time correction and averaging for frequency comb interferometry," Opt. Express **20**, 21932–21939 (2012).

[92] T. Ideguchi, A. Poisson, G. Guelachvili, N. Picqué, and T. W. Hänsch, "Adaptive real-time dual-comb spectroscopy," Nature Communications **5**, 3375 (2014).

[93] X. Shen, M. Yan, Q. Hao, K. Yang, and H. Zeng, "Adaptive dual-comb spectroscopy with 1200-h continuous operation stability," IEEE Photonics J. **10** (2018).

[94] J.-D. Deschênes, P. Giaccari, and J. Genest, "Optical referencing technique with CW lasers as intermediate oscillators for continuous full delay range frequency comb interferometry," Opt. Express **18**, 23358–23370 (2010).

[95] D. A. B. Miller, D. S. Chemla, T. C. Damen, A. C. Gossard, W. Wiegmann, T. H. Wood, and C. A. Burrus, "Band-edge electroabsorption in quantum well structures: The quantum-confined stark effect," Phys. Rev. Lett. **53**, 2173–2176 (1984).

[96] L. V. Keldysh, "Ionization in the field of a strong electromagnetic wave," Journal of Experimental and Theoretical Physics **20**, 1307–1314 (1965).

[97] D. A. B. Miller, D. S. Chemla, and S. Schmitt-Rink, "Relation between electroabsorption in bulk semiconductors and in quantum wells: The quantum-confined Franz-Keldysh effect," Phys. Rev. B **33**, 6976–6982 (1986).

[98] B. L. Wilmer, D. Webber, J. M. Ashley, K. C. Hall, and A. D. Bristow, "Role of strain on the coherent properties of gaas excitons and biexcitons," Phys. Rev. B **94**, 075207 (2016).

[99] R. Singh, M. Richter, G. Moody, M. E. Siemens, H. Li, and S. T. Cundiff, "Localization dynamics of excitons in disordered semiconductor quantum wells," Phys. Rev. B **95**, 235307 (2017).

[100] S. Mukamel, *Principles of Nonlinear Optical Spectroscopy* (Oxford University Press, Oxford, 1999).

[101] S. T. Cundiff and S. Mukamel, "Optical multidimensional coherent spectroscopy," Physics Today **66** (2013).

[102] A. P. Spencer, B. Spokoyny, and E. Harel, "Enhanced-resolution single-shot 2DFT spectroscopy by spatial spectral interferometry," The Journal of Physical Chemistry Letters **6**, 945–950 (2015).

[103] L. M. Kiefer, J. T. King, and K. J. Kubarych, "Dynamics of rhenium photocatalysts revealed through ultrafast multidimensional spectroscopy," Accounts of Chemical Research **48**, 1123–1130 (2015).

[104] S. Draeger, S. Roeding, and T. Brixner, "Rapid-scan coherent 2D fluorescence spectroscopy," Opt. Express **25**, 3259–3267 (2017).

[105] B. Lomsadze, B. C. Smith, and S. T. Cundiff, "Tri-comb spectroscopy," Nature Photonics **12**, 676–680 (2018).

[106] J. A. Myers, K. L. M. Lewis, P. F. Tekavec, and J. P. Ogilvie, "Two-color two-dimensional fourier transform electronic spectroscopy with a pulse-shaper," Opt. Express **16**, 17420–17428 (2008).

[107] A. D. Bristow, D. Karaiskaj, X. Dai, T. Zhang, C. Carlsson, K. R. Hagen, R. Jimenez, and S. T. Cundiff, "A versatile ultrastable platform for optical multidimensional fourier-transform spectroscopy," Review of Scientific Instruments **80**, 073108 (2009).

[108] D. B. Turner, K. W. Stone, K. Gundogdu, and K. A. Nelson, "Invited Article: The coherent optical laser beam recombination technique (COLBERT) spectrometer: Coherent multidimensional spectroscopy made easier," Review of Scientific Instruments **82**, 081301 (2011).

[109] P. F. Tekavec, G. A. Lott, and A. H. Marcus, "Fluorescence-detected two-dimensional electronic coherence spectroscopy by acousto-optic phase modulation," The Journal of Chemical Physics **127**, 214307 (2007).

[110] D. B. Turner, P. C. Arpin, S. D. McClure, D. J. Ulness, and G. D. Scholes, "Coherent multidimensional optical spectra measured using incoherent light," Nature Communications **4** (2013).

[111] M. Khalil, N. Demirdven, and A. Tokmakoff, "Coherent 2D IR spectroscopy: molecular structure and dynamics in solution," The Journal of Physical Chemistry A **107**, 5258–5279 (2003).

[112] E. Lucas, G. Lihachev, R. Bouchand, N. G. Pavlov, A. S. Raja, M. Karpov, M. L. Gorodetsky, and T. J. Kippenberg, "Spatial multiplexing of soliton microcombs," Nature Photonics **12**, 699–705 (2018).

[113] Z. Lv, H. Teng, R. Wang, L. Wang, J. Wang, and Z. Wei, "Tunable triple-wavelength mode-locked ytterbium fiber laser with birefringence filter," Applied Physics B. **121**, 1–6 (2018).

[114] X. Zhao, X. Qu, F. Zhang, Y. Zhao, and G. Tang, "Absolute distance measurement by multi-heterodyne interferometry using an electro-optic triple comb," Opt. Lett. **43**, 807–810 (2018).

[115] X. Zhao, C. Li, T. Li, G. Hu, R. Li, M. Bai, T. Yasui, and Z. Zheng, "Dead-band-free, high-resolution microwave frequency measurement using a free-running triple-comb fiber laser," IEEE Journal of Selected Topics in Quantum Electronics **24**, 1–8 (2018).

[116] D. R. Carlson, D. D. Hickstein, W. Zhang, A. J. Metcalf, F. Quinlan, S. A. Diddams, and S. B. Papp, "Ultrafast electro-optic light with subcycle control," Science **361**, 1358–1363 (2018).

[117] Z. L. Newman, V. Maurice, T. E. Drake, J. R. Stone, T. C. Briles, D. T. Spencer, C. Fredrick, Q. Li, D. Westly, B. R. Ilic, B. Shen, M.-G. Suh, K. Y. Yang, C. Johnson, D. M. S. Johnson, L. Hollberg, K. Vahala, K. Srinivasan, S. A. Diddams, J. Kitching, S. B. Papp, and M. T. Hummon, "Photonic integration of an optical atomic clock," ArXiv e-prints (2018).

[118] H. A. Lorentz, *The theory of electrons and its applications to the phenomena of light and radiant heat* (Leipzig: B.G. Teubner, New York, 1909), 1st ed.

[119] H. A. Lorentz, "Ueber den einfluss magnetischer krfte auf die emission des lichtes," Annalen der Physik **299**, 278 (1897).

[120] P. Zeeman, "Over den invloed eener magnetisatie op den aard van het door een stof uitgezonden licht," Versl. Kon. Ak. Wet. **5**, 181–184 (1896).

[121] P. Zeeman, "Over den invloed eener magnetisatie op den aard van het door een stof uitgezonden licht, II." Versl. Kon. Ak. Wet. **5**, 242–248 (1896).

[122] A. J. Kox, "The discovery of the electron: II. the zeeman effect," European Journal of Physics **18**, 139 (1997).

[123] J. J. Thomson, "Cathode rays," The Electrician **39**, 103–109 (1897).

[124] J. Z. Buchwald and A. Warwick, eds., *Histories of the electron: the birth of microphysics* (MIT Press, Cambridge, Mass, 2001).

[125] A. Zangwill, *Modern Electrodynamics* (Cambridge University Press, Cambridge, 2013).

[126] P. W. Milonni and J. H. Eberly, *Lasers* (Wiley-Interscience, New York, 1988).

[127] W. M. Fisher and S. C. Rand, "Light-induced dynamics in the lorentz oscillator model with magnetic forces," Phys. Rev. A **82**, 013802 (2010).

[128] K. E. Oughstun and R. A. Albanese, "Magnetic field contribution to the lorentz model," J. Opt. Soc. Am. A **23**, 1751–1756 (2006).

[129] R. Hertel, "Theory of the inverse faraday effect in metals," Journal of Magnetism and Magnetic Materials **303**, L1 – L4 (2006).

[130] M. Battiato, G. Barbalinardo, and P. M. Oppeneer, "Quantum theory of the inverse faraday effect," Phys. Rev. B **89**, 014413 (2014).

[131] Z. Q. Qiu and S. D. Bader, "Surface magneto-optic kerr effect," Review of Scientific Instruments **71**, 1243–1255 (2000).

[132] W. Voigt, "Ueber das elektrische analogon des zeemaneffectes," Annalen der Physik **309**, 197–208 (1901).

[133] A. J. Kox, "The discovery of the stark effect and its early theoretical explanations," Annalen der Physik **525**, A63–A66 (2013).

[134] A. F. Gibson, M. F. Kimmitt, and A. C. Walker, "Photon drag in germanium," Applied Physics Letters **17**, 75–77 (1970).

[135] A. M. Danishevskiĭ, A. A. Kastal'Skiĭ, S. M. Ryvkin, and I. D. Yaroshetskiĭ, "Dragging of Free Carriers by Photons in Direct Interband Transitions in Semiconductors," Soviet Journal of Experimental and Theoretical Physics **31**, 292 (1970).

[136] A. F. Gibson, M. F. Kimmitt, A. O. Koohian, D. E. Evans, and G. F. D. Levy, "A study of radiation pressure in a refractive medium by the photon drag effect," Proceedings of the Royal Society of London. Series A, Mathematical and Physical Sciences **370**, 303–311 (1980).

[137] M. Mansuripur, "Radiation pressure and the linear momentum of the electromagnetic field," Opt. Express **12**, 5375–5401 (2004).

[138] R. Loudon, S. M. Barnett, and C. Baxter, "Radiation pressure and momentum transfer in dielectrics: The photon drag effect," Phys. Rev. A **71**, 063802 (2005).

[139] M. Mansuripur, "Radiation pressure and the linear momentum of light in dispersive dielectric media," Opt. Express **13**, 2245–2250 (2005).

[140] J. Birch, C. Bradley, and M. Kimmitt, "Absorption and refraction in germanium at 293k in the range 1250 cm1," Infrared Physics **14**, 189 – 197 (1974).

[141] I. V. Sokolov, "The angular momentum of an electromagnetic wave, the sadovski effect, and the generation of magnetic fields in a plasma," Soviet Physics Uspekhi **34**, 925 (1991).

[142] P. S. Pershan, J. P. van der Ziel, and L. D. Malmstrom, "Theoretical discussion of the inverse faraday effect, raman scattering, and related phenomena," Phys. Rev. **143**, 574–583 (1966).

[143] J. P. van der Ziel, P. S. Pershan, and L. D. Malmstrom, "Optically-induced magnetization resulting from the inverse faraday effect," Phys. Rev. Lett. **15**, 190–193 (1965).

[144] A. V. Kimel, A. Kirilyuk, P. A. Usachev, R. V. Pisarev, A. M. Balbashov, and T. Rasing, "Ultrafast non-thermal control of magnetization by instantaneous photomagnetic pulses," Nature **435**, 655 EP – (2005).

[145] I. Žutić, J. Fabian, and S. Das Sarma, "Spintronics: Fundamentals and applications," Rev. Mod. Phys. **76**, 323–410 (2004).

[146] D. Paget, G. Lampel, B. Sapoval, and V. I. Safarov, "Low field electron-nuclear spin coupling in gallium arsenide under optical pumping conditions," Phys. Rev. B **15**, 5780–5796 (1977).

[147] D. S. Bethune, R. W. Smith, and Y. R. Shen, "Optical quadrupole sum-frequency generation in sodium vapor," Phys. Rev. Lett. **37**, 431–434 (1976).

[148] D. S. Bethune, "Quadrupole second-harmonic generation for a focused beam of arbitrary transverse structure and polarization," Opt. Lett. **6**, 287–289 (1981).

[149] R. W. Terhune, P. D. Maker, and C. M. Savage, "Optical harmonic generation in calcite," Phys. Rev. Lett. **8**, 404–406 (1962).

[150] J. J. Thomson, "Cathode rays," Philos. Mag. **44**, 293–316 (1897).

[151] J. Larmor, "On the theory of the magnetic influence on spectra; and on the radiation from moving ions," The London, Edinburgh, and Dublin Philosophical Magazine and Journal of Science **44**, 503–512 (1897).

[152] D. J. Griffiths, *Introduction to Quantum Mechanics* (Pearson Education, Inc., Upper Saddle River, NJ, 2005), 2nd ed.

[153] H. Becquerel, "Sur une interprtation appligarle au phnomne de faraday et au phnomne de zeeman," J. Phys. Theor. Appl. **6**, 681 – 688 (1897).

[154] G. F. Fitzgerald, "Note on the connection between the faraday rotation of plane of polarisation and the zeeman change of frequency of light vibrations in a magnetic field," Proceedings of the Royal Society of London **63**, 31–35 (1898).

[155] V. B. Berestetskii, E. M. Lifshitz, and L. P. Pitaevskii, *Relativistic Quantum Theory* (Pergamon Press, Oxford, 1971).

[156] P. Tamarat, T. Gaebel, J. Rabeau, M. Khan, A. Greentree, H. Wilson, L. C L Hollenberg, S. Prawer, P. Hemmer, F. Jelezko, and J. Wrachtrup, "Stark shift control of single optical centers in diamond," Physical review letters **97**, 083002 (2006).

[157] L. D. Landau and E. M. Lifshitz, *Quantum Mechanics: Non-relativistic Theory* (Pergamon Press, Oxford, 1965), 2nd ed.

[158] W. Klemperer, K. K. Lehmann, J. K. G. Watson, and S. C. Wofsy, "Can molecules have permanent electric dipole moments?" The Journal of Physical Chemistry **97**, 2413–2416 (1993).

[159] S. Yefet and A. Pe'er, "A review of cavity design for kerr lens mode-locked solid-state lasers," Applied Sciences **3**, 694–724 (2013).

[160] T. Ideguchi, T. Nakamura, Y. Kobayashi, and K. Goda, "Kerr-lens mode-locked bidirectional dual-comb ring laser for broadband dual-comb spectroscopy," Optica **3**, 748–753 (2016).

[161] L. A. Sterczewski, J. Westberg, and G. Wysocki, "Computational coherent averaging for free-running dual-comb spectroscopy," ArXiv e-prints (2018).

[162] L. Greengard and J. Lee, "Accelerating the nonuniform fast fourier transform," SIAM Review **46**, 443–454 (2004).

[163] N. Belabas and D. M. Jonas, "Three-dimensional view of signal propagation in femtosecond four-wave mixing with application to the boxcars geometry," J. Opt. Soc. Am. B **22**, 655–674 (2005).

[164] D. M. Jonas, "Two-dimensional femtosecond spectroscopy," Annual Review of Physical Chemistry **54**, 425–463 (2003).

[165] A. P. Spencer, H. Li, S. T. Cundiff, and D. M. Jonas, "Pulse propagation effects in optical 2D fourier-transform spectroscopy: Theory," The Journal of Physical Chemistry A **119**, 3936–3960 (2015).

[166] M. K. Yetzbacher, N. Belabas, K. A. Kitney, and D. M. Jonas, "Propagation, beam geometry, and detection distortions of peak shapes in two-dimensional fourier transform spectra," The Journal of Chemical Physics **126**, 044511 (2007).

[167] C. L. Smallwood, T. M. Autry, and S. T. Cundiff, "Analytical solutions to the finite-pulse bloch model for multidimensional coherent spectroscopy," J. Opt. Soc. Am. B **34**, 419–429 (2017).